DYNAMICS OF DIFFERENT FISSION MECHANISMS USING FRAGMENTATION APPROACH

A THESIS

Submitted for the partial fulfillment of requirement for the award of the degree of

DOCTOR OF PHILOSOPHY

By

AMANDEEP KAUR
(Regn. No: 901412011)

under the guidance of

Dr. MANOJ K. SHARMA
(Professor)

THAPAR INSTITUTE
OF ENGINEERING & TECHNOLOGY
(Deemed to be University)

SCHOOL OF PHYSICS AND MATERIALS SCIENCE
THAPAR INSTITUTE OF ENGINEERING AND TECHNOLOGY, PATIALA-147004, PUNJAB, INDIA

AUGUST, 2019

.

Dedicated to

My Family

for their love and support

&

All of my friends

without whom none of my success would be possible

CERTIFICATE

This is to certify that the thesis entitled "**DYNAMICS OF DIFFERENT FISSION MECHANISMS USING FRAGMENTATION APPROACH**" being submitted by **Ms. Amandeep Kaur** for the fulfillment of the requirements for the award of Degree of Doctor of Philosophy in the School of Physics and Materials Science, Thapar Institute of Engineering and Technology, Patiala, is a record of the candidate's own work carried out by her under my supervision. The matter presented in this thesis has not been submitted in part or full for the award of any degree in any university or institute.

Supervisor

7.1.2020

Dr. Manoj K. Sharma

Professor

School of Physics and Materials Science

Thapar Institute of Engineering and Technology (TIET)

Patiala- 147004

Punjab (India)

Acknowledgements

First and above all, I praise God Almighty, for giving me the strength, knowledge, ability and opportunity to undertake this research study, and to complete it satisfactory. Without his blessings, this achievement would not have been possible. This thesis appears in its current form due to the assistance and guidance of several people. I would therefore like to offer my sincere thanks to all of them.

I would like to express my sincere gratitude to my esteemed supervisor Dr. Manoj K. Sharma, Professor, School of Physics and Materials Science, Thapar Institute of Engineering and Technology (TIET), Patiala, for the continuous support of my PhD study and research. His guidance helped me in all the time of research and writing of this thesis. For me he is an example of the skillful academic who makes the balance in all aspects of his life. It was an honor to work with him. I thank him personally for being such a wonderful and supportive supervisor. Special thanks to Sonam madam for all her love and affection. I am very grateful to Late Prof. Raj K. Gupta, Department of Physics, Panjab University, Chandigarh, and Prof. S. K. Patra, Institute of Physics, Bhubaneswar, for their support and suggestions in my research work.

I express profound gratitude to Prof. O. P. Pandey, Head, School of Physics and Materials Science and Prof. Rafat Siddique, Dean of research and sponsored projects, TIET, Patiala, to provide me with all facilities to carry out this research work. I sincerely appreciate the whole hearted cooperation and valuable suggestions provided by Advisory Doctoral Committee comprising Dr. Sunil Devi, Dr. Raj Kumar and Dr. A. K. Lal. My sincere thanks also goes to all the staff of the School for their help and kind support.

I also express my heartfelt thanks to my lab mates Dr. Gurvinder Kaur, Dr. Gudveen Sawhney, Dr. Kirandeep Sandhu, Dr. Rajni, Dr. Manjeet Singh Gautam, Dr. Amandeep Kaur, Ms. Gurjit Kaur, Ms. Ishita Sharma, Mrs. Navjot Kaur Virk, Mr. Nitin Sharma and Mr. Vishal Parmar, for their co-operation and encouragement. The journey of PhD will not be easy without my lovely friends. I owe a deep sense of gratitude to my friends Neha, Kanishka and Shivani for all the fantastic moments we spent together. My special thanks go to my bestie Sangeeta, who always with me in every kind of situations. I can't even explain how grateful I am to have you in my life. Your support is precious, no one can replace you. I am also thankful to members of other lab groups specially Kaushlendra,

Santhosh, Saloni, Pallavi, Raveena, Amanpreet, Kaveri, Indu and Gaurav for their help and all the fun we had during Ph.D. I really enjoyed and cherished the moments spent with you all.

Acknowledgements seem to be incomplete without a word of thanks and appreciation to my family, whose cooperation, patience and prayers helped me to materialize my dream of a thesis into reality. I deeply thank my grandparents for their unconditional trust, timely encouragement, and endless patience. Mummy, Papa I do not know how to thank you enough for providing me with the opportunity to be where I am today. I always knew that you believed in me and wanted the best for me. Also, I thank to my brother and sister-in-law for their amazing love and care. I dedicate this work to you all.

The financial assistance from University Grant Commission (UGC), Government of India, New Delhi, under the "Maulana Azad National Fellowship for Minority Students Scheme" is gratefully acknowledged.

Amandeep Kaur

Patiala
August, 2019.

(Amandeep Kaur)

List of Publications :

A. Journals :

1. Fine structure effect among heavy-ion induced fission fragments at near and above barrier energies,
   Amandeep Kaur and Manoj K. Sharma,
   Eur. Phys. J. A **55**, 89 (2019).

2. Investigation of various decay mechanisms for ^{216}Th* following the ^{32}S+^{184}W reaction in the range $E_{c.m.}$=118-196 MeV,
   Amandeep Kaur and Manoj K. Sharma,
   Phys. Rev. C **99**, 044611 (2019).

3. Across barrier fission analysis of At* isotopes formed in ^{3,4,6,8}He+^{209}Bi reactions,
   Amandeep Kaur, Gurjit Kaur, S. K. Patra and Manoj K. Sharma,
   Nucl. Phys. A **990**, 94 (2019).

4. Fission cross sections and fragment mass distribution of actinide nuclei formed in n-induced reactions,
   Amandeep Kaur, Guvinder Kaur and Manoj K. Sharma,
   Braz. J. Phys **48**, 608 (2018).

5. Spontaneous fission of the end product in α-decay chain of recoiled superheavy nucleus: A theoretical study,
   Amandeep Kaur, Gudveen Sawhney, Manoj K. Sharma and Raj K. Gupta,
   Int. Jour. of Mod. Phys. E **27**, 1850043 (2018).

6. Decay analysis of Ge isotopes formed in reactions induced by tightly and loosely bound projectiles,
   Amandeep Kaur, Kirandeep Sandhu and Manoj K. Sharma,
   Commun. Theor. Phys. **70**, 565 (2018).

7. Analysis of spontaneous fission in superheavy mass region using the dynamical cluster-decay model,

Gudveen Sawhney, **Amandeep Kaur**, Manoj K. Sharma and Raj K. Gupta,
Acta Phys. Pol. B **48**, 629 (2017).

8. Fission fragmentation analysis of ^{211}At* nucleus formed in ^{19}F+^{192}Os reaction,
Amandeep Kaur and Manoj K. Sharma,
Indian J. Pure Appl. Phys. **57**, 576 (2019).

9. Decay analysis of ^{216}Th* nucleus using dynamical cluster-decay model,
Amandeep Kaur and Manoj K. Sharma,
AIP conference proceedings **2006**, 030001 (2018).

10. Dynamics of Db isotopes formed in reactions induced by ^{238}U, ^{248}Cm and ^{249}Bk across the Coulomb barrier, (Not part of this thesis)
Gurjit Kaur, Kirandeep Sandhu, **Amandeep Kaur** and Manoj K. Sharma,
Phys. Rev. C **97**, 054602 (2018).

11. Fission fragment mass distributions of Astatine isotopes within collective clusterization approach,
Amandeep Kaur and Manoj K. Sharma,
J. Phys. Conf. Ser. (2019) submitted.

B. International/ National Symposia/ Workshops/ Conferences:

12. Fission fragment mass distributions of Astatine isotopes within collective clusterization approach, (Poster presentation)
Amandeep Kaur and Manoj K. Sharma,
International nuclear physics conference (INPC-2019), Glasgow, United Kingdom, July 29 - August 2, 2019.

13. Mass distribution and spontaneous fission half-lives of Nobelium isotopes using preformed cluster method, (Poster Presentation)
Amandeep Kaur, Gudveen Sawhney, Jyoti and Manoj K. Sharma,
Proceedings of the DAE Symp. on Nucl. Phys. **63**, 714 (2018).

DAE International Symposium on Nuclear Physics, Bhabha Atomic Research Centre, Mumbai, December 10-14, 2018.

14. Decay analysis of Nobelium isotopes using preformed cluster model, (Oral Presentation)
    Amandeep Kaur, Jyoti and Manoj K. Sharma,
    Punjab Science Congress, Punjab Agriculture University, Ludhiana, INDIA, February 7-9, 2018.

15. Study on structural aspects of the spontaneous fission in superheavy region, (Poster Presentation)
    Amandeep Kaur, Gudveen Sawhney, Manoj K. Sharma and Raj K. Gupta,
    Proceedings of the DAE Symp. on Nucl. Phys. **62**, 518 (2017).
    62^{th} DAE-BRNS Symposium on Nuclear Physics, Thapar Institute of Engineering and Technology, Patiala, INDIA, December 20-24, 2017.

16. Dynamics of p-induced fission of actinide nuclei using collective clusterization approach, (Poster Presentation)
    Amandeep Kaur, Gurvinder Kaur and Manoj K. Sharma,
    Proceedings of the DAE Symp. on Nucl. Phys. **61**, 516 (2016).
    61^{th} DAE-BRNS Symposium on Nuclear Physics, Saha Institute of Nuclear Physics, Kolkata, INDIA, June 20-24, 2016.

17. Fusion dynamics of ^{20}Ne+^{208}Pb reaction using static and energy dependent Woods-Saxson potential, (Poster Presentation)
    Manjeet Singh Gautam, **Amandeep Kaur** and Manoj K. Sharma,
    Proceedings of the DAE Symp. on Nucl. Phys. **60** 410 (2015).
    60^{th} DAE-BRNS Symposium on Nuclear Physics, Sri Sathya Sai Institute of Higher Learning, Prasanthi Nilayam, Andra Pradesh, INDIA, December 7-11, 2015.

Contents

List of Figures

List of Tables

ABSTRACT

The fusion-fission mechanism is a complex process which consists a collective motion of nucleons at compound nucleus stage and its subsequent segregation in the fission channel. Significant progress on experimental and theoretical front has helped immensely to understand this intricate process. The main emphasis in this thesis is to investigate the dynamics of different fission mechanisms. The work is committed to the study of several compound nucleus (CN) and non-compound nucleus (nCN) fission mechanisms of light and heavy nuclei formed in nuclear reactions, which involve different type of projectiles, e.g., light particles, loosely bound nuclei and heavy ions. This investigation is performed by utilizing the collective clusterization technique of "dynamical cluster-decay model (DCM)", thereby the contribution of light particles in the decay process is also investigated along with the fission process. The collective fragmentation potential is calculated using macro-microscopic method, which in turn helps to estimate the mass fragmentation and related cross-section yields in the decay channel. Here, the structural information of fissioning nuclei is obtained by calculating the preformation probability (P_0) of the nascent fragments. Current study includes the temperature (T) and angular momentum (ℓ) effects, which have decisive impact on fission process. Besides this, the deformation and orientation effects of decaying fragments are also incorporated via the radius vector. The calculated results for different fission mechanisms compare nicely with the experimental data, and some predictions are made which can be verified via future experiments. Besides induced fission, spontaneous fission (SF) occurring at the end of α-decay chains of superhavey nuclei (SHN) is also explored in this thesis. Thesis covers seven chapters, a brief account of layout is discussed below.

Chapter 1 consists a brief overview of nuclear fission research in recent times, with possible scenario of further applications in this area. The phenomenal experimental findings accompanied by theoretical investigations over the last few decades are highlighted. The dynamics of different CN and nCN processes along with their dependence on various entrance channel properties are discussed. The identification of the contribution of various competing CN and nCN decay channels is an intricate process. Therefore, a brief description of experimental techniques and theoretical models, which are used to identify

such processes is provided. In addition to this, the SF of SHN, and its influence on the synthesis of SHN is discussed in brief.

Chapter 2 provides the relevant information of dynamical cluster-decay model (DCM) employed to analyze the dynamics of different fission processes. This methodology is developed using dynamical fragmentation theory, which considers mass (or charge) asymmetry coordinate as a dynamical coordinate in order to study the mass (or charge) transfer in a nuclear decay process. The combine effect of attractive and repulsive energies on a decay process is examined in terms of collective fragmentation potential. In order to determine the fragment mass distributions and energetically favoured nascent fragments, the preformation probability (P_0) is evaluated using mass-asymmetry η-dependent Schrödinger wave equation. The methods of calculating the barrier tunneling probability (P) and decay cross-sections (σ) are also presented. Further, the procedures to evaluate the nCN processes (quasi fission and fast fission) and spontaneous fission are discussed. Note that the fast fission mechanism is studied for the first time within the DCM approach. Finally, the details of fission fragment anisotropy (A) using standard saddle-point statistical model (SSPSM) are given in this chapter. A descriptive analysis of work done using this methodology is covered in chapters 3-7.

Literature survey suggests that the spontaneous fission (SF) process plays a crucial role in identifying the newly synthesized superheavy nuclei (SHN), and hence demands a thorough study. In **chapter 3**, an effort is made to study the SF of $^{266}_{103}$Lr, $^{267}_{104}$Rf, $^{266-268}_{105}$Db, $^{281}_{111}$Rg, and $^{282}_{112}$Cn SHN appearing as end products in α-decay chains of other SHN. The analysis is carried out within the DCM for angular momentum ℓ=0 case, where the T-effects are incorporated from measured recoil energy (E_R) of SHN, left after few neutrons evaporation at the CN stage. The behaviour of fragment mass distribution and competitive emergence of the dominant decay modes, i.e., the α-emission vs. spontaneous fission, is studied by identifying the most probable heavy fission fragments, along with the estimation of SF half-life times $T^{SF}_{1/2}$ and total kinetic energy (TKE) of the above noted SHN. The mass distributions of chosen nuclei are symmetric in nature. The most preferred decay fragment is found to lie in the region of doubly magic shell closures of Z=50 and N=82, with highest preformation probability (P_0). In addition, a comparative study of the 'hot compact' and 'cold elongated' configurations of β_{2i}-deformed and θ^{opt}_i-

oriented nuclei indicate significantly different behavior of the two mass fragmentation yields, favoring 'hot compact' configuration. Finally, the role of 'shell corrections' in SF decay is duly investigated.

Chapter 4 contains the analysis of light particle (n and p) and heavy ion (^{32}S) induced fission of actinide nuclei. Firstly, the fission dynamics of odd mass actinide nuclei, ^{233}Th* and ^{239}U* produced in n-induced reactions is studied at various neutron energies, i.e, E_n=32.8 MeV-59.9 MeV. The fragment mass distributions are examined by choosing both spherical and deformed (upto β_2-static) fragmentation. The study is extended to two more actinide nuclei (^{233}Pa* and ^{239}Np*) and the barrier characteristics are compared for chosen reactions and corresponding preformation factor is worked out to estimate the relative influence on fragment mass distribution. In addition to this, the relative role of sticking and non-sticking moment of inertia on the fission decay of ^{233}Th* is explored. Besides this, a comparative study of n-induced reaction with p-induced reactions is carried out for Th and U nuclei. The investigation is carry out further by studying the various CN and nCN decay processes of ^{216}Th* actinide produced in the heavy-ion induced reaction, ^{32}S+^{184}W. This analysis is performed at across barrier energy window (118.8 MeV$\leq E_{c.m.} \leq$ 195.9 MeV) by including the quadrupole deformations (β_2-static) and optimum orientations ($\theta_i^{opt.}$) of the decay fragments. The anomalous behaviour of calculated fission anisotropies (A) for ^{216}Th* nucleus advocate the existence of nCN contributions, such as quasi fission (QF) and fast fission (FF). With an aim to have comprehensive analysis of CN and nCN fission mechanisms (ff, QF, FF), the role of center-of-mass energy ($E_{c.m.}$) and angular momentum is explored in terms of various observables of DCM e.g. fragmentation and scattering potentials along with preformation and tunneling probability. The fragmentation potential shows that asymmetric fission is the main decay mode of ^{216}Th* nucleus, independent of $E_{c.m.}$ and ℓ-values. The capture excitation functions $\sigma_{Cap.}$ are obtained by adding the DCM-calculated CN (σ_{CN}=σ_{ER}+σ_{ff}) and nCN (σ_{nCN}=σ_{QF}+σ_{FF}) contributions. The calculated cross-sections show good agreement with the experimental measurements, and the contribution of evaporation residue component is predicted to be rather small. The compound nucleus formation probability P_{CN} is estimated as a function of $E_{c.m.}$, which in turn suggest that maximum contribution from CN channel is approximately 65%. Finally, the impact of β_2-dynamic deformations on

the various decay mechanisms of ^{216}Th* nucleus is examined at highest $E_{c.m.}$=195.9 MeV, where nCN processes start competing the CN decay process.

In **Chapter 5**, DCM is engaged for the investigation of tightly bound and loosely bound He-projectile induced reactions involving lighter (^{64}Zn) and heavier (^{209}Bi) mass target. First, the decay of ^{68,70}Ge* compound systems formed, respectively, via tightly (^{4}He) and loosely (^{6}He) bound projectiles using ^{64}Zn target is studied over a wide energy range ($E_{c.m.}$∼5 to 16 MeV). The fusion excitation functions, obtained by adding various evaporation channels show good agreement with the available data for ^{4}He+^{64}Zn reaction. However, the predicted fission contributions come out to be negligibly small. On the contrary, the decrement in the fusion excitation functions of ^{70}Ge* nuclear system is addressed by presuming that ^{65}Zn evaporation residue is formed via breakup+transfer processes. The contribution of breakup+transfer channels for ^{6}He+^{64}Zn reaction is duly addressed by implementing appropriate energy corrections due to the breakup of '^{6}He' projectile into $2n$ and ^{4}He. Apart from this, the barrier lowering, angular momentum and energy dependence effects are also explored in view of the dynamics of aforementioned reactions. Next, the fission decay is examined for various ^{212,213,215,217}At* isotopes formed in tightly (^{3,4}He) and loosely bound (^{6,8}He) projectile induced on heavy mass target (^{209}Bi). By optimizing appropriate "neck-length parameter (ΔR)", the fission excitation functions are obtained for ^{212,213,215}At* compound nuclei (CN) at above barrier energies, where the experimental data is available. The DCM calculations are extended at below barrier region for these nuclei, and to other reaction ^{8}He+^{209}Bi→^{217}At*, using the systematics of ^{212,213,215}At* isotopes. The magnitude of fission cross-sections increases with the addition of neutrons in the He-projectile (or say in the At* compound nucleus since the target nucleus of each reaction is same) at common energies. To obtain better description of fission dynamics involved with neutron-deficient and neutron-rich He-induced reactions, the fragmentation potential and prefromation probability P_0 of decaying fragments are analyzed along with corresponding barrier tunneling probability P. The fission fragment mass distributions are explored for all 'At*' isotopes, and most probable fission fragments are identified. It has been observed that asymmetric fission forms the predominant decay mode for all considered isotopes, although a minor hump with very small preformation probability appears around symmetric fragments for lighter ^{212,213}At* nuclei. Finally,

the N/Z dependence of fission cross-sections and most probable decaying fragments, is explored in view of fragmentation structure and related cross-section yields.

After analyzing the decay of lighter and heavier nuclei produced in different type of projectile induced reactions, the fine structure effects in the fission fragments of pre-actinide and actinide nuclei are investigated in **chapter 6**. The fission decay of ^{201}Bi*, ^{206}Po*, ^{211}At*, ^{212}Rn*, ^{216}Ra*, ^{227}Pa* and ^{228}U* nuclei produced in ^{19}F-induced reactions at near and above barrier energies is explored. The interplay between two modes of fission i.e. symmetric (Sym) and asymmetric (Asym) in the fission fragment mass distributions is investigated. For present set of calculations the symmetric to asymmetric fission peak ratio is less than unity ($\frac{P_{Sym}}{P_{Asym}}$<1), which inturn suggests the dominance of asymmetric fission for above mentioned compound nuclei. The role of shell corrections and deformations of fragments in the fission dynamics is duly addressed. The evaluated fission excitation functions are in agreement with the experimental one, except for few energies above the barrier. This disagreement is associated with the possible existence of nCN fission as higher energies are more prone to these kind of processes. The study of fission fragment mass distributions is further extended to the isotopic analysis of above mentioned pre-actinide and actinide nuclei at common $E_{c.m.}$≈80 MeV near the barrier. It is observed that the lighter isotopes exhibit symmetric fission distribution, whereas heavier ones prefer to decay via asymmetric path. A transition between symmetric and asymmetric fission occurs around fissioning nuclei with N/Z≈1.4, showing the triple humped mass distribution suggesting comparable contribution of symmetric and asymmetric fission. Finally, the most energetic asymmetric light (A_L) and heavy (A_H) fission fragments are identified for the isotopes of above mentioned nuclei. Interestingly, the heavier asymmetric fission fragments are located near proton number around Z=50 for pre-actinide region and Z=54 for actinide nuclei.

Finally, in **chapter 7**, the results acquired from above mentioned studies are summarized, and a prospective outlook for further studies on fission dynamics is briefed.

Chapter 1

Introduction

1.1 Nuclear fission: an overview

The story of splitting of a heavy mass nucleus into two smaller nascent fragments began in 1930s. This process is an outcome of persistent attempts to understand the artificial radioactivity by numerous academicians working in that area. In 1934, I. Curie and F. Joliot discovered the artificial radioactivity by striking alpha (α) particles on stable nuclei [1]. E. Fermi further worked in this area, and observed that neutron (n) irradiation on heavy element prompts the production of a nucleus with higher mass number, or, a nucleus with higher charge number as a consequence of beta decay. The pursuit of his findings led Otto Hahn and Fritz Strassmann to the discovery in 1939, that a Uranium nucleus divides into two smaller parts with different proton (Z) and neutron (N) numbers, when struck with a neutron [2]. The term 'fission' for this new type of nuclear reaction was used by O. R. Frisch and L. Meitner, who measured the fragments observed from the disintegration of Uranium nucleus [3]. It is worth mentioning here that L. Meitner also contributed to the nuclear fission discovery, as she worked in the company of Otto Hahn, who received a Noble Prize in chemistry for his findings (and usually known as the "godfather of nuclear fission"). After a short time of nuclear fission discovery, Bohr and Wheeler published an article which explained the theory of fission using liquid drop model (LDM) [4]. This theory is still assisting the researchers to understand various aspects of nuclear fission. The next enthusiasm among scientists was to search for the possibility of spontaneous fission (SF) of heavy nucleus as a natural decay process instead of being induced by a nuclear particle. W. F. Libby endeavored first effort to find the SF of Uranium nucleus, however missed to discover it due to smallness of effect [5]. Further,

in 1940, two Russian physicists G. Flerov and K. Petrzhak discovered the SF in Uranium nucleus by utilizing more sensitive experimental techniques [6]. However, the theoretical prediction of SF process was already given by the Bohr and Wheeler in their theory of nuclear fission [4].

Until now, the exploration of nuclear fission was spread throughout the world. The findings of Otto Hahn and Fritz Strassmann were instantly acknowledged by the E. Fermi. Furthermore, he demonstrated the possibility of chain reactions in the n-induced fission of Uranium nucleus, and also confirmed that this process releases enormous amount of energy. After this momentous event, Fermi was drawn into the Manhattan project, which was set up to build an atomic bomb during the world war-II. This project's essential objective was to harness the power of the atomic nucleus to produce an unbelievably groundbreaking weapon. This project was terminated in 1945, with the trial of the first atom bomb in Alamogordo, New Mexico.

Eighty years have been passed from the discovery of nuclear fission, but this process is still important not only because of its use to make nuclear weapon for military purposes, but also its enduring concernment to the society. A small amount of excitation energy is required to disintegrate the atomic nucleus into two pieces, which is approximately equal to a few per thousand of its total binding energy (B.E.). This disintegration process generates enormous energy of the order of 200 MeV. In this manner, this particular content of nuclear energy is around 10^8 times greater than the energy produced from fossil fuels. The common use of nuclear energy is the electricity production from nuclear reactors using nuclear fission process, and approximately 14% of the total world's electricity is generated from nuclear fuel. The nuclear energy is also used as a driving force in ships, submarines and specific kinds of surface vessels. One important application of nuclear fission process is the production of radioisotopes. The demand for the radioisotopes is persistently rising, as they are essential ingredients in the fields of industry, medical science and agriculture. More than twenty isotopes are widespread for medical purposes, from which ^{99m}Tc and ^{131}I are the commonly used isotopes. The diagnosis and treatment of some cancer and cardiovascular diseases are now possible with the help of radiation technology. Moreover, the nuclear fission is very useful process for the detection of neutrons.

In general sense, the comprehensive knowledge of nuclear fission and its pros and

cons, is crucial due to its widespread use in everyday life. Moreover, it offers an extensive assortment of logical research on nuclear characteristics and general physics. The advancement in the nuclear fission research, intensely depends upon the improvement of the experimental techniques, the availability of projectile beams and fissioning nuclei material etc. Consequently, the traditional and constrained use of neutron 'or' light particle as a projectile in fission reactions has provided a limited chance of investigation of this process. In last few years, diverse advances have been made in theoretical and experimental nuclear fission research, e.g., the use of heavy and radioactive ions in place of light particles, identification and assessment of non-compound nucleus processes and development of nuclear detectors and accelerators. In the next section, the various developments in fission research that took place in last few decades are highlighted.

1.2 Highlights in nuclear fission research

Numerous advances have taken place in the field of nuclear fission after the year of its discovery. A brief history and some events happened in the area of nuclear fission have been described in the previous section. Further details of the phenomenal experimental findings accompanied by theoretical investigations over the last eight decades of nuclear fission study, are highlighted in Fig. 1.1. Initially, the focus of investigators has only on the light particle induced fission of stable nuclei at low energies 'or' on the spontaneous fissioning nuclei, due to the challenges at the experimental front. However, the successful testing of controlled fission chain reaction using a nuclear reactor, led the experimental advancements to the next level. Subsequently, various kind of fission mechanisms were detected by employing different probes like light-charged particles, heavy ions, loosely bound nuclei etc. The observed fission mechanisms are β-delayed fission [7, 8], compound nucleus (CN) [9] and non-compound nucleus (nCN) fission [10–12], ternary fission [13], electromagnetically induced fission [14], surrogate type of fission [15], photo fission [16] etc. The surrogate and photo fission methods are useful to examine the fission barrier characteristics in particular for non-fissile nuclei [15, 16] etc. In 1962, a dramatic example of spontaneous fission was observed from the isomeric state of heavy nuclear system [17]. The fission measurements involve the mass and charge distributions, kinetic energy and angular distributions, fission barriers, pre-fission particles, fission cross-sections, deforma-

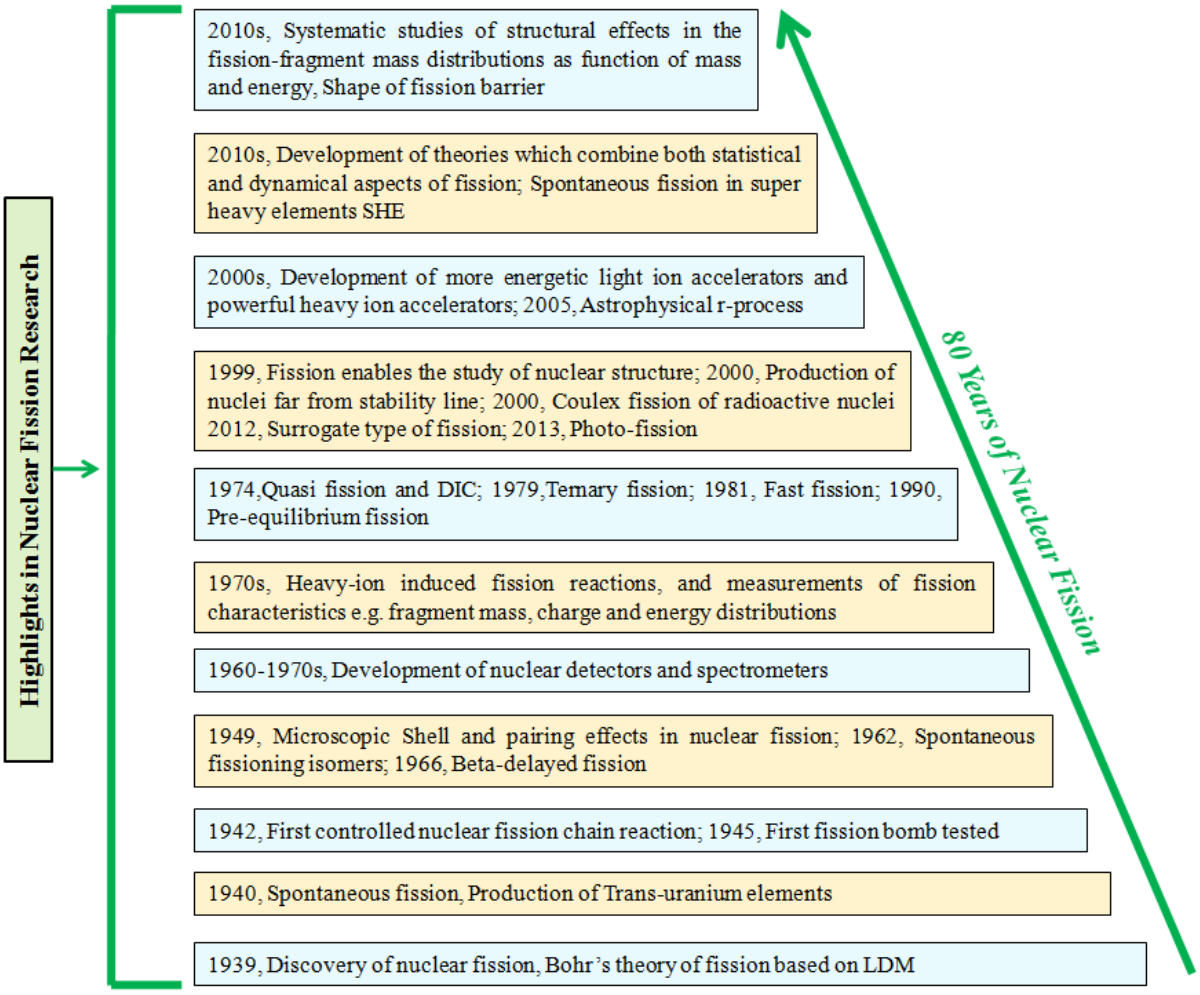

Figure 1.1: A pictorial view of various advances in the nuclear fission field, which have taken place over last eight decades after the discovery of fission process.

tions and level densities of fissioning nuclei. The comprehensive theoretical study of these measurements advocates the importance of microscopic shell and pairing effects. As a result of this, several theories have been developed to study the interplay between the macroscopic and microscopic effects, which further depend upon the excitation energies of fissioning nuclei. As a result macroscopic LDM and microscopic shell model were developed, which play important role to decide the mass division of compound nuclei [4,18–20]. The detailed description of other statistical/dynamical models developed using macro- and micro-scopic approaches, is given in section 1.6. Furthermore, the fission process play significant role in the analysis of nuclear structure, astrophysical r-processes [21] and production of nuclear systems away from stability line. Apart from this, the spontaneous fission play important role in the generation of superheavy nuclei (SHN) [22]. It is worth mentioning here that the fission mechanism strongly depends upon the entrance channel properties and excitation energies. This inturn results in the various non-compound nucleus (nCN) decay processes (e.g., quasifission (QF) [10], fast fission (FF) [11] and deep-inelastic collision (DIC) [23], see section 1.3. The development of the energetic and powerful light ion and heavy ion accelerators in last recent two decades, made it possible to analyze the fission decay of different pre-actinide and actinide nuclei. The surprising result of these studies, is the co-existence of symmetric (Sym) and asymmetric (Asym) fission channels in the mass distributions. An organized study of these sub-structural effects in the fragment mass distributions for a wide mass and energy window is highly desirable. Nowadays, this topic is very tempting and interesting to the researchers, which is the one of the objective of this thesis work, and the results are discussed in chapter 6. Moreover, the compound nucleus and non-compound nucleus fission mechanisms are investigated in present study, and are briefly addressed in the following sections.

1.3 Compound nucleus and non-compound nucleus decay mechanisms

In the initial years of nuclear fission research, light particle (e.g. n and p) induced fission was the main theme of studies, and these investigations unlocked the various aspects of fission phenomena. But, in 1960-70s, after the evolution of energetic heavy ion accelerators and nuclear detectors, the heavy ion induced fission becomes the fascinating subject. The

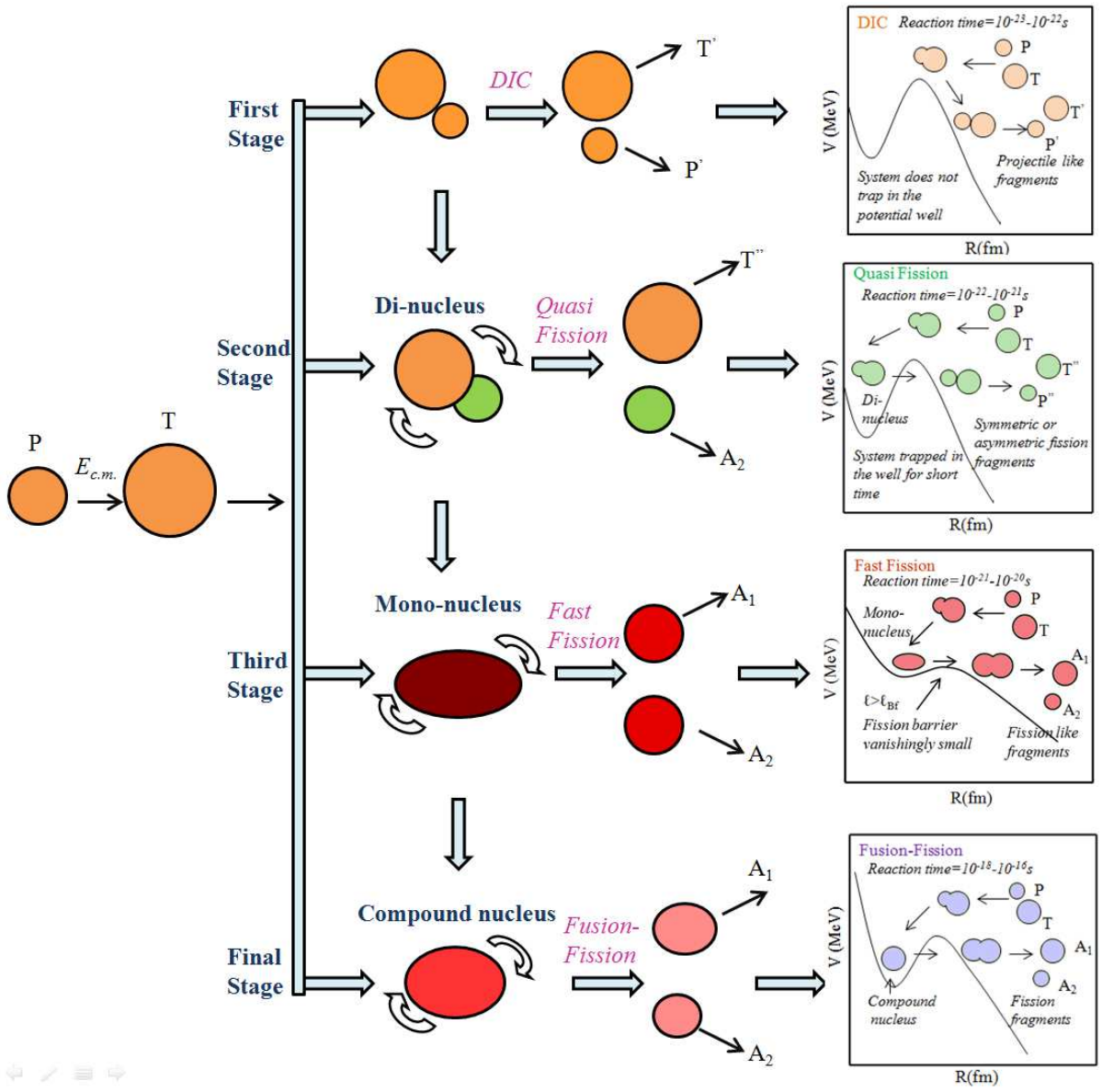

Figure 1.2: A diagram illustrating the journey of projectile-target composite system from non-equilibrated di-nucleus system (DNS) to equilibrated compound nucleus (CN).

collision of heavy ion with target nucleus over broad energies across the Coulomb barrier, provides a way to the nuclear matter to interact strongly, and consequently result in variety of decay modes. In the last three decades lots of work have been done in this area, but the full understanding of these phenomenon is still limited. Note that 'α' particle is considered as the 'lightest heavy ion'. The dynamics involved with heavy ion induced reactions is totally different from light particle induced reactions due to the following facts: (i) the huge Coulomb repulsion due to large atomic numbers of nuclear reactants, (ii) the large angular momentum related with the large mass of interacting partners, (iii) the formation probability is relatively large for heavy ion induced reaction.

A large number of processes can appear in the heavy ion collisions due to their above mentioned characteristics. Broadly speaking, in heavy ion induced reaction, complete amalgamation of projectile and target i.e. the formation of compound nucleus (CN) does not take place instantly. There could be possibility that such equilibrated stage is never achieved. In the course of systematic theoretical and experimental investigation of the static and dynamic conditions for heavy ion induced reaction, a competing process termed as non-compound nucleus (nCN) mechanism was observed. A considerable amount of energy dissipation is observed in these kind of reactions.

Fig. 1.2 represents the step-by-step view of different decay processes which are introduced via equilibrated and non-equilibrated projectile-target (P-T) composite system formed in heavy projectile induced reaction. In order to achieve the final phase of heavy ion induced reaction, i.e., an equilibrated CN, a P-T composite system could pass through the various reaction stages. At the point, when an energetic projectile nucleus strikes with the target nucleus, a capture process initiates. As a result, a di-nucleus (DNS) composition is formed, which is non-equilibrated in nature [24]. If this composition is neither trapped in the potential well, nor the full momentum transfer takes place, then the first stage of heavy ion reaction dynamics is known as deep inelastic collision (DIC). The decaying fragments in this process are similar to the projectile and target systems [25]. On the other side, if this nuclear system stuck in the potential well for a short time, then certain part of kinetic energy is dissipated and multi-nucleons are transferred. Since the incident energy is adequately large to cross the barrier, the DNS splits into two parts before it becomes equilibrated CN. This nCN process is known as quasi fission (QF),

which happens in the second stage of the collision as shown in Fig. 1.2. The fragments produced in this process may be symmetric or asymmetric depending upon the entrance channel mass asymmetry. This is an intermediate non-equilibrated nCN process, where the incoming channel is supposed to retain its identity [26, 27]. The typical reaction time for QF process is 10^{-22}-10^{-21}s which is much smaller than the reaction time of CN fission process (complete fusion-fission (ff)) i.e. 10^{-18}-10^{-16}s. This demonstrates that the QF and ff processes have different characteristics. Broadly speaking, the ff is a statistical process and depicted by temperature (T) and angular momentum (ℓ) effects, whereas QF is dynamical process which depends upon various entrance channel factors. Moreover, QF act as a decisive factor in the generation of superheavy nucleus (SHN), because it decreases the probability of complete fusion [28–31]. The contribution of QF process becomes dominant in massive reactions and at higher energies, this aspect is duly investigated in this thesis.

If the DNS survives the QF, it might be changed into mononucleus, see third stage of Fig. 1.2. The angular momentum (ℓ) of this rotating mononucleus is much higher, such that the fission barrier (Bf) start disappearing due to large rotational energy. The fission barrier of the nucleus, disappears at large magnitude of ℓ, where shell effects are significantly damped as a function of E^*_{CN} and ℓ. If $\ell \geq \ell_{Bf}$, where ℓ_{Bf} is angular momentum at which fission barrier disappears, then the mononucleus experiences quick splitting before reaching equilibrate state. This phenomenon is known as fast fission (FF) and produce two fragments which has similar properties like fusion-fission fragments [32]. This process is also prominent for massive reactions and higher energies. It is worth noting that FF process occurs only above the ℓ-values, where fission barrier disappears. However, QF can occurs at all ℓ-values of di-nucleus system [32].

If the P-T composite system relaxes in energy, mass, angular momentum and shape degree of freedom, eventually equilibrated CN is formed [33]. In Fig. 1.2, this is the last stage of heavy ion reaction having large reaction time, and involves complete amalgamation of reaction partners and consequently form the compound nucleus. The mass (A_{CN}) and excitation energy (E^*_{CN}) of compound nucleus decide that into which channel it will decay, e.g., evaporation residue (ER) or the fusion-fission (ff). Note that, the nascent fragments/clusters of a CN does not remember their history of formation following the

Bohr's hypothesis of independence [33].

The identification of these different kind of decay processes relies on the experimental facilities and theoretical evaluations. From above discussion, it may be concluded that the complete understanding of fission dynamics is essential. For instance, the understanding of CN fission (ff) and nCN fission (QF,FF) processes is important to identify best target projectile pairs for synthesis of new heavy/superheavy nuclei. The occurrence of different CN and nCN processes depends on various entrance channel factors which are discussed in the next section.

1.4 Entrance channel properties and nuclear fission

The nuclear reactions are observed to be extremely sensitive towards the characteristics of reaction partners. Several experimental as well as theoretical attempts have been made in this context. The studies showed that the occurrence of CN or nCN mechanisms relies on various factors, such as size and shape of projectile, mass asymmetry of reaction partners, incident energy, Coulomb repulsion factor, deformations, orientations etc. A brief explanation of these aspects is discussed below:

1.4.1 Type of projectile

As discussed in previous section, the reaction dynamics is strongly influenced by replacing the lighter projectile with the heavier one. The repulsive Coulomb and rotational energies involved in the heavy projectile induced reactions, are much larger than the light particle induced reactions. As a consequence, the possibility of complete fusion decreases, and result in the formation of non-equilibrated projectile-target composite system, which further decay via nCN processes.

In spite of this, the nuclear structure 'or' the nature of projectile has also impact on the reaction dynamics. The advancements that have been taken place in the experimental methods, allow one to use the radioactive ion beams in a nuclear reaction. For instance, if a loosely bound 'or' halo projectile hits the target nucleus in place of tightly bound projectile, the reaction dynamics get influenced in two ways: (i) the potential barrier gets lower due to the larger radius of loosely bound system, and results in the large reaction cross-sections, (ii) the lower binding energy of projectile gives rise to breakup

and transfer processes. Numerous nuclear reactions with different tightly and loosely bound projectiles on same targets has been tested to see the effect of projectile nature on the reaction dynamics [34–36]. In chapter 4 of this thesis, the detailed analysis of light particle and heavy ion induced fission of actinide nuclei is carried out. Besides this, chapter 5 is devoted to the tightly and loosely bound He-projectile induced reactions on light as well as heavy mass targets.

1.4.2 Mass asymmetry parameter

Mass asymmetry parameter (α_e) of entrance channel is an important probe to measure the probable occurrence of a reaction mechanism. According to the Bohr's hypothesis [33], the reaction cross-sections should be similar for same CN formed via different entrance channels at common excitation energy. Though literature showed that the evaporation residue and fusion-fission excitation functions are different for different reactions, regardless whether the compound nucleus is same. This difference is attributed to the fact that, the emergence of CN and nCN processes depends on the properties of reaction partners [37]. Apart from this, the impact of charge and neutron asymmetries of entrance channel on the potential well and barrier height is significant, which in turn effects the excitation functions [38, 39].

Basically, the mass asymmetry (α_e) parameter of entrance channel is the one of the important parameter which decides the type of decay process of projectile-target composite system. The mass asymmetry [α_e=A_T-A_P/(A_T+A_P)] of interacting nuclei play significant role to decide the contributions from CN and nCN fission processes. It is evident from literature [40], that if $\alpha_e<\alpha_{BG}$ then there is a possibility of nCN contributions. In fact, 'Businaro Gallone mass asymmetry (α_{BG})' is a parameter which separates mass symmetric liquid drop fission barrier from the asymmetric one [41, 42]. A large quantity of mass is transferred among reactants for the $\alpha_e>\alpha_{BG}$ condition, which results in an equilibrated composite system (i.e. CN). On the contrary, for $\alpha_e<\alpha_{BG}$, few nucleons transfer take place and a di-nuclear system is formed, which decays before achieving the equilibrium, thus giving rise to nCN process [40].

1.4.3 Incident energy

Plenty of work have been devoted to the incident energy dependence of all possible decaying properties of fissioning nuclei produced in variety of nuclear reactions. The compound nucleus formation/fusion probability (P_{CN}) is larger at incident energies below and near the Coulomb barrier as compared to above barrier energies. That means the contribution of evaporation residue and fusion-fission channels is prominent at below and near barrier energies than nCN processes [43]. However, nCN mechanism start competing the CN processes at above barrier energies. Relevant results are discussed for ^{32}S+^{184}W reaction in chapter 4. Moreover, the breakup and transfer processes also appear at above barrier energies, if the loosely bound projectile beam is involved in the nuclear reaction [34–36]. An effort is made in the thesis to analyze the reaction dynamics at broad energy range across the Coulomb barrier for various kind of reactions, and the results are discussed in chapters 4 to 6.

1.4.4 Coulomb repulsion factor

In addition to above mentioned factors, the Coulomb product ($Z_P Z_T$) of atomic numbers of projectile and target, strongly affect the reaction dynamics, and decides that which decay mode will be dominant. If the Coulomb repulsion between two heavy interacting nuclei is large, there is a dramatic reduction in probability of formation of compound nucleus. Therefore, projectile-target composite system separates earlier without reaching equilibrated state. Consequently, the quasi fission process may take place for a reaction having Coulomb product $Z_P Z_T \geq 1000$ [44]. This factor also serves as an obstacle in the generation of superheavy nuclei (SHN).

1.4.5 Deformations and orientations

Different studies suggest that the deformation and orientation effects play an important job in the formation of equilibrated and non-equilibrated composite system. The tip-to-tip collision of deformed reaction partners give rise to nCN processes. However, the side collisions generally lead to the complete fusion-fission processes [45]. The incorporation of deformations and orientations influence the values of barrier heights and interaction radii. As a consequence, the tunneling probabilities get influenced and hence the total

cross-sections. Therefore, the appropriate inclusion of deformation and orientation effects is extremely desirable for appropriate addressal of fission dynamics.

In addition to above, there are some other factors which affect the fission reaction dynamics as listed here: (i) Mass of CN (A_{CN}). (ii) Excitation energy of CN (E^*_{CN}). (iii) Total angular momentum of CN (ℓ_{max}). (iv) Fissility parameter of CN (Z^2/A). (v) N/Z ratio of CN, where N and Z, are, respectively the neutron number and atomic number of compound nucleus. Note that these quantities are interrelated to each other, and any change among them may affect the fission fragment mass distributions, and hence the overall fusion-fission dynamics. The related results are described in chapters 4 and 5.

1.5 Experimental methods to distinguish between CN and nCN fission

The distinguishing of various competing CN and nCN decay channels is a complicated process. The experimental signatures of these decay mechanisms may overlap with each other. In this way, it is hard to make their individual identification or the measurement of their contribution independently. Several experimental methods are accessible to find the existence of nCN fission in a nuclear reaction. A brief description of such methods is given below.

(i) The straightforward method to watch the presence of nCN content in a reaction is to measure the fission fragment angular anisotropies (A) and compare them with the theoretical calculations [46]. The fission fragment anisotropy are extracted from measured angular distributions of fission fragments [47]. Generally, fission anisotropy is calculated using standard saddle-point statistical model (SSPSM) [48], details are present in chapter 2. This method assumes that the nascent fragments are decaying towards symmetry axis of parent nucleus. The projection of the angular momentum on this axis is conserved from saddle to scission point. This supposition may not be justified for massive nuclei due to the different nuclear configurations at these two points. As a consequence, the SSPSM based anisotropies deviate from the experimental ones, which inturn advocate the presence of nCN fission. Similar results are observed in the study of chapter 4, where SSPSM does not properly described the fission anisotropies at higher energies, indicating the presence of nCN in the decay of ^{216}Th* nucleus [49].

(ii) The physical demonstration of nCN content in a nuclear reaction can be attained on account of the different reaction times of CN and nCN processes. The separation of two fragments during nCN process takes place in a very short timescale in comparison with the CN process [50, 51], therefore, the direct evidence of different CN and nCN processes can be observed in terms of reaction times. The experimentalists use blocking technique to extract the nuclear reaction times, the details of such kind of experiment are given in Ref. [52].

(iii) The fission fragments originating from nCN process are often characterized by their broad mass distribution, mass angle correlations, kinetic energy and angular distributions etc. [46, 53], which indicate a non-equilibrium origin and small sticking time of the decaying system compared to those originating from CN fission. If there is a possibility of nCN decay, a different pattern arises in the mass or kinetic energy distributions. Therefore, the plot of width of distributions vs excitation energy is an authentic tool to distinguish between CN and nCN fission.

(iv) Recently, γ rays were used as a probe to differentiate between CN and nCN fission on the basis of their angular momenta [54]. It is known that CN fission is a slow process as compared to the nCN fission. Therefore, distinct regions of angular momentum are generated via equilibrated and non-equilibrated fission processes. A possible way to achieve the separation between the CN and nCN fission is the measurement of angular momentum of decaying fragments by detecting γ rays [54].

(v) According to Bohr's hypothesis [33], the nuclear reactions with same CN but different entrance channels should give the same fusion cross-sections at same excitation energies, as discussed in previous section. But, for reactions prone to nCN channel, the probability of pure fusion gets diminished. As a result, the fusion excitation functions are suppressed, and this suppression is treated as an evidence of nCN fission. In spite of all above mentioned tools, the identification of nCN fission is still a difficult task. Thus, one needs proper interpretation of such experimental methods via appropriate theoretical approaches. Thereby, in the next section different theoretical approaches are discussed which are used to explain the fission mechanisms.

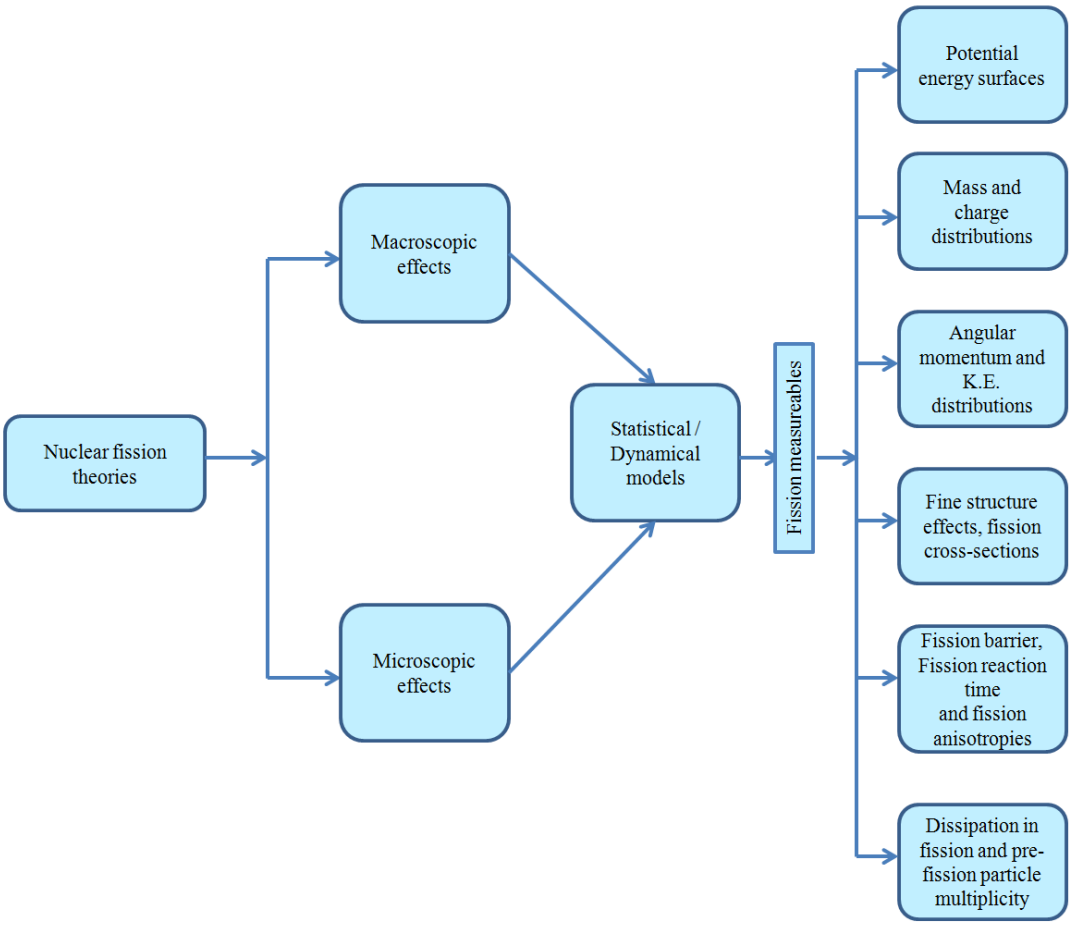

Figure 1.3: A schematic view of statistical/dynamical theories development on the basis of macroscopic and microscopic effects, which further used to describe different measurables of fission process.

1.6 Different theoretical approaches used to study fission mechanisms

Extensive theories were formulated to understand the dynamics associated with fission mechanisms, and to depict numerous fission measurables. The main driving factors relating to fission studies are: structure, dynamics and energy dissipation, which affect the various aspects of fission dynamics. Until now, large amount of data is available from the experiments on fission mechanism. The theoretical verification of available experimental fission data is carried out via various theoretical descriptions and many useful insights are predicted for future experiments on this area. The very first theory of nuclear fission was given by Bohr and Wheeler, who explained the fission process using macroscopic approach of liquid drop model (LDM) [4]. They proposed the idea of compound nucleus

(CN), which can deform itself up to the critical point due to the competition between Coulomb repulsion and nuclear proximity forces (nuclear surface tension). Beyond this point, the nuclear system becomes unstable and decay via fission process. The running theme in the nuclear fission research is the co-existence of macroscopic liquid drop and microscopic shell effects in fissioning nuclei, as illustrated in Fig. 1.3. The rich interplay between the nuclear structure and the reaction dynamics has been brought out in the analysis of fission reactions. In this domain, the enormous development has been made in last few decades for the overall understanding of various nuclear fission aspects. Several statistical/dynamical theories were developed which provide the combine effect of macroscopic and microscopic approaches, which are useful to calculate the potential energy surfaces (PES) of heavy fissioning nuclei [55]. Other than this, the self-consistent microscopic model based on density-dependent Hartree-Fock-Bogolyubov approach were also developed to analyze the low energy fission [56]. The pair breaking in fission or the fine structure effects in fission fragments were also analyzed using the Combinatorial model [57]. The time dependent Hartree-Fock method was used to investigate the induced fission of heavy nuclei and results were compared with macro-microscopic approaches [58]. This method deals with the all degrees of freedom related to dynamics of every constituent particle, thereby able to describe the complicated quasi fission process. Further, the fission process was also described well by statistical saddle and scission point models [59–63]. The standard saddle point statistical model (SSPSM) was successfully applied to study the reactions with lighter mass projectiles [48]. However, this approach is incapable to explain the fission fragment anisotropies for heavy ion induced reactions, and hence used as a probe to find the existence of nCN content. Apart from this, dinucleus system model [39, 43] and pre-equilibrium fission model [12, 47] were developed to study CN and nCN fission contributions individually. In the thesis work, the equilibrated and non-equilibrated fission processes are investigated by employing dynamical cluster-decay model (DCM) approach [49]. The DCM is derived from dynamical fragmentation theory [64–66], in which Strutinsky macro-microscopic method is used to describe the collective fragmentation process. This model has been successfully applied on numerous nuclear reactions and various CN and nCN mechanisms. The detailed description of DCM is presented in chapter 2.

1.7 Spontaneous fission of superheavy nuclei

Using the macroscopic theory of liquid drop model, Bohr and Wheeler set a limit for spontaneous fission (SF) process, i.e., $Z^2/A = 48$ [4]. Here, Z and A are respectively the charge and mass number of parent nucleus. If a nucleus crosses this limit of stability, it becomes unstable and decay via SF. The first experimental proof of this phenomenon was given by Flerov and Petrzhak in 1940 [6]. Since then, a large number of heavy nuclei are found to decay via SF process. The SF half-lives of these nuclei may vary from number of years to the small fraction of a second. If the charge number (Z) of a nucleus rises, the height of fission barrier is expected to show decrement. Hence, the probability of SF decay is small for lighter actinide nuclei, but increases dramatically with increase in charge number of nuclear systems. The SF process share the same fundamental mechanisms as that of alpha (α) decay, such as the fragment preformation and quantum tunneling process. The SF is equally complex process due to the large uncertainties among the mass and charge number of nascent fragments and associated released energy.

α-decay and SF process are the important topics as they play crucial role in the production of superheavy nuclei (SHN). The existence of long lived SHN is restrained by these two processes [22]. In literature, different α-decay chains are measured, and for most of the cases their end product is a spontaneous fissioning superheavy nuclei. That means both α- and SF-decay are the main obstacles (besides QF) in the production of long-lived SHN. Numerous theoretical attempts have been made to understand these two phenomenon thoroughly. DCM for ℓ=0 case was utilized to study the several alpha decay chains of recoiled SHN [67]. The temperature effects were incorporated in terms of recoil energy (E_R) of the SHN. The estimated alpha decay half-life times show nice agreement with experimental data. An attempt is made in chapter 3 to understand the SF process of SHN which is occurring as an end product in the α-decay chain. The fission fragment mass distributions are also analyzed for spontaneous fissioning nuclei, in order to acquire the knowledge of most probable decaying fission fragments.

1.8 Motivation of the present work

In previous sections, an attempt is made to give the overview of research work done in the area of fusion-fission dynamics. However, the complete survey of fission studies is likely impossible due to the pace of improvement and broadness of research work. The previous mentioned discussions on fission dynamics and related aspects provide a motivation to understand this phenomenon in more details. Thus the problems studied in this work revolve around the different kind of fission mechanisms induced via various type of projectiles say light, heavy and loosely bound nuclei etc. It may be noted that, the experimental findings are not much worthy without the theoretical verifications and vice versa. Hence, in the present thesis work, the dynamical cluster-decay model (DCM) based on quantum mechanical fragmentation theory (QMFT) is employed to study various fission mechanisms of different nuclei. A list of approved objectives is enumerated below:

1. Study of spontaneous fission of superheavy nuclei occurring as end product in the α-decay chains.

2. Fission decay investigation of light and heavy nuclei produced via different kind of projectiles such as light particles, heavy ions and loosely bound nuclei at wide energy range across the Coulomb barrier.

3. The comparative analysis of CN and nCN fission processes in terms of energy, temperature and angular momentum effects.

4. The study of fine structure effects in the fission fragment mass distributions, and identification of nascent fission fragments.

5. Comparison of DCM-calculated results with the experimental measurements.

The detailed description of these objectives and organization of the thesis is discussed in the following section.

1.9 Organization of thesis

After discussing the general introduction of nuclear fission research and problem formulation in present chapter, the thesis is further divided into six more chapters. A diagram-

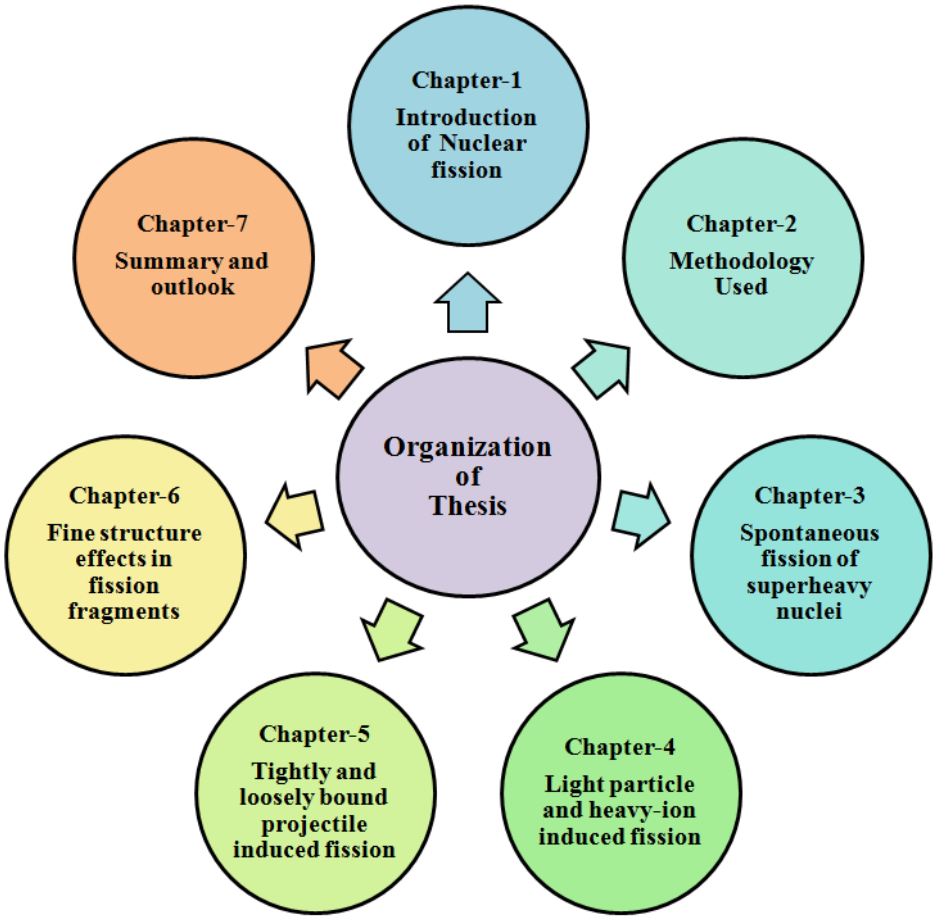

Figure 1.4: A schematic presentation of chapter wise organized thesis.

matic look of these chapters is given in Fig. 1.4, and an outline of the thesis is given below:

- **Chapter 2** is devoted to the description of the methodology used in present work to analyze the different CN and nCN fission mechanisms. The collective clusterization approach of QMFT based DCM is described in details. The essential ingredient of DCM is the fragmentation potential, which goes as input to the Schödinger equation, and further solved to estimate the preformation probability P_0 of decaying fragments. P_0 is the probability of finding certain mass fragments at position R on the decay path, and used to depict the fine-structure features about the fissioning nuclei. Apart from this, the precise discussion of Wentzel-Kramers-Brillouin (WKB) approximation based penetration probability P is given in details. Using P_0 and P, the fission excitation functions are calculated for various decay products studied in

this work. The calculated results are discussed in the succeeding chapters.

- In **Chapter 3**, the spontaneous fission (SF) of superheavy nuclei (SHN) is analyzed within DCM for angular momentum ℓ=0 case. The considered spontaneous fissioning nuclei are $^{266}_{103}$Lr, $^{267}_{104}$Rf, $^{266-268}_{105}$Db, $^{281}_{111}$Rg, and $^{282}_{112}$Cn, occuring as an end product in the α-decay chains of SHN. It is well known that both α-decay and SF are the decisive factors in the production of new SHN. Hence the possible competition between SF and α-decay of SHN is explored in terms of half-life times ($T_{1/2}$), preformation factor (P_0) and penetrability (P), and identifying the SF as a prominent decay mode for above mentioned SHN. The obtained SF half-life times show good agreement with experimental values. Further, the fragment mass distribution of spontaneous fissioning nuclei are studied along with the identification of energetically most favoured fission fragments. Finally, the orientation effects in SF are investigated in terms of 'hot compact' and 'cold elongated' configurations of decay fragments. After studying the SF of SHN, which is a tempting topic in nuclear fission research as it strongly influence the production of SHN, the thesis work is further extended to the study of light particle and heavy ion induced fission of actinide nuclei.

- The first part of **Chapter 4** presents the fission cross-sections of actinide nuclei produced in n+^{232}Th and n+^{238}U nuclear reactions, at incident energy window 32.8$\leq$ $E_n$$\leq$59.9 MeV. The fission fragment mass distributions are examined for the choice of spherical and β_2-deformed fragmentation. The investigation is broadened further for two more n+^{232}Pa and n+^{238}Np reactions, to analyze the barrier characteristics and mass distributions. The use of sticking and non-sticking moment of inertia in rotational energy is tested for ^{233}Th* nucleus. Finally, the fission dynamics of Th and U nuclei is investigated by replacing neutral n-projectile with the charged p-projectile at common incident energy. In the second part of this chapter, the fission dynamics of ^{216}Th* nucleus formed in heavy ion induced reaction, i.e., ^{32}S+^{184}W is studied. The analysis is carried out at centre-of-energies ($E_{c.m.}$) across the Coulomb barrier varying from 118 to 195.9 MeV. The fission fragment anisotropies (A) are calculated within SSPSM by utilizing DCM parameters. The calculated anionotropies show a deviation from the experimental data at above barrier energies, thus indicates

the presence of non-compound nucleus (nCN) fission. Further, the cross-sections of CN fission ['or' say fusion-fission (ff)] and nCN fission [i.e. quasi fission (QF) and fast fission (FF)] are estimated within DCM approach, and their sum is in accordance with experimental capture cross-sections which involves the content of CN and nCN fission. Moreover, the evaporation residue (ER) excitation functions are predicted which comes out be negligibly small. The angular momentum, energy and dynamic deformation effects are explored in terms of fragmentation potential, preformation probability, penetrability and fission cross-sections of CN and nCN fission processes. Lastly, the probability of compound nucleus formation (P_{CN}) is calculated as a function of $E_{c.m.}$.

- **Chapter 5** represents the study of tightly and loosely bound He-induced reactions on light and heavy mass target systems. When tightly bound '^{4}He' and loosely bound '^{6}He' projectiles strike to the light mass '^{64}Zn' target, the ^{68,70}Ge* compound nuclei are formed, which mainly decay via evaporation residue (ER) channels. For these light mass compound nuclei, the predicted fission excitation functions are very small. However, the fusion excitation functions are calculated by the summation of various ER cross-sections at $E_{c.m.}\sim$5 to 16 MeV across the barrier. Because of the loosely bound nature of ^{6}He-projectile, sub-barrier enhancement and above-barrier suppression are observed in the complete fusion excitation functions of ^{6}He+^{64}Zn in reference to the ^{4}He-induced reactions. This analysis is extended for ^{212,213,215}At* compound nuclei formed in other ^{3,4,6}He-induced reactions involving heavier target ^{209}Bi. By optimizing appropriate "neck-length parameter ΔR", the fission excitation functions are calculated for ^{212,213,215}At* systems at above barrier energies, where some experimental data is available. The DCM calculations are extended at below barrier region for these nuclei, and to other reaction ^{8}He+^{209}Bi$\rightarrow{}^{217}$At*, using the systematics of ^{212,213,215}At* isotopes. To obtain better description of fission dynamics involved with neutron-deficient and neutron-rich He-induced reactions, the fragmentation potential and preformation probability P_0 of fission products are analyzed along with corresponding barrier tunneling probability P. The fission fragment mass distributions are explored for all 'At' isotopes, and most probable fission fragments are identified. Lastly, the N/Z dependence of various DCM based fission

observables is examined.

- **Chapter 6** focused on the study of fine structure effects in the fission fragments of $^{201}Bi^{*}$, $^{206}Po^{*}$, $^{211}At^{*}$, $^{212}Rn^{*}$, $^{216}Ra^{*}$, $^{227}Pa^{*}$ and $^{228}U^{*}$ nuclei produced in ^{19}F-induced reactions. The co-existence of symmetric and asymmetric mass distribution among fission fragments is investigated by calculating their peak ratios as a function of energy, which inturn suggest the dominance of asymmetric fission for aforementioned nuclei. The fission excitation functions are calculated at wide energy range. The deviation of fission contributions at few highest energies advocates the presence of nCN fission. It is observed from results that apart from the shell effects, the deformations of nascent fragments play crucial role for the evolution of fine-structure effects. Next, the mass dependence of fragment mass distribution is analyzed for the wide mass range of considered nuclei. A transition from symmetric fission to asymmetric fission is observed as one goes from lighter to heavier mass isotope. Finally, the energetically favoured fission fragments are identified for all the studied fissioning nuclei.

- At last, **Chapter 7** concludes the observations obtained from the present work of thesis. A short note about the importance of fission studies along with the scope of possible extension for future research work is also presented.

Bibliography

[1] F. Joliot and I. Curie, C. R. Acad. Sci. Paris **198**, 254 (1934); Nature **133**, 201 (1934).

[2] O. Hahn and F. Strassmann, Naturwiss. **27**, 11 (1939).

[3] L. Meitner and O. R. Frisch, Nature **143**, 239 (1939).

[4] N. Bohr and J. A. Wheeler, Phys. Rev. **56**, 426 (1939).

[5] W. F. Libby, Phys. Rev. **55**, 1269 (1939).

[6] G. N. Flerov and K. A. Petrzhak, Phys. Rev. **58**, 275 (1940).

[7] V. I. Kuznetsov, N. K. Skobelev and G. N. Flerov, Yad. Fiz. **4**, 279, (1966) [Sov. J. Nucl. Phys. **4**, 202 (1967)].

[8] V. I. Kuznetsov, N. K. Skobelev and G. N. Flerov, Yad. Fiz. **5**, 271 (1967) [Sov. J. Nucl. Phys. **5**, 191 (1967)].

[9] C. Wagemans, *The Nuclear Fission Process* (CRC Press, Boca Raton, FL) (1991).

[10] F. Hanappe, M. Lefort, C. Ngo, J. Peter and B. Tamain, Phys. Rev. Lett. **32**, 738 (1974).

[11] B. Borderie, M. Berlanger, D. Gardès, F. Hanappe, L. Nowicki, J. Péter, B. Tamain, S. Agarwal, J. Girard, C. Grégoire, J. Matuszek, C. Ngô, Z. Phys. A - Atoms and Nuclei **299**, 263 (1981).

[12] V. S. Ramamurthy, S. S. Kapoor, R. K. Choudhury, A. Saxena, D. M. Nadkarni, A. K. Mohanty, B. K. Nayak, S. V. Sastry, S. Kailas, A. Chatterjee, P. Singh and A. Navin, Phys. Rev. Lett. **65**, 25 (1990).

[13] R. L. Fleischer, P. B. Price, R. M. Walker and E. L. Hubbard, Phys. Rev. **143**, 943 (1966).

[14] K. H. Schmidt *et al.*, Nucl. Phys. A **665**, 221 (2000).

[15] J. E. Escher, J. T. Burke, F. S. Dietrich, N. D. Scielzo, I. J. Thompson and W. Younes, Rev. Mod. Phys. **84**, 353 (2012).

[16] L. Csige *et al.*, Phys. Rev. C **87**, 044321 (2013).

[17] S. M. Polikanov, V. Druin, V. Karnaukhov, V. Mikheev, A. Pleve, N. Skobelev, V. Subbotin, G. Ter-Akopyan and V. Fomichev, Zh. Eksp. Teor. Fiz. 42, 1464 (1962) [Sov. Phys. JETP 15, 1062 (1962)].

[18] L. Meitner, Nature **165**, 561 (1950).

[19] V. M. Strutinsky, Nucl. Phys. A **95**, 420 (1967).

[20] J. R. Nix, Nucl. Phys. A **130**, 241 (1969).

[21] I. V. Panov, E. Kolbe, B. Pfeiffer, T. Rauscher, K.-L. Kratz and F.-K. Thielemann, Nucl. Phys. A **747**, 633 (2005).

[22] Yu. Ts. Oganessian and V. K. Utyonkov, Nucl. Phys. A **944**, 62 (2015).

[23] R. A. Broglia, C. H. Dasso and Aa. Winther, Phys. Lett. B 53, 301 (1974).

[24] V. V. Samarin, Physics of Atomic Nuclei **72**, 1682 (2009).

[25] D. Shapira *et al.*, Phys. Rev. C **28**, 1148 (1983).

[26] B. B. Back, Phys. Rev. C **31**, 2104 (1985).

[27] B. B. Back *et al.*, Phys. Rev. C **53**, 1734 (1996); **32**, 195 (1985).

[28] V. Zagrebaev, A. Karpov and W. Greiner, J. Phys.: Conf. Ser **420**, 012001 (2013).

[29] V. Zagrebaev, A. Karpov and W. Greiner, EPJ Web of Conferences **86**, 00066 (2015).

[30] M. Trotta, A. M. Stefanini, S. Beghini, B. R. Behera *et al.*, Eur. Phys. J. A **25**, s01, 615 (2005).

[31] V. Yu. Denisov and S. Hofmann, Phys. Rev. C **61**, 034606 (2000).

[32] A. K. Nasirov, K. Kim, G. Mandaglio, G. Giardina, A. Muminov and Y. Kim, Eur. Phys. J. A **49**, 147 (2013).

[33] N. Bohr, Nature (London) **137**, 344 (1936).

[34] L. F. Canto, P. R. S. Gomes, R. Donangelo and M. S. Hussein, Phys. Rep. **424**, 1 (2006).

[35] N. Keeley, R. Raabe, N. Alamanos and J. L. Sidac, Prog. Part. Nucl. Phys. **59**, 579 (2007).

[36] N. Keeley, N. Alamanos, K. W. Kemper and K. Rusek, Prog. Part. Nucl. Phys. **63**, 396 (2009).

[37] G. Fazio *et al.*, J. Phys. Soc. Jpn. **74**, 307 (2005).

[38] G. Mandaglio, A. Anastasi, F. Curciarello, G. Fazio, G. Giardina and A. K. Nasirov, Phys. Rev. C **98**, 044616 (2018).

[39] A. K. Nasirov, B. M. Kayumov, G. Mandaglio, G. Giardina, K. Kim and Y. Kim, Eur. Phys. J. A **55**, 29 (2019).

[40] R. G. Thomas, R. K. Choudhury, A. K. Mohanty, A. Saxena and S. S. Kapoor, Phys. Rev. C **67**, 041601(R) (2003).

[41] U. L. Businaro and S. Gallone, Nuovo Cimento **5**, 315 (1957).

[42] K. Thomas, R. Davies and A. J. Sierk, Phys. Rev. C **31**, 915 (1985).

[43] H. Q. Zhang, C. L. Zhang, C. J. Lin, Z. H. Liu, F. Yang, A. K. Nasirov, G. Mandaglio, M. Manganaro and G. Giardina, Phys. Rev. C **81**, 034611 (2010).

[44] R. Rafiei, R. G. Thomas, D. J. Hinde, M. Dasgupta, C. R. Morton, L. R. Gasques, M. L. Brown, and M. D. Rodriguez, Phys. Rev. C **77**, 024606 (2008).

[45] D. J. Hinde, M. Dasgupta, J. R. Leigh, J. P. Lestone, J. C. Mein, C. R. Morton, J. O. Newton, and H. Timmers, Phys. Rev. Lett. **74**, 1295 (1995).

[46] S. Kailas, Phys. Rep. **284**, 381 (1997).

[47] V. S. Ramamurthy and S. S. Kapoor, Phys. Rev. Lett. **54**, 178 (1985).

[48] R. Vandenbosch and J. R. Huizenga, *Nuclear Fission* (Academic, New York, 1973).

[49] A. Kaur and M. K. sharma, Phys. Rev. C **99**, 044611 (2019).

[50] C. Ngo, C. Gregoire, B. Remaud and E. Tomasi, Nucl. Phys. A **400**, 259c (1983).

[51] G. Kaur and M. K. Sharma, Int. J. Mod. Phys. E **23**, 1450063 (2014).

[52] M. Morjean, D. Jacquet, M. Laget and J. F. Berger, J. Phys.: Conf. Ser. **282**, 012009 (2011).

[53] S. Bhattacharya *et al.*, EPJ Web Conf. **86**, 00004 (2015).

[54] A. Pulcini *et al.*, J. Phys.: Conf. Ser. **1014**, 012013 (2018).

[55] U. Mosel and H. W. Schmitt, Nucl. Phys. A **165**, 73 (1971).

[56] J. F. Berger, M. Girod and D. Gogny, Nucl. Phys. A **428**, 23 (1984)

[57] H. Nifenecker, G. Mariolopoulos, J. P. Bocquet, R. Brissot, M. Ch. Hamelin, J. Crancon and Ch. Ristori, Z. Phys. A **308**, 39 (1982).

[58] J. W. Negele, S. E. Koonin, P. Möller, J. R. Nix and A. J. Sierk, Phys. Rev. C **17**, 1098 (1978).

[59] T. Matsuse, C. Beck, R. Nouicer and D. Mahboub, Phys. Rev. C **55**, 1380 (1997).

[60] B. D. Wilkins, E. P. Steinberg, and R. R. Chasman, Phys. Rev. C **14**, 1832 (1976).

[61] S. J. Sanders, Phys. Rev. C **44**, 2676 (1991).

[62] S. J. Sanders *et al.*, Phys. Rev. C **40**, 2091 (1989).

[63] S. J. Sanders, A. Szanto de Toledo and C. Beck, Phys. Rep. **311**, 487 (1999).

[64] H. J. Fink, J. Maruhn,W. Scheid and W. Greiner, Z. Phys. **268**, 321 (1974).

[65] J. Maruhn and W. Greiner, Phys. Rev. Lett. **32**, 548 (1974).

[66] R. K. Gupta, W. Scheid and W. Greiner, Phys. Rev. Lett. **35**, 353 (1975).

[67] Niyti, G. Sawhney, M. K. Sharma and R. K. Gupta, Phys. Rev. C **91**, 054606 (2015).

Chapter 2

Methodology

2.1 Introduction

The contents related to formation of compound system and subsequent dynamics via competing fission processes along with the related structural and dynamical aspects have been discussed in the previous chapter. This nuclear process is still a conundrum for both theoretical as well as experimental researchers. Numerous theoretical framework have been applied in attempts to negotiate the intricacy of fission process, as briefed in section 1.6 of chapter 1. The full interpretation of nuclear structure and reaction dynamics involved in fission process is not yet fully understood, because it demands comprehensive knowledge of the forces associated with the collective motion of nucleons of reaction partners. The primary goal of this work is to investigate the spontaneous fission (SF), compound nucleus (CN) fission and non-compound nucleus (nCN) fission mechanisms, and the corresponding characteristics such as collective potential energy, fission fragment mass distribution and fission excitation functions etc. To fulfill this objective, the dynamical cluster-decay model (DCM) [1–10] is employed to study the decay properties of fissioning nuclei produced in nuclear reactions involving different kind of projectiles, such as light particles, heavy ions and radioactive ions. The analysis of decay dynamics is carried out for light and heavy nuclear systems at projectile energies around the Coulomb barrier. Therefore, the temperature T and angular momentum ℓ effects are introduced in the methodology along with the deformation and orientation degrees of freedom. DCM is based on the "quantum mechanical (or dynamical) fragmentation theory (QMFT)" [11–18], where the potential is computed within the Strutinsky macro-microscopic method [19] using two-center shell model (TCSM) [20]. DCM has property

of collective clusterization which treats all the decay processes (e.g. evaporation residue (ER), intermediate mass fragments (IMF) and fission fragments (ff)) on parallel footing. Note that this aspect of handling different decay processes at parallel footing is not available in majority of competing models.

DCM has been successfully applied for various CN and nCN decay processes in [1–10], which provide useful results in terms of fragmentation process and mass distributions. In the present work, apart from the study of CN and nCN fission, the application of DCM in terms of other competing decay channels is also examined. The fine structure effects among fission fragments are analyzed for several isotopes of pre-actinide and actinide nuclei at near and above barrier energies. Besides this, the fast fission (FF) process is also addressed in the DCM calculations.

In the subsequent sections 2.2 and 2.3, a brief description of DCM approach is dicussed. The T-dependent fragmentation potential is a key ingredient of dynamical model, which is obtained by using collective coordinates, explained in section 2.4. The preformation probability (P_0) of decay fragments is estimated using stationery Schrödinger equation in mass asymmetry coordinate, where fragmentation potential goes as input, see section 2.5. The preformation probability (P_0) provides an opportunity to analyze the mass division among decaying fragments, which further depends upon various factors, e.g., mass number, temperature, deformations, orientations etc. In section 2.6, the process of estimating penetration probability P of these nascent fragments through the potential barrier is described, in view of Wenzel-Kramers-Brillouin (WKB) approximation. The combine effect of P_0 and P can be seen in section 2.7 in terms of decay cross-sections. A description of nCN fission process and fission fragment mass anisotropy (A) are discussed in section 2.8 and 2.9 respectively. Finally, a method to estimate the spontaneous fission half-life times is briefed in section 2.10.

2.2 The dynamical cluster-decay model

The dynamical cluster-decay model (DCM) [1–10] is formulated using quantum mechanical fragmentation theory (QMFT) [11–18] for the charge and mass flow/transfer in nuclear decay processes by utilizing the idea of the charge ($\eta_Z = (Z_1 - Z_2)/(Z_1 + Z_2)$) and mass ($\eta_A = (A_1 - A_2)/(A_1 + A_2)$) asymmetry coordinates, which served as dynamical coordi-

nates in TCSM [20]. Subscripts 1 and 2 denote the heavy and light fragments. QMFT describes all two-body channels from which the composite system can be formed 'or' into which it can decay. The mass division of excited composite system has been explained by a dynamical treatment of collective asymmetry coordinates. Apart from asymmetry coordinate, another four coordinates used to define the nuclear shape, and thus the parameters of our potential are (i) relative separation coordinate R between the two nuclei, (ii) the neck-parameter ϵ ($=E_0/E^{'}$), where E_0 and $E^{'}$, represent, respectively actual and fixed barrier heights of two center oscillator. ϵ=0 demonstrate the broad neck formation, while ϵ=1 depicts the fully squeezed neck, corresponding to the asymptotic region. (iii) azimuthal angle ϕ between principal planes of interacting nuclear systems. (iv) deformations $\beta_{\lambda i}$ and orientations θ_i of two nuclei, where λ=2,3,4... and i=1, 2.

The fragmentation of two separated fragments/nuclei is determined using mass asymmetry, charge asymmetry and neutron asymmetry coordinates, given by

$$\eta_A = \frac{A_1 - A_2}{A_1 + A_2}, \eta_Z = \frac{Z_1 - Z_2}{Z_1 + Z_2}, \eta_N = \frac{N_1 - N_2}{N_1 + N_2}. \tag{2.1}$$

Two of above mentioned coordinates are sufficient to treat as dynamical coordinates, because they are connected with following relation

$$\eta = \frac{Z}{A}\eta_Z + \frac{N}{A}\eta_N. \tag{2.2}$$

Here A=A_1+A_2, Z=Z_1+Z_2 and N=N_1+N_2 are the mass number, charge number and neutron number of the CN, and A_i, Z_i and N_i (i=1, 2) represent the same but for two decaying fragments. The value of η-coordinate can vary between 0 and 1, and hence permits the unified description of few- and multi-nucleon transfer, large-mass transfer, the complete fusion ($|\eta| = 1$) of two nuclear systems, and the symmetric ($|\eta| = 0$,) asymmetric and super-asymmetric fission of composite system. The pictorial view of two deformed nuclei lying in the same plane (i.e. ϕ=0), can be seen in Fig. 2 of Ref. [21].

In DCM, the η and R coordinates, respectively, describe the nucleon division/exchange between decaying nuclei, and the transfer of the kinetic energy of the incident channel ($E_{c.m.}$) to the internal excitation. Here, internal excitation refers to the total excitation energy (TXE) or total kinetic energy (TKE)) of the outgoing fragments. The relation between these quantities can be expressed as

$$E^*_{CN} + Q_{out}(T) = TKE(T) + TXE(T). \tag{2.3}$$

The temperature (T) of hot CN having excitation energy (E^*_{CN}), is calculated within the semi-empirical statistical formula

$$E^*_{CN} = \frac{1}{a}AT^2 - T = E_{c.m.} + Q_{in}, \tag{2.4}$$

where a is the level density parameter that may vary between 7 to 11 depending on the mass number of the compound nucleus (A_{CN}). The entrance channel Q-value (i.e. Q_{in}) is given by $B.E._1 + B.E._2 - B.E._{CN}$, where $B.E.$'s represent the binding energies. In some of the thesis calculations, the T-dependence of the deformation parameter $\beta_{\lambda i}$ is also incorporated [22, 23], as shown below

$$\beta_{\lambda i}(T) = exp(-T/T_0)\beta_{\lambda i}(0), \tag{2.5}$$

where $\beta_{\lambda i}(0)$ known as static deformation. T_0=1.5 is the temperature of CN at which shell effects start disappearing [24]. The collective coordinates of fragmentation theory are further used to determine the kinetic (K) and potential (V) energy part of Hamiltonian, as discussed in the following section.

2.3 The Schrodinger wave equation and related Hamiltonian

The Hamiltonian is described by utilizing above mentioned collective coordinates, and its assessment given separately in terms of kinetic (K) energy and potential (V) energy:

$$H = K(R, \beta, \epsilon, \eta, \eta_Z; \dot{R}, \dot{\beta}, \dot{\epsilon}, \dot{\eta}, \dot{\eta_Z}) + V(R, \beta, \epsilon, \eta, \eta_Z), \tag{2.6}$$

For fixed orientation, the potential is minimized in the η_Z-coordinate, which further fixes the mass asymmetry coordinate and also the deformation parameter. The collective potential energy V, calculated within the Strutinsky renormalization method [19] by calculating the single particle energies of TCSM [20]. Thus, Schrödinger wave equation for the coupled η and R variables is given by

$$H(\eta, R)\psi(\eta, R) = E(\eta, R)\psi(\eta, R), \tag{2.7}$$

with Hamiltonian,

$$H(\eta, R) = K(\eta) + K(R) + K(\eta, R) + V(\eta) + V(R) + V(\eta, R). \tag{2.8}$$

In general, the η- and R-motions are taken as coupled, however, in the present approach, they are decoupled [11–13]. The coupling terms of kinetic and potential energies are neglected here, since the coupled cranking masses (B_{ij}, i,j=R,η) are negligibly small [11,13,25]. The Hamiltonian using the Pauli-Podolsky prescription [26] for the decoupled approximation, reads as

$$H = -\frac{\hbar^2}{2\sqrt{B_{\eta\eta}}}\frac{\partial}{\partial\eta}\frac{1}{\sqrt{B_{\eta\eta}}}\frac{\partial}{\partial\eta} - \frac{\hbar^2}{2\sqrt{B_{RR}}}\frac{\partial}{\partial R}\frac{1}{\sqrt{B_{RR}}}\frac{\partial}{\partial R} + V(\eta) + V(R) \tag{2.9}$$

Hence, the Schrödinger equation gets separated in η and R coordinates, and given by

$$\left\{-\frac{\hbar^2}{2\sqrt{B_{\eta\eta}}}\frac{\partial}{\partial\eta}\frac{1}{\sqrt{B_{\eta\eta}}}\frac{\partial}{\partial\eta} + V_R(\eta,T)\right\}\psi^\nu(\eta) = E^\nu\psi^\nu(\eta), \tag{2.10}$$

and

$$\left\{-\frac{\hbar^2}{2\sqrt{B_{RR}}}\frac{\partial}{\partial R}\frac{1}{\sqrt{B_{RR}}}\frac{\partial}{\partial R} + V_\eta(R,T)\right\}\psi^\nu(R) = E^\nu\psi^\nu(R), \tag{2.11}$$

with ν=0,1,2,3... referring to ground state (ν=0) and excited state ($\nu\neq$0) solutions. Assuming the Boltzmann-like function for each coordinate as

$$|\psi|^2 = \sum_{\nu=0}^{\infty}|\psi^\nu|^2 exp(-E^\nu/T). \tag{2.12}$$

The solutions $|\psi(\eta)|^2$ and $|\psi(R)|^2$ of Eq. (2.10) and (2.11), respectively, give the preformation P_0 and penetration P probability. In this work, P is estimated from WKB integral instead of solving Schrödinger equation (2.11) [27]. In Eq. (2.10), the $V_R(\eta,T)$ is the collective fragmentation potential defined in the following section.

2.4 The collective fragmentation potential

In recent years, the collective illustration of a composite system has been exploited for addressal of decay dynamics of numerous nuclear systems formed via heavy ion induced reactions. The major benefit of this approach is the use of collective Hamiltonian which permits a simple depiction of complicated 'many-body' phenomena. Although, the collective phenomenon is just a part of complete picture of the nuclear system, yet frequently the most striking and consequently the most basic and intriguing ones. In order to examine the dynamics engaged with the excited nuclear system, the temperature dependent collective potential energy (or fragmentation potential $V_R(\eta,T)$) has been calculated, which

is the key ingredient to the Schrödinger equation. By studying the deep valleys in the fragmentation potential plot at some η-values, the stability of decaying fragments is estimated. Therefore, the fragmentation potential $V_R(\eta, T)$ in terms of collective coordinates at fixed R=R_a (the entry point of penetration path, discussed ahead in section 2.6), is reads as

$$\begin{aligned} V_R(\eta,T) = \sum_{i=1}^{2}[V_{LDM}(A_i,Z_i,T)] + \sum_{i=1}^{2}[\delta U_i]exp(-T^2/T_0^2) \\ +V_C(R,Z_i,\beta_{\lambda i},\theta_i,T) + V_P(R,A_i,\beta_{\lambda i},\theta_i,T) \\ +V_\ell(R,A_i,\beta_{\lambda i},\theta_i,T). \end{aligned} \tag{2.13}$$

In Eq. (2.13), V_{LDM} and δU are respectively the macroscopic liquid drop model and microscopic shell correction parts of binding energy (B.E.), obtained by using the macro-microscopic re-normalization method of Strutinsky [19]. The T-dependent V_{LDM}(T) is taken from Davidson *et al.* [28], which is based on the semi-empirical mass formula of Seeger [29], as

$$\begin{aligned} V_{LDM}(A,Z,T) &= \alpha(T)A + \beta(T)A^{\frac{2}{3}} + \left(\gamma(T) - \frac{\eta(T)}{A^{\frac{1}{3}}}\right)\left(\frac{I^2+2|I|}{A}\right) \\ &+\frac{Z^2}{R_0(T)A^{\frac{1}{3}}}\left(1 - \frac{0.7636}{Z^{\frac{2}{3}}} - \frac{2.29}{[R_0(T)A^{\frac{1}{3}}]^2}\right) + \delta(T)\frac{f(Z,A)}{A^{\frac{3}{4}}}, \end{aligned} \tag{2.14}$$

where $I = a_a(Z-N)$, $a_a = 1.0$, and respectively, for even-even, even-odd, and odd-odd nuclei, $f(Z,A)$=(-1,0,1). In Ref. [30], the constants has been estimated at zero temperature, by fitting all even-even and 488 odd mass nuclei which are available at that time. Until now, a lot of data is accessible on ground-state B.E. Thus, the constants were re-adjusted [3] to obtain the experimental B.E. of Ref. [31] 'or' the theoretical estimates of Ref. [32] which don't exist in [31]. The T-dependent constants of Eq. (2.14) are obtained from Fig. 1 of Ref. [28], attained by fitting to the canonical ensemble average of the excitation energy of over 300 nuclei for T$\leq$4 MeV, extrapolated linearly for higher temperatures. Further, δU, the 'empirical' shell corrections, are obtained from Ref. [33] for spherical nuclei, expressed as

$$\delta U = C\left[\frac{F(N)+F(Z)}{(A/2)^{2/3}} - cA^{1/3}\right], \tag{2.15}$$

where

$$F(X) = \frac{3}{5}\left(\frac{M_i^{5/3} - M_{i-1}^{5/3}}{M_i - M_{i-1}}\right)(X - M_{i-1}) - \frac{3}{5}\left(X^{5/3} - M_{i-1}^{5/3}\right) \tag{2.16}$$

with X=N or Z, $M_{i-1} < X < M_i$ and M_i as the magic numbers. Here, constants C and c are 5.8 MeV and 0.26 respectively.

The symmetric fragmentation of fission process was successfully explained by the macroscopic LDM part of B.E. However, it missed to clarify that why fission happens in two unequal fragments. The consideration of microscopic shell corrections in the total potential certainly prompted the appearance of the asymmetric fission valleys [34]. The experimental measurements show a deep valleys at specific proton (Z) and/or neutron (N) numbers, pointing the existence of magic shell closures in fissioning nuclei. That means, the summation of microscopic δU and macroscopic V_{LDM} provides a appropriate explanation of the binding energies. The microscopic term δU strongly affected by the E^*_{CN} of nucleus (see Eq. (2.13)), and start fading at sufficiently higher energies [24]. Therefore, it was always of interest to investigate the complex interplay between microscopic and macroscopic part of potential energy and its relative dependence on incident beam energy. Apart from B.E. part of fragmentation potential, the knowledge of repulsive and attractive forces is also desired to understand the dynamics involved with different decay mechanisms. In Eq. (2.13), V_C, V_P and V_ℓ are, respectively, the Coulomb, nuclear proximity and centrifugal potentials for deformed and oriented nuclei, elaborated in the subsequent sections.

2.4.1 The Coulomb potential

The disintegration of compound nucleus may be viewed as a 'tug-of-war' between the Coulomb force of repulsion and attractive nuclear force. When repulsive force obtain a pivotal role, the splitting of compound nucleus takes place. The significance of repulsive Coulomb force can be determined from the nuclear fission process, where the dynamic picture of splitting relies upon the competition between the forces of surface interactions of the nuclei and the Coulomb interactions acting in the nucleus core. Such physical scenario provides an opportunity to understand the nuclear fission in more detail. The repulsive Coulomb potential (V_C) emerges due to the positive charge of the interacting/decaying nuclei. The repulsive potential between spherically symmetric nuclear systems is basically calculated using a simple expression, i.e., $V_C = Z_1 Z_2 e^2/R$. To obtain the Coulomb potential for the case of deformed and oriented nuclei, this expression is modified [35], and

reads as

$$V_c(Z_i,\beta_{\lambda i},\theta_i,\alpha_i,T) = \frac{Z_1Z_2e^2}{R(T)} + 3Z_1Z_2e^2\sum_{\lambda,i=1,2}\frac{1}{2\lambda+1}\frac{R_i^{\lambda}(\alpha_i,T)}{R(T)^{\lambda+1}}Y_{\lambda}^{(0)}(\theta_i) \times\Big[\beta_{\lambda i}+\frac{4}{7}\beta_{\lambda i}^2Y_{\lambda}^{(0)}(\theta_i)\Big], \quad (2.17)$$

$Y_{\lambda}^{(0)}(\theta_i)$ represents the spherical harmonics function. Higher the charge number of interacting nuclei, stronger is the Coulomb repulsion. As a consequence, nuclei are almost ready to fly apart, which gives rise to the nCN content. Note that the nuclear reactions with large Z_1Z_2 product, have more tendency to decay via nCN processes.

2.4.2 The nuclear proximity potential

The surface interactions between the nuclei/fragments have been analyzed in terms of proximity potential (V_P). The surface energy term is inadequate to describe the attractive forces between two nuclei, when the minimum distance between their surfaces is less than 2 fm, 'or' when a composite nuclear system is at the verge of separating into two parts. At that proximity region, an additional potential is needed to describe such attractive forces, and hence known as proximity potential. On the basis of the 'pocket formula' of Blocki *et al.* [36], the expression of proximity potential for two hot deformed/oriented nuclei with ϕ=0, given as [21]

$$V_P(A_i,\beta_{\lambda i},\theta_i,R,T) = 4\pi\bar{R}(T)\gamma b(T)\Phi(s_0(T)). \quad (2.18)$$

$b(T)(=0.99(1+0.009T^2))$ is the temperature dependent surface thickness, and the nuclear surface tension is calculated as $\gamma = 0.9517\left[1-1.7826\left(\frac{N-Z}{A}\right)^2\right] MeVfm^{-2}$. $\Phi(s_0)$ is known as universal function, dependent on the shortest distance of closest approach s_0 (refer Fig. 2 of Ref. [21]) and independent of shapes of nuclei,

$$\Phi(s_0) = \begin{cases} -\frac{1}{2}(s_0-2.54)^2 - 0.0852(s_0-2.54)^3; s_0 \le 1.2511 \\ -3.437exp(-\frac{s_0}{0.75}); s_0 \ge 1.2511. \end{cases} \quad (2.19)$$

$\bar{R}$ is the "mean curvature radius" of the two spherical reaction partners,

$$\bar{R} = \frac{R_1R_2}{R_1+R_2}, \quad (2.20)$$

with radius vectors R_i $(i=1,2)$

$$R_i(\alpha_i,T) = R_{0i}(T)\left[1+\sum_{\lambda}\beta_{\lambda i}Y_{\lambda}^{(0)}(\alpha_i)\right], \quad (2.21)$$

and T-dependent nuclear radii R_{0i} of the equivalent spherical nuclei [37],

$$R_{0i}(T) = [1.28A_i^{\frac{1}{3}} - 0.76 + 0.8A_i^{\frac{-1}{3}}](1 + 0.0007T^2)fm. \tag{2.22}$$

In terms of the radii of curvature R_{i1} and R_{i2} in the principal planes of curvature of each of the two nuclei (i=1, 2) at the points of closest approach, the mean curvature radius $\bar{R}$ for deformed, oriented nuclei is given as

$$\begin{aligned} \frac{1}{\bar{R}^2} &= \frac{1}{R_{11}R_{12}} + \frac{1}{R_{21}R_{22}} + \left[\frac{1}{R_{11}R_{21}} + \frac{1}{R_{12}R_{22}}\right] sin^2\phi \\ &+ \left[\frac{1}{R_{11}R_{22}} + \frac{1}{R_{21}R_{12}}\right] cos^2\phi. \end{aligned} \tag{2.23}$$

2.4.3 The centrifugal potential

The influence of angular momentum (ℓ) on fission dynamics has been studied in this thesis. Various CN and nCN decay mechanisms strongly depend on the ℓ-values. Hence, the incorporation of rotational energy 'or' centrifugal potential in the collective fragmentation potential is essential. The centrifugal potential arises due to the rotational motion of nuclear system. It has been observed that the fission probability increases for the case of rotating system as compared to non-rotating one. Therefore, the rotational energy has critical significance in the fission dynamics, and calculated using following relation

$$V_\ell(A_i, T, \beta_{\lambda i}, \theta_i, \alpha_i) = \frac{\hbar^2\ell(\ell+1)}{2I(T)}. \tag{2.24}$$

The moment of inertia $I(T)$ can be defined in two ways

(i) Sticking (I_S) limit of moment of inertia [38]

$$I_S(T) = \mu R^2 + \frac{2}{5}A_1 m R_1^2(\alpha_1, T) + \frac{2}{5}A_2 m R_2^2(\alpha_2, T), \tag{2.25}$$

where, μ=$m\frac{A_1A_2}{A_1+A_2}$ is the reduced mass, with m as the nucleon mass. R_i taken from Eqs. (2.21) and (2.22).

(ii) Non-sticking (I_{NS}) choice of moment of inertia [39]

$$I_{NS}(T) = \mu R^2. \tag{2.26}$$

It is worth noting that, the decay cross-sections within DCM approach are generally estimated using the sticking-limit of moment of inertia (I_S). In the sticking choice of I, the touching nuclei rotate around their common center-of-mass. This choice of moment of inertia is attributed to the use of proximity potential [36]. However, the non-sticking limit (I_{NS}) is favoured for fission fragment anisotropies (A) calculations (discussed in section 2.9), where no intrinsic rotation of nuclei is taken into consideration due to small separation between them. Note that the non-sticking limits are generally used to determine the experimental ℓ value. In this work, the angular momentum dependence of CN and nCN fission has been explored, and the results are discussed in chapter 4 and 5.

2.5 The preformation probability

The preformation probability (P_0) is the solution of the Schrödinger wave equation (2.10) in mass asymmetry coordinate, using fragmentation potential as a input, at R=R$_a$ (see section 2.6), obtained as

$$P_0(A_2) \propto |\psi^{\nu}(A_2)|^2 \tag{2.27}$$

Here $\nu = 0, 1, 2...$, referring to ground state and excited state solutions. The lowest vibrational ν=0 is taken for the ground state decays. Then, the mass (or charge) distribution yield which is proportional to the probability $|\psi^0(\eta)|^2$ (or$|\psi^0(\eta_Z)|^2$) is scaled to say, mass A$_2$ of one of the fragments ($d\eta$=2/A) and it is given by:

$$P_0 = |\psi(\eta(A_i))|^2 \sqrt{B_{\eta\eta}} \frac{2}{A_{CN}}, \tag{2.28}$$

In Eq. (2.28), $B_{\eta\eta}$ is the mass parameter used to define the kinetic energy term. In the present work, simple classical model given by Kröger and Scheid for mass transfer in heavy ion collision [40] is used to account for hydrodynamical mass parameter $B_{\eta\eta}$, which read as

$$B_{\eta\eta} = \frac{AmR^2}{4} \left[\frac{v_t(1+\gamma)}{v_c(1+\delta^2)} - 1 \right], \tag{2.29}$$

with

$$\gamma = \frac{R_c}{2R} \left[\frac{1}{1+\cos\vartheta_1} \left(1 - \frac{R_c}{R_1}\right) + \frac{1}{1+\cos\vartheta_2} \left(1 - \frac{R_c}{R_2}\right) \right], \tag{2.30}$$

$$\delta = \frac{1}{2R} \left[(1-\cos\vartheta_1)(R_1 - R_c) + (1-\cos\vartheta_2)(R_2 - R_c) \right], \tag{2.31}$$

$$v_c = \pi R_c^2 R. \tag{2.32}$$

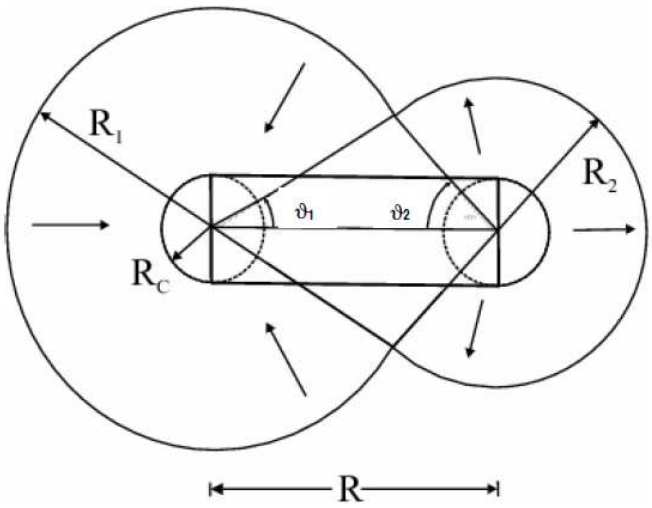

Figure 2.1: The geometrical representation of the two interacting nuclei as considered in the classical hydrodynamical model of [40]

In Eq. (2.29), v_t ($=v_1 + v_2$) is the total conserved volume. For two touching sphere $\vartheta_1 = \vartheta_2 = 0$, $\delta = 0$. The radius of a cylinder $R_c(\neq 0)$ of length R is assumed for the mass transfer between the two spherical fragments, having a homogeneous flow in it (see Fig. 2.1).

2.6 The barrier tunneling probability

The barrier tunneling probability 'or' the penetrability P of preformed fragments/clusters across the potential barrier is determined by utilizing the Wenzel-Kramers-Brillouin (WKB) approximation. Instead of solving the radial Schrödinger equation (2.11) in R coordinate, the penetrability is calculated using WKB integral analytically by parameterizing the potential V(R), as described below:

$$V(R) = \begin{cases} a_1 R + a_2 R^2; & R_0 \leq R \leq R_t \\ V_C + V_P + V_\ell; & R \geq R_t. \end{cases} \tag{2.33}$$

In above equation, for $R < R_t$, $V(R)$ is parameterized using a polynomial of second order in R-coordinate for each η-value. However, the potential $V(R)$ for $R \geq R_t$ is obtained by using scattering potential (i.e. sum of Coulomb, proximity and centrifugal potential $V(R) = V_C + V_P + V_\ell$). A typical scattering potential, calculated for fission reaction ^{227}Pa$^*\rightarrow{}^{92}$Sr+^{135}I is shown in Fig. 2.2, along with the turning points. The constants a_i (i=1,2) present in the polynomial are estimated by using boundary conditions as mentioned below:

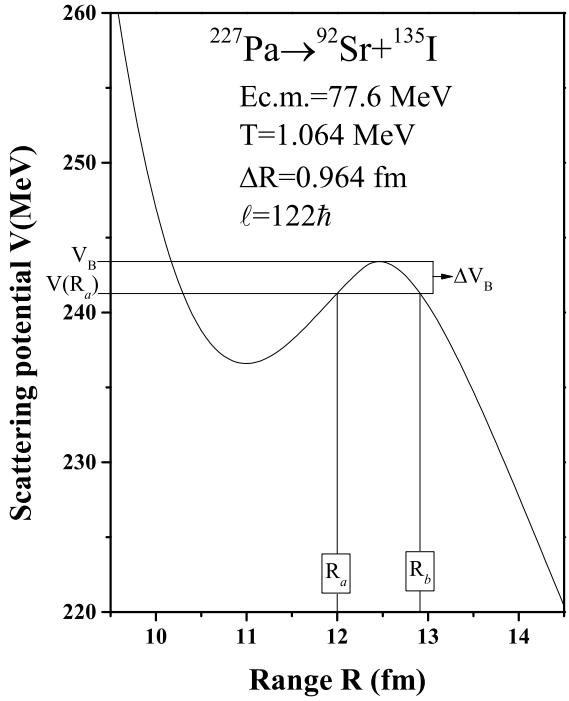

Figure 2.2: The scattering potential V(R) for the fission decay of ^{227}Pa* compound nucleus, with other marked quantities.

(i) At $R = R_0$, $V(R) = Q$

(ii) At $R = R_t$, $V(R) = V(R_t)$

The penetrability P of fragments decaying from the excited compound nucleus, is given by

$$P = \exp\left[-\frac{2}{\hbar}\int_{R_a}^{R_b}\{2\mu[V(R) - Q_{eff}]\}^{1/2}dR\right]. \tag{2.34}$$

Here, V(R), Q_{eff} and TKE are, respectively, scattering potential, effective Q-value and total kinetic energy of decay process. Ref. [41] suggests that the magnitude of hydrodynamical mass parameter B_{RR} is nearly similar to the reduced mass μ for the outgoing channel within the phenomenological approach based on incompressible irrotational flow. Hence, the WKB integral is solved analytically using reduced mass μ instead of B_{RR} for the estimation of penetrability. R_a and R_b are the two turning points of penetration path, satisfying

$$V(R_a) = V(R_b) = Q_{eff} = TKE(T). \tag{2.35}$$

$V(R_a)$ and $V(R_b)$ describes the scattering potential experienced by the fragment during first and second turning points of the barrier as shown in Fig. 2.2. R_a is obtained by using following relation

$$\begin{aligned} R_a &= R_1(\alpha_1, T) + R_2(\alpha_2, T) + \Delta R(\eta, T) \\ &= R_t(\alpha_i, T) + \Delta R(\eta, T), \end{aligned} \tag{2.36}$$

where, R_i and R_{0i} are defined in earlier Eqs. (2.21) and (2.22). The "neck length parameter (ΔR)" is the relative separation between two nuclei, used to incorporate the neck effects in decaying fragments in somewhat similar way as done in TCSM [20]. This choice of neck criteria is like the one adopted in scission point [42, 43] and saddle point [44–46] statistical models for addressing ER and fission decay modes. The choice of ΔR for the best fit to the data allows us to define the effective "barrier-lowering" parameter ΔV_B (see Fig. 2.2) for each ℓ-value as the difference between the actual barrier used, $V(R_a, \ell)$, and the calculated barrier $V_B(\ell)$, as

$$\Delta V_B(\ell) = V(R_a, \ell) - V_B(\ell). \tag{2.37}$$

ΔV_B is defined as a negative quantity which means that the actually used barrier is effectively lowered. This in-built parameter of DCM plays important role to address of fission excitation functions.

2.7 Decay cross-sections

Using the preformation P_0 and penetration P probability obtained within decoupled approximation to η- and R-motions, the CN decay or fragment's formation cross-sections are calculated, in terms of partial wave analysis, as

$$\sigma(A_1, A_2) = \frac{\pi}{k^2} \sum_{\ell=0}^{\ell_{max}} (2\ell + 1) P_0 P; \quad k = \sqrt{\frac{2\mu E_{c.m.}}{\hbar^2}}. \tag{2.38}$$

Here, μ=$mA_1A_2/(A_1+A_2)$ is the reduced mass, and ℓ_{max} is maximum angular momentum fixed where the cross-sections of light particles (or evaporation residue) become negligibly small. The collective clusterization process within the domain of DCM is used, and calculated the excitation function of evaporation residue (σ_{ER}), intermediate mass fragments (σ_{IMF}), symmetric and asymmetric fission fragments (σ_{ff}) etc. Following equation (2.38),

the cross-sections of evaporation residue and fusion-fission mechanisms (i.e. σ_{ER} and σ_{ff}) are calculated as

$$\sigma_{ER} = \sum_{A_2=1}^{4} \sigma(A_1, A_2); \quad \sigma_{ff} = 2 \sum_{A_2=A/2-20}^{A/2} \sigma(A_1, A_2), \tag{2.39}$$

giving cross-sections of CN decay $\sigma_{CN} = \sigma_{ER} + \sigma_{ff}$.

2.8 Non-compound nuclear fission

After discussing the collective clusterization approach of DCM methodology along with the T- and ℓ-effects, it is concluded that DCM approach can be used to address the excitation functions of various compound nucleus (CN) processes over a wide mass and energy range. In recent years, an evolution of heavy ion induced reactions in terms of non-compound nucleus reactions has taken place. Hence, it is worth studying such nuclear reactions within the framework of collective clusterization criteria. The pursuit of such reaction mechanisms requires the inclusion of some characteristic features of nCN fission. As discussed in previous chapter, the hinderance in the formation of CN can be addressed in terms of nCN cross-sections (excitation functions) (σ_{nCN}) which may involve contributions from quasi fission (QF) and fast fission (FF) processes, i.e. σ_{nCN}=σ_{QF}+σ_{FF}. Note that the excitation functions are obtained using partial wave analysis as described in Eq. (2.38 and 2.39). In the case of quasi fission (QF), the projectile is captured by target, and a non-equilibrated composite system (called di-nuclear system) is formed, which traps into the potential well for very short time. In this case, multi-nucleon transfer takes place, and formed composite system re-separates at faster pace (as compared to equilibrated CN), and hence projectile like fragments appear in the exit channel, and QF is observed. In DCM based calculations, the QF contributions are calculated by considering preformation probability equal to unity for the entrance channel [47], since for quasi fission the target and projectile systems are supposed to retain their identity [48, 49]. The penetration probability (P_{ic}) is calculated as for the decay fragments identical to incoming channel using WKB approximation, and then QF cross-section, reads as

$$\sigma_{QF} = \frac{\pi}{k^2} \sum_{\ell=0}^{\ell_{max}} (2\ell + 1) P_{ic}. \tag{2.40}$$

Further, in the case of fast fission (FF) process, a mononucleus is formed that survived QF. The angular momentum of mononucleus is much large. The fission barrier (Bf) of this rotating system disappears at large value of angular momentum due to higher rotational energy [50]. Thus, hot and rotating nucleus undergoes fast fission, and results in the generation of fission fragments similar to those in fusion-fission (ff) process. Note that fast fission products has alike properties as that of usual ff fragments [51]. Here, P_0 is calculated by solving equation (2.10) for fission fragments for angular momentum values varying from ℓ_{Bf} to ℓ_{max} (ℓ_{Bf} is an angular momentum, where fission barrier disappears). Here, barrier penetration probability is considered to be maximum (i.e. P=1) in agreement with the Ref. [52]. Thus, the fast fission contributions are calculated using following formula

$$\sigma_{FF} = \frac{\pi}{k^2} \sum_{\ell_{Bf}}^{\ell_{max}} (2\ell + 1) P_0. \tag{2.41}$$

Chapter 4 deals with study of QF and FF mechanisms investigated for actinide nucleus ^{216}Th* produced in heavy-ion induced reaction.

2.9 Fission fragment anisotropy using standard saddle-point statistical model

Fission fragment anisotropy (A) is a successful tool to explore the presence/absence of CN and nCN fission mechanisms in heavy-ion induced reactions. In the present work, the standard saddle-point statistical model (SSPSM) [53] is employed to calculate the fission anisotropy by utilizing DCM obtained quantities for the non-sticking choice of moment of inertia. A relation of fission anisotropy with other parameters is given by

$$A = 1 + < \ell^2 > /4K_0^2, \tag{2.42}$$

In the equation above, $< \ell^2 >$ is the mean square angular momentum of fissioning nucleus related to the total ℓ value (equivalently, ℓ_{max} of the CN). K_0^2 is the variance of the K distribution, and reads as

$$K_0^2 = T \times I_{eff}/\hbar^2. \tag{2.43}$$

Here, T is the temperature of CN. I_{eff}, the effective moment of inertia is obtained by utilizing the finite-range rotating liquid drop model [54]. Within SSPSM approach, it is

assumed that the fission fragments may decay towards the symmetry axis of the compound system and the projection of the total angular momentum on this axis is conserved from saddle to scission point. For heavier nuclear systems, this assumption may not be justified due to the different nuclear configurations at these points. Therefore, SSPSM-calculated fission anisotropies show anomalous behaviour with regard to experimental measured one, which indicates the existence of nCN contributions, e.g. quasi fission and fast fission.

2.10 Spontaneous fission half-lives

In this thesis , chapter 3 represents the study of spontaneous fission (SF) of superheavy nuclei (SHN) appearing as end product in the alpha decay chains of another isotopes of SHN. The SF half-lives ($T_{1/2}$) are calculated using DCM for non-rotating (ℓ=0), recoiled nuclei [55]. Since the residual nucleus is considered to be 'hot' due to its measured recoil energy E_R, the temperature T-effects have been incorporated here, with T (in MeV) for the SF of SHN coming into picture via its excitation energy (E_R^*) as

$$E_R^* = \frac{1}{a}AT^2 - T = E_R - Q_\alpha. \tag{2.44}$$

Here, a=10 for the study of spontaneous fissioning SHN, and Q_α denotes the Q-value of the alpha decaying nucleus preceding to the SF nucleus. Note that Q-value has been taken negative, considering that energy is required for SF decay of a superheavy nucleus.

In DCM, the decay constant λ (related to half-life $T_{1/2}$) is the product of three factors: the fragment preformation probability P_0, the barrier impinging frequency ν_0 and the barrier penetration probability P, given by the relation

$$\lambda = \nu_o P_0 P; \qquad T_{1/2} = ln2/\lambda. \tag{2.45}$$

Here, P_0 and P are calculated using methods presented in sections 2.5 and 2.6 for ℓ=0 (i.e. s-wave) case. Note that, the previous study [55] of alpha decay chains have successfully explained the experimental measurements. Therefore, it is quite interesting to see if the same DCM for ℓ=0 case, would explain the SF of SHN, and the results are presented in the next chapter.

After a brief layout of processes and methods adopted for addressal of fusion-fission dynamics and related non-compound nuclear components, the results based on collective fragmentation analysis are presented in chapters 3 to 7.

Bibliography

[1] R. K. Gupta, R. Kumar, N. K. Dhiman, M. Balasubraniam, W. Scheid and C. Beck, Phys. Rev. C **68**, 014610 (2003).

[2] M. Balasubramaniam, R. Kumar, R. K. Gupta, C. Beck and W. Scheid, J. Phys. G: Nucl. Part. Phys. **29**, 2703 (2003).

[3] B. B. Singh, M. K. Sharma and R. K. Gupta, Phys. Rev. C **77**, 054613 (2008).

[4] M. K. Sharma, G. Sawhney, R. K. Gupta and W. Greiner, J. Phys. G: Nucl. Part. Phys. **38**, 105101 (2011).

[5] M. Kaur, R. Kumar and M. K. Sharma, Phys. Rev. C **85**, 014609 (2012); M. Kaur and M. K. Sharma, Eur. Phys. J. A **50**, 61 (2014).

[6] G. Sawhney and M. K. Sharma, Eur. Phys. J. A **48**, 57 (2012); M. K. Sharma, S. Kanwar, G. Sawhney and R. K. Gupta, Phys. Rev. C **85**, 064602 (2012); G. Sawhney, R. Kumar and M. K. Sharma, Phys. Rev. C **86**, 034613 (2012).

[7] G. Kaur and M. K. Sharma, Nucl. Phys. A **884** 36 (2012); Phys. Rev. C **87**, 044601 (2013); Int. J. Mod. Phys. E **23**, 1450063 (2014).

[8] Rajni, R. Kumar and M. K. Sharma, Phys. Rev C **90**, 044604 (2014); Rajni, G. Kaur and M. K. Sharma, Int. J. Mod. Phys. E **25**, 1650091 (2016).

[9] G. Kaur, K. Sandhu and M. K. Sharma, Phys. Rev. C **94**, 014615 (2016). G. Kaur, K. Sandhu, A. Kaur and M. K. Sharma, Phys. Rev. C **97**, 054602 (2018).

[10] A. Kaur, G. Sawhney and M. K. Sharma, Int. J. Mod. Phys. E **27**, 1850043 (2018); A. Kaur, K. Sandhu and M. K. Sharma, Commun. Theor. Phys. **70**, 565 (2018); A. Kaur and M. K. Sharma, Phys. Rev. C **99**, 044611 (2019).

[11] J. Maruhn and W. Greiner, Phys. Rev. Lett. **32**, 548 (1974).

[12] H. J. Fink, W. Greiner, R. K. Gupta, S. Liran, J.H. Maruhn, W. Scheid and O. Zohni, in Proceedings of Int. Conf. on Reaction between Complex Nuclei, Nashville, (Amsterdam: North Holland), **21**, pages 2 (1974).

[13] R. K. Gupta, W. Scheid and W. Greiner, Phys. Rev. Lett. **35**, 353 (1975).

[14] S. Yamaji, W. Scheid, H. J. Fink and W. Greiner, Z. Phys. A **278**, 69 (1976); S. Yamaji, W. Scheid, H. J. Fink and W. Greiner, J. Phys. G: Nucl. Phys. **2**, L189 (1976); S. Yamaji, K. H. Ziegenhain, H. J. Fink, W. Greiner and W. Scheid, J. Phys. G: Nucl. Phys. **3**, 1283 (1977).

[15] R. K. Gupta, A. Sandulescu and W. Greiner, Z. Naturforsch, **32a**, 704 (1977); R. K. Gupta, C. Pirvulescu, A. Sandulescu and W. Greiner, Z. Phys. A **283**, 217 (1977); Sovt. J. Nucl. Phys. **28**, 160 (1978); R. K. Gupta, Z. Phys. A **281**, 159 (1977).

[16] A. Sandulescu, R. K. Gupta, W. Scheid and W. Greiner, Phys. Lett. B **60**, 225 (1976); R. K. Gupta, A. Sandulescu and W. Greiner, Phys. Lett. B **67**, 257 (1977); Rev. Roum. Phys. **23**, 51 (1978).

[17] R. K. Gupta, IANCAS Bull. (India), **6**, 2 (1990).

[18] A. Sandulescu, H. J. Lustig, J. Hahn and W. Greiner, J. Phys. G: Nucl. Phys. **4**, L279 (1978); H. J. Lustig, J. A. Maruhn and W. Greiner, J. Phys. G: Nucl. Phys. **6**, L25 (1980).

[19] V. M. Strutinsky, Nucl. Phys. A **95**, 420 (1967).

[20] J. Maruhn and W. Greiner, Z. Physik **251**, 431 (1972).

[21] R. K. Gupta, N. Singh and M. Manhas, Phys. Rev. C **70**, 034608 (2004).

[22] M. Muenchow and W. Scheid, Phys. Lett. B **162**, 265 (1985); Nucl. Phys. A **468**, 59 (1987).

[23] M. Rashdan, A. Faessler and W. Waida, J. Phys. G: Nucl. Part. Phys. **17**, 1401 (1991).

[24] A. S. Jensen and J. Damgaard, Nucl. Phys. A **203**, 578 (1973).

[25] D. R. Saroha and R. K. Gupta, J. Phys. G: Nucl. Phys. **12**, 1265 (1986).

[26] W. Pauli, in *Handbuck der Physik*, Part I, edited by H. Geiger and K. Sheel (Springer, Berlin, 1933), Vol. **24**, p. 120; B. Padolsky, Phys. Rev. 32, 812 (1928); J. Eisenberg and W. Greiner, *Nuclear Models* (North Holland, Amsterdam, 1971).

[27] S. S. Malik and R. K. Gupta, Phys. Rev. C **39**, 1992 (1989).

[28] N. J. Davidson, S. S. Hsiao, J. Markram, H. G. Miller and Y. Tzeng, Nucl. Phys. A **570**, 61c (1994).

[29] P. A. Seeger, Nucl. Phys. **25**, 1 (1961).

[30] S. DeBenedetti, Nuclear Interactions (New York: Wiley) (1964).

[31] G. Audi, A. H. Wapstra and C. Thiboult, Nucl. Phys. A **729**, 337 (2003).

[32] P. Möller, J. R. Nix, W. D. Myers and W. J. Swiatecki, At. Data Nucl. Data Tables **59**, 185 (1995).

[33] W. Myers and W. J. Swiatecki, Nucl. Phys. **81**, 1 (1966).

[34] U. Brosa, S. Grossmann and A. Müller, Phys. Rep. **197**, 167 (1990).

[35] R. K. Gupta, M. Balasubramaniam, R. Kumar, N. Singh, M. Manhas and W. Greiner, J. Phys. G: Nucl. Part. Phys. C **31**, 631 (2005).

[36] J. Blocki, J. Randrup, W. J. Swiatecki and C. F. Tsang, Ann. Phys. (NY) **105**, 427 (1977).

[37] G. Royer and J. Mignen, J. Phys. G: Nucl. Part. Phys. **18**, 1781 (1992).

[38] N. Cindro and D. Pocanic, J. Phys. G: Nucl. Part. Phys. **6**, 359 (1980).

[39] R. Aroumougame, N. Malhotra, S. S. Malik and R. K. Gupta, Phys. Rev. C **35**, 3 (1987).

[40] H. Kröger and W. Scheid, J. Phys. G **6**, L85 (1980).

[41] D. N. Poenaru, R. A. Gherghescu and W. Greiner, Eur. Phys. J. A **24**, 355 (2005).

[42] T. Matsuse, C. Beck, R. Nouicer and D. Mahboub, Phys. Rev. C **55** (1997) 1380.

[43] B. D. Wilkins, E. P. Steinberg and R. R. Chasman, Phys. Rev. C **14** 1832 (1976).

[44] S. J. Sanders, Phys. Rev. C **44**, 2676 (1991).

[45] S. J. Sanders *et al.*, Phys. Rev. C **40**, 2091 (1989).

[46] S. J. Sanders, A. Szanto de Toledo and C. Beck, Phys. Rep. **311**, 487 (1999).

[47] R. Kumar, M. Bansal, S. K. Arun and R. K. Gupta, Phys. Rev. C **80**, 034618 (2009).

[48] B. B. Back *et al.*, Phys. Rev. C **53**, 1734 (1996); **32**, 195 (1985).

[49] B. B. Back, Phys. Rev. C **31**, 2104 (1985).

[50] B. Borderie, M. Berlanger, D. Gardes, F. Hanappe, L. Nowicki, J. Peter, B. Tamain, S. Agarwal, J. Girard, C. Gregoire, J. Matuszek and C. Ngo, Z. Phys. A **299**, 263 (1981).

[51] A. K. Nasirov, K. Kim, G. Mandaglio, G. Giardina, A. Muminov and Y. Kim, Eur. Phys. J. A **49**, 147 (2013).

[52] S. S. Kapoor and V. Ramamurthy, Pramana J. Phys. **33**, 161 (1989).

[53] R. Vandenbosch and J. R. Huizenga, *Nuclear Fission* (Academic, New York, 1973).

[54] A. J. Sierk, Phys. Rev. C 33, 2039 (1986).

[55] Niyti, G. Sawhney, M. K. Sharma and R. K. Gupta, Phys. Rev. C **91**, 054606 (2015).

Chapter 3

Spontaneous fission of superheavy nuclei

3.1 Introduction

Following the discovery of spontaneous fission (SF) of ^{238}U [1], a number of heavy and superheavy nuclei (SHN) exhibiting this type of radioactive decay were reported, and their respective half-life times were measured by different laboratories [2,3]. Importantly, the half-life times of such processes can be considered as experimental evidence of the formation of SHN in a nuclear reaction. The SHN are mainly identified by the sequential α-decay chain from unknown (unstable) nuclei to known (stable) nuclei. The final product of these chains may decay via α or SF process. Apparently, both SF and α-decay act as a decisive factor for the overall existence of SHN. The SF and it's related aspects find crucial relevance and importance to figure out the dynamical behavior of parent nuclei, especially in the superheavy mass region. Recently, a systematic study of α-decay chains of several isotopes of SHN with Z=113 to 118 has been carried out [4]. In this study, the α-decay half lives ($T^{\alpha}_{1/2}$) were calculated by employing dynamical cluster-decay model (DCM) for non-rotating (ℓ=0) recoiled nuclei (see section 2.10 of chapter 2), which found decent agreement with the experimental measurements. Note that the recoiled SHN arises as a result of x-neutrons (x=2-4) emission from a compound nucleus (CN) formed in heavy ion induced reactions.

As mentioned earlier, some α-decay chains end in spontaneous fissioning nuclei, like $^{266}_{103}$Lr to $^{282}_{112}$Cn from Z=113 to 118 nuclei, and it was of interest to see if DCM for ℓ=0 case [4], would explain the measured SF data [5–10]. These spontaneous fissioning nuclei appear as end products in the α-decay chains of various isotopes of Z=113-118 SHN

formed in hot-fusion reactions [5–10], after xn-emission. Note that the heaviest nucleus observed till now is Z=118, even though the synthesis of elements 119 and 120 were attempted [11,12], using projectiles heavier than ^{48}Ca, but with no decay chains of parent nuclei or their descendants were observed in these experiments. Motivated by previous study [4] of α-decay chains, the eight considered cases of *spontaneous fissioning nuclei*, analyzed here in this chapter, are as listed below:

1. $^{266}_{105}$Db occurring as the end product of the α-decay chain of SHN ^{282}113, formed via ^{237}Np+^{48}Ca reaction after 3n emission.

2. $^{267}_{104}$Rf occurring as the end product of the α-decay chain of SHN ^{287}114, formed via ^{242}Pu+^{48}Ca reaction after 3n emission.

3. $^{267}_{105}$Db occurring as the end product of the α-decay chain of SHN ^{287}115, formed via ^{243}Am+^{48}Ca reaction after 4n emission.

4. $^{268}_{105}$Db occurring as the end product of the α-decay chain of SHN ^{288}115, formed via ^{243}Am+^{48}Ca reaction after 3n emission.

5. $^{267}_{104}$Rf occurring as the end product of the α-decay chain of SHN ^{291}116, formed via ^{245}Cm+^{48}Ca reaction after 2n emission.

6. $^{281}_{111}$Rg occurring as the end product of the α-decay chain of SHN ^{293}117, formed via ^{249}Bk+^{48}Ca reaction after 4n emission.

7. $^{266}_{103}$Lr occurring as the end product of the α-decay chain of SHN ^{294}117, formed via ^{249}Bk+^{48}Ca reaction after 3n emission.

8. $^{282}_{112}$Cn occurring as the end product of the α-decay chain of SHN ^{294}118, formed via ^{249}Cf+^{48}Ca reaction after 3n emission.

The end products of the above considered α-decay chains are reported to have a 100% spontaneous fissioning component [5–10]. The outcomes of this investigation are published in Refs. [13–15].

The temperature effects arise here in view of the measured recoil energy E_R of SHN, left after certain neutrons disintegrate from the CN. The main difference between earlier

study of α-decay chains ending in an α-decaying nucleus [4] and the present one ending in a SF nucleus, is that in the former case, energy was expected to release via the α-emission of the nucleus, the Q_α-value, such that the excitation energy of the recoiled SHN/ or the relevant nucleus $E_R^* = E_R + Q_\alpha$ at each step in the α-decay chain. On the other hand, considering that energy is required for the SF of a nucleus, $E_R^* = E_R - Q_\alpha$ in the present case of the ending nucleus as a SF nucleus. Here, Q_α refers to Q-value of the α-decaying nucleus preceding to the SF nucleus. The average measured recoil energies (E_R) are 10.5, 11.5 and 12.5 MeV, respectively, for the decay chains of (a) ^{287}114, (b) ^{282}113, ^{287}115, ^{288}115, ^{291}116, ^{293}117, and (c) ^{294}117, ^{294}118 SHN [5–10].

In this work, a relative analysis of two decay modes of SHN; such as α-decay and SF for the DCM(ℓ=0) is investigated in reference to measured [5–10] data and other available theoretical calculations [16–18]. The calculated SF half-lives, within one parameter fit of the first turning point R_a or neck-length ΔR, match the experimental data nicely. The study explored a complete survey of fragmentation potential, preformation and penetration probability for the two processes (SF and α-decay). The influence of deformations/orientations and shell corrections on the SF decay is duly incorporated. The details of results are discussed in section underneath.

3.2 Calculations and results

An overview of this section is as per the following: Section 3.2.1 represents the study of barrier characteristics for the two cases of an α-decay chain ending in α-decaying or SF nucleus, and then the preformation probability P_0, penetrability P and finally the half-lives $T_{1/2}$ for the spontaneous fission and α-decay processes. The calculations also provide the opportunity to examine the fission fragment mass distributions and to identify the most probable fragments, the relevant results are shown in section 3.2.2. Note that the fission fragments are not identified in experiments [5–10], hence such analysis is of extreme relevance and importance. The calculations are made for ℓ=0 case of β_2-deformed fragments. For the orientations [19], both "hot, compact" and "cold, elongated" configurations are explored. Furthermore, section 3.2.3 represents the possible role of shell closure effects in the SF process, that arise due to the nuclear structure effects in fragmentation potential or equivalently the preformation factor. Finally, the conclusions

of this study are summarized in section 3.3.

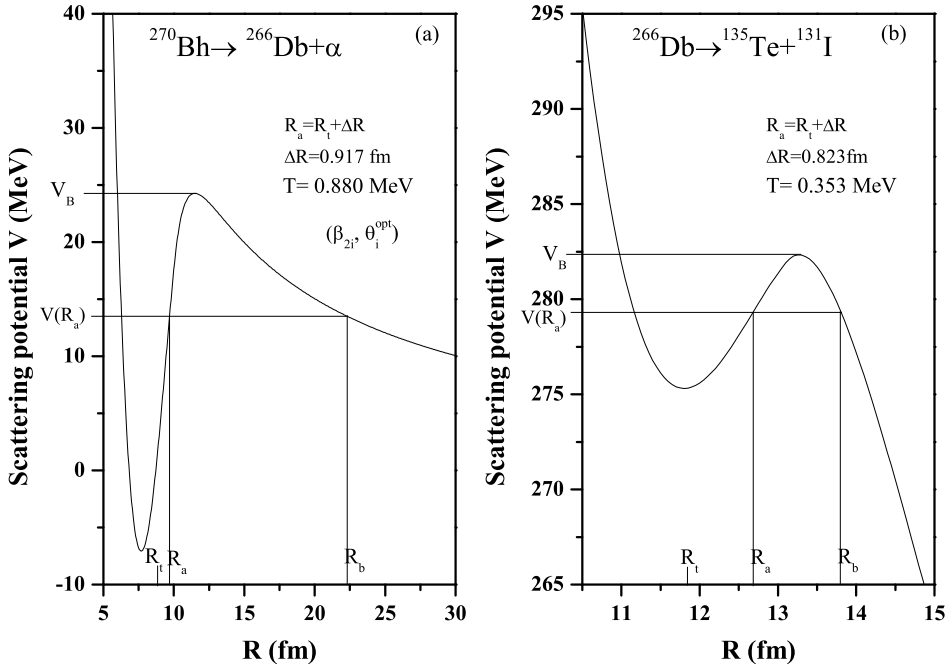

Figure 3.1: The interaction potential for the decay of (a) ^{270}Bh→^{266}Db+α and (b) ^{266}Db→^{135}Te+^{131}I using deformed choice of fragments. Here ^{270}Bh is the preceding α-decaying nucleus, and ^{266}Db is the end product of the decay chain of ^{282}113 SHN.

3.2.1 SF of SHN and its competing analysis with α-decay

To analyze the barrier characteristics of α-decay and SF process, Fig. 3.1(a) illustrated the scattering potential for α-decay of ^{270}Bh, and in Fig. 3.1(b) for SF of ^{266}Db, where ^{270}Bh is the preceding α-decaying nucleus with complement daughter as spontaneous fissioning ^{266}Db nucleus, appearing as the end product in the measured [5] decay chain of ^{282}113. Note that both α-decay and SF processes correspond to different mass asymmetry of the decaying fragments, and our choice of ^{135}Te (and its complementary ^{131}I) fragment in Fig. 3.1(b) is based on the (energetically most favored) lowest minima in the fragmentation potential. The relative comparison between α-decay of ^{270}Bh and SF of ^{266}Db suggests that barrier height V_B decreases and barrier position R_b gets enhanced in the α-decay case, thereby decreasing considerably the tunneling probability P (refer to Table 3.1). Note that the "neck-length" parameter (ΔR) values, chosen in reference to the measured $T^{\alpha}_{1/2}$ and $T^{SF}_{1/2}$ data [5], are different for the α and SF processes. Interestingly, the ΔR

parameter is observed to be larger for α-decay, as compared to SF, which seems to suggest that α-decay occurs faster (decay constant λ smaller) than the SF process, as observed in experiments [5–10], compared to the α-decay mode. Thus, the "neck-length parameter ΔR" plays a unique role to examine the decay half-life times and therefore, the decay path of a particular nuclear system.

Next, an attempt is made to analyze systematically the competition between the two decay modes by comparing in Table 3.1, the α-decay half-lifes with those of SF, thereby identifying the prominent decay mode for chosen set of parent nuclei. It is relevant to note that $T_{1/2}$ in DCM depends primarily on the preformation factor P_0 and the penetrability P (refer Eq. (2.45) of chapter 2), the impinging frequency ν_0 is almost constant for different nuclei as shown in Table 3.2. The results presented in Table 3.1 are for all the considered SHN ^{266}Db, ^{267}Rf, ^{267}Db, ^{268}Db, ^{281}Rg, ^{266}Lr and ^{282}Cn, calculated at reported ΔR values, listed in Table 3.2. It is observed from Table 3.1 that both P_0 and P decrease as one goes from SF to α-decaying nucleus, thereby indicating SF channel as the dominant mode of decay. Furthermore, the SF half-life times vary in an extremely wide range from 10^{-4} s to 10^{4} s, and found to be rather small as compared to 10^{17} s to 10^{30} s for the case of α-emission. This means that the studied parents (the end product in the measured [5–10] α-decay chains) are stable against α-decays and hence the considered decay chains terminate via the SF mode, in accordance with the experimental [5–10] observations.

Table 3.2 and Fig. 3.2(a) represent the calculated and experimental SF half-life times ($\log_{10}T^{SF}_{1/2}$) [5–10] corresponding to the most probable decay fragments of each spontaneous fissioning nucleus occuring at the end of an α-decay chain. The preferential decay channel with maximum P_0 is selected from Fig. 3.3 (details discussed in section 3.2.2). The results of other recent calculations by Qian and Ren [16] and Bao *et al.* [17], together with one obtained for a semi-empirical relation [18], are also reported in Table 3.2. The only parameter used in our DCM(ℓ=0) calculations is the neck-length ΔR (=R_a-R_t), which is optimized in view of experimental $T^{SF}_{1/2}$ [5–10]. It is noticed from Table 3.2 that the neck-length parameter (ΔR) is nearly fixed at 0.84±0.05 fm for all considered spontaneous fissioning systems as the end product of α-decay chains. The relevant details of temperature T involved (estimated from the average value of recoil energy E_R), along

Table 3.1: DCM(ℓ=0) estimated P_0, P and $T_{1/2}$ represented for α-decay and SF of various chosen SHN. The identification of the prominent decay mode is also noted.

Decay	Parent	Preformation probability P_0		Penetrability P		Half-life $T_{1/2}$ (s)		Prominent
chain of	nucleus	SF decay	α-emission	SF decay	α-emission	SF decay	α-emission	decay mode
282_{113}	^{266}Db	1.82×10^{-23}	2.08×10^{-35}	1.08×10^{-2}	1.39×10^{-12}	1.32×10^{3}	7.53×10^{24}	SF
287_{114}	^{267}Rf	6.89×10^{-24}	1.03×10^{-39}	5.14×10^{-3}	1.40×10^{-13}	7.46×10^{3}	1.57×10^{30}	SF
287_{115}	^{267}Db	5.93×10^{-24}	2.40×10^{-39}	6.62×10^{-3}	1.13×10^{-13}	6.65×10^{3}	8.24×10^{29}	SF
288_{115}	^{268}Db	3.67×10^{-25}	1.27×10^{-40}	6.78×10^{-3}	2.07×10^{-13}	1.05×10^{4}	8.51×10^{30}	SF
291_{116}	^{267}Rf	8.51×10^{-24}	3.21×10^{-39}	6.17×10^{-3}	3.54×10^{-13}	5.04×10^{3}	1.97×10^{29}	SF
293_{117}	^{281}Rg	5.82×10^{-22}	4.33×10^{-33}	2.08×10^{-2}	9.83×10^{-11}	2.12×10^{1}	4.89×10^{20}	SF
294_{117}	^{266}Lr	1.26×10^{-24}	9.77×10^{-37}	5.45×10^{-3}	7.10×10^{-13}	3.89×10^{4}	3.22×10^{26}	SF
294_{118}	^{282}Cn	6.54×10^{-18}	1.94×10^{-30}	4.58×10^{-2}	4.52×10^{-10}	8.50×10^{-4}	2.33×10^{17}	SF

Table 3.2: Comparison of experimental spontaneous fission half-lives ($T^{SF}_{1/2}$) with our DCM(ℓ=0) calculations and other theoretical results. The characteristics like neck-length parameter (ΔR), temperature (T), total kinetic energy (TKE) and assault frequency $\nu_0(\mathrm{s}^{-1})$ are also listed. The two ^{267}Rf are, respectively, from ^{287}114 and ^{291}116 parent SHN.

Decay	T	R_a=R_t+ΔR	TKE	$\log_{10}T^{SF}_{(1/2)}$(s)					Assault frequency
	(MeV)	(fm)	(MeV)	Expt. [5–10]	DCM(ℓ=0)	Ref. [16]	Ref. [17]	Ref. [18]	$\nu_0(\mathrm{s}^{-1})$
^{266}Db$\rightarrow^{131}$Te+^{135}I	0.353	R_t+0.823	279.3	3.120	3.120	6.782	7.198	-0.313	2.67×10^{21}
^{267}Rf$\rightarrow^{133}$Te+^{134}Te	0.327	R_t+0.788	273.2	3.918	3.873	-	-	-	2.61×10^{21}
^{267}Db$\rightarrow^{132}$Te+^{135}I	0.359	R_t+0.783	278.7	3.811	3.823	8.468	5.207	-1.093	2.65×10^{21}
^{268}Db$\rightarrow^{133}$Te+^{135}I	0.365	R_t+0.791	278.6	4.987	5.021	8.267	7.953	-1.235	2.63×10^{21}
^{267}Rf$\rightarrow^{133}$Te+^{134}Te	0.383	R_t+0.803	273.3	3.670	3.702	-	4.578	-	2.61×10^{21}
^{281}Rg$\rightarrow^{138}$Xe+^{143}La	0.249	R_t+0.865	313.0	1.342	1.327	1.435	-1.903	-2.909	2.70×10^{21}
^{266}Lr$\rightarrow^{133}$Sb+^{133}Te	0.439	R_t+0.818	268.4	4.597	4.589	8.598	-	-1.259	2.59×10^{21}
^{282}Cn$\rightarrow^{140}$Ba+^{142}Ba	0.273	R_t+0.893	318.6	-3.086	-3.070	-	-3.793	-	2.70×10^{21}

with total kinetic energy (TKE) of decay fragments are also given in Table 3.2. Clearly, our DCM(ℓ=0)-calculated half-lives match with the measured data [5–10], which suggests a certainty that DCM imparts a sensible estimate of favorable fission fragments, not available so-far in experiments [5–10]. Also, the experimental verification of calculated total kinetic energies (TKE's) of the fragments would be interesting.

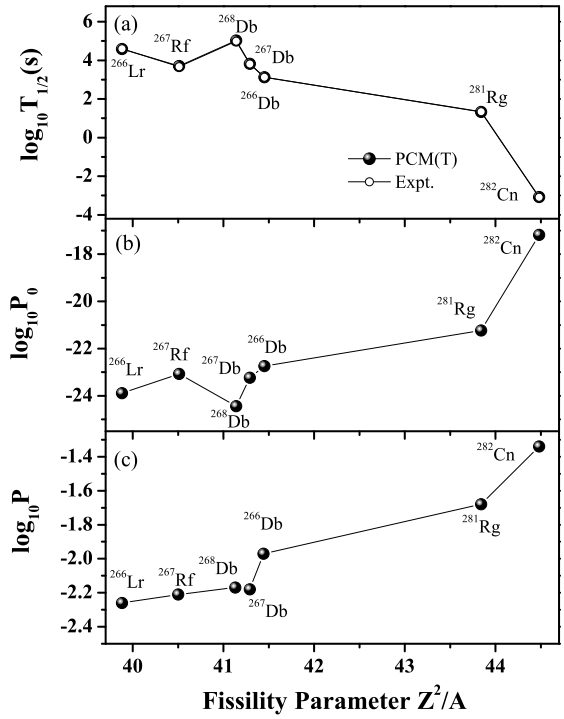

Figure 3.2: a) The DCM(ℓ=0) calculated decay half-lives versus fissility parameter for various spontaneous fissioning SHN are plotted. Panels (b) and (c) depict the same for P_0 and P, respectively.

Next, with increasing Z of the spontaneous fissioning nuclei, the variation of P_0 and P with fissility parameter (Z^2/A) in Fig. 3.2(b) and (c) is also of interest. It is noticed that for the majority of nuclei, both P_0 and P follow similar trend, and hence increase with increasing fissility parameter, thereby indicating highly fissile nature of ^{282}Cn. Moreover, the observed one to one correspondence between $\log_{10}T_{1/2}$ and $\log_{10}P_0$ reveal that the preformation probability P_0 imparts nuclear structure details in SF decay analysis (for a further detailed information, see section 3.2.2 in the following). Figs. 3.2(a) and 3.2(b) depict that when P_0 is small, $T_{1/2}$ is large and vice versa for considered isotopes of Z=103-112 nuclei. A closer look at Fig. 3.2 also indicates a direct isospin (N/Z) dependence of SF half-life times. Amongst the chosen isotopes of Db, for example, $T^{SF}_{1/2}$ is small for the

lighter system and show increment with the increase of neutrons in the parent nucleus. Summarizing, it is observed that more the fissility parameter of a nuclear system, higher the probability of fragments preformation and subsequent penetration, and hence shorter the decay life-time.

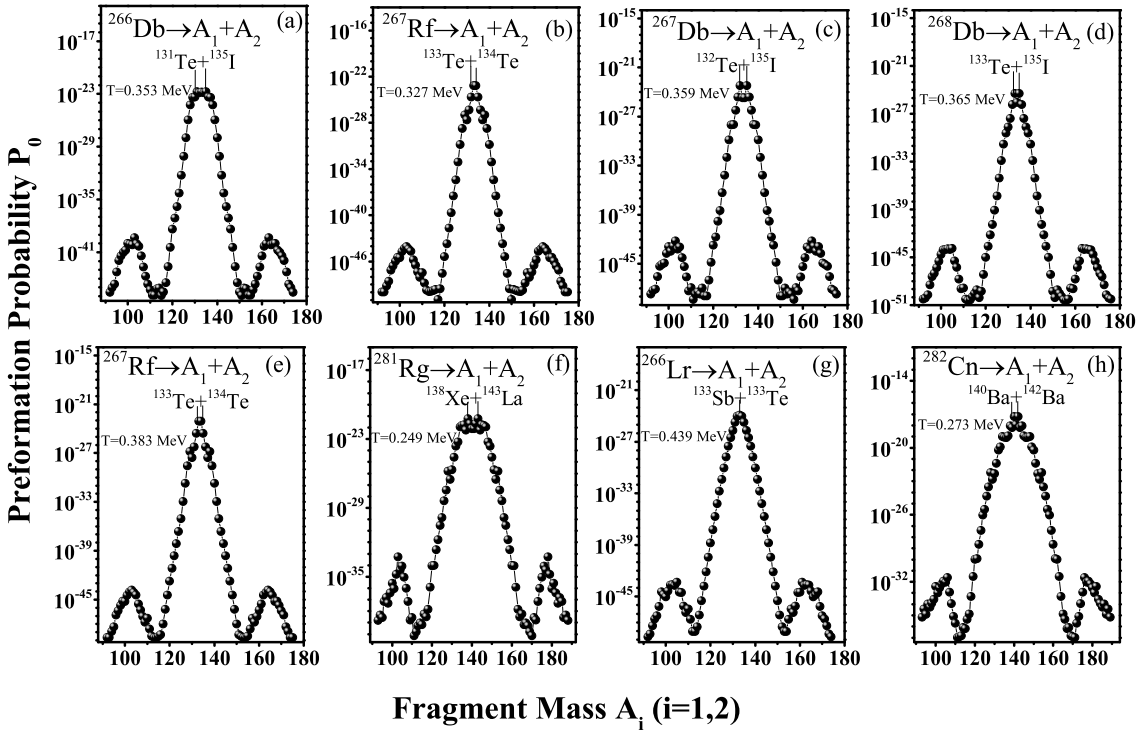

Figure 3.3: Preformation probability P_0 for the fragmentation process of (a)^{266}Db, (b)^{267}Rf, (c) ^{267}Db, (d) ^{268}Db, (e) ^{267}Rf, (f) ^{281}Rg, (g) ^{266}Lr and (h) ^{282}Cn spontaneous fissioing nuclei.

3.2.2 Fragment mass distribution and identification of most probable fragments

One of the objective of this study is to look for the energetically most favorable heavy fragments in the spontaneous decay of various considered nuclei, which belong to the superheavy mass region. Such investigations, in turn, provide a testing ground for the SF half-life calculations. In view of this, Fig. 3.3 depicts P_0 (A_i; i=1,2) for all the chosen nuclei. The best preformed pair of fragments for a particular parent nucleus, are shown in Fig. 3.3 by drawing a vertical line. From figure, three interesting results are noticed: (i) except for the relative magnitude, the mass distributions of all SF nuclei ^{266}Db, ^{267}Rf,

^{267}Db, ^{268}Db, ^{281}Rg, ^{266}Lr and ^{282}Cn are identical, showing clearly the symmetric fission in each case. This result is in an agreement with the only measured data available on mass distribution of ^{262}Rf [20]; (ii) the fission fragments with mass range A_2=131 to 140 (and complementary fragments) appear as the prime contributors towards SF half-lives in all chosen nuclei; (iii) the shell closure effects around Z=50 and N=82 are seen in operation and seem to affect the preformation factor significantly.

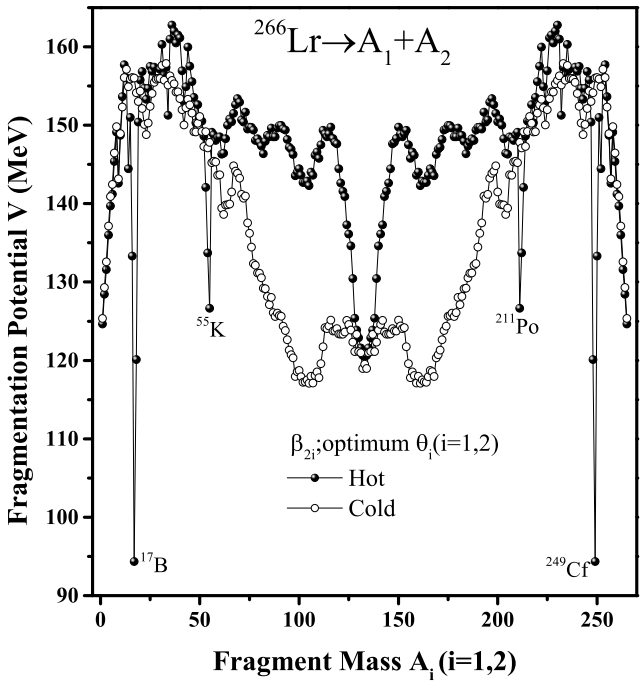

Figure 3.4: The fragmentation potential $V(\eta)$ for the SF decay of ^{266}Lr for quadrupole β_{2i} deformed choice of fragments with 'optimum' orientations $\theta_i^{opt.}$ forming 'hot compact' and 'cold elongated' configurations at fixed value of ΔR=0.818 fm.

To investigate the relative behaviour of 'hot compact' and 'cold elongated' configurations, Fig. 3.4 illustrates the fragmentation potential V(A_i) ($\equiv$ V(η)) for ^{266}Lr nucleus. All the calculations have been made for quadrupole (β_{2i}) deformed fragments having 'optimum' orientations $\theta_i^{opt.}$, taken from Table 1 of [19]. The orientations are determined based on the sign of β_{2i} (+ or -), which further characterizes the 'hot compact' or 'cold elongated' configuration. The 'hot compact' configuration refers to the smallest interaction radius and highest interaction barrier, whereas the 'cold elongated' configuration corresponds to the largest interaction radius and lowest interaction barrier. Fig. 3.4 represents that the

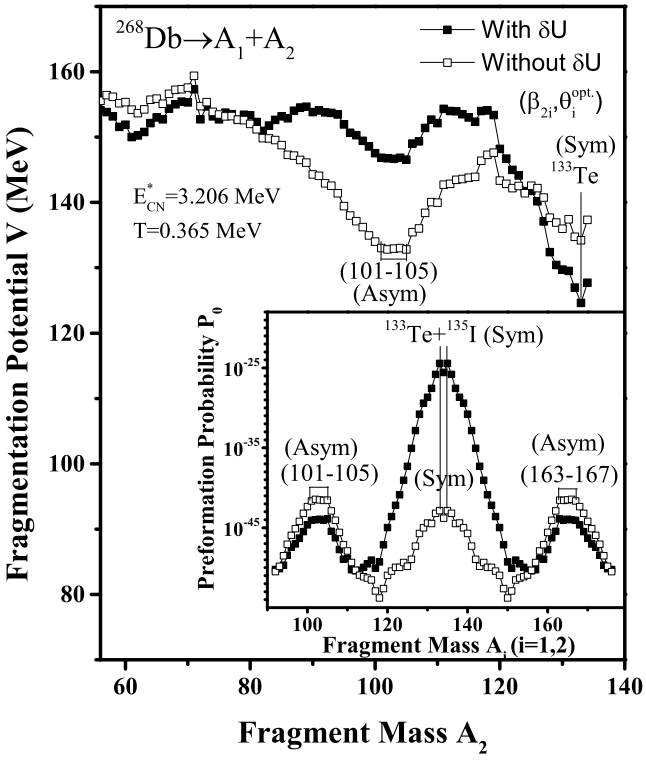

Figure 3.5: The calculated fragmentation potential for spontaneous fission of ^{268}Db are plotted to illustrate the significance of shell corrections. The inset shows the same but for preformation factor $P_0(\mathrm{A}_i)$.

mass distribution is clearly symmetric for 'hot' configuration, and becomes asymmetric for 'cold' configurations. In the present work, only 'hot compact' configurations are used for the calculations. The sharp minima in fragmentation potential at ^{17}B, ^{55}K (and in complementary heavy fragments) results in an enhanced preformation probability. However, the corresponding penetrability P is very small for each of these fragments, such that product P_0P is smaller than for the symmetric fragmentation, and hence the dips which arise due to inaccurate estimates of β_2-deformation don't affect our conclusions. After the study of orientations effects in SF decay, the influence of 'shell corrections' on SF dynamics is explored in the next section.

3.2.3 Influence of "shell corrections" on SF decay

The role of "shell corrections δU" comes explicitly through binding energy term in the fragmentation potential. In the present discussion, possible role of δU for the SF decay of

^{268}Db nucleus is analyzed. Two approaches have been considered: first is dependence of V(A_2) on shell corrections (i.e. δU$\neq$0), second is it's comparison with 'δU=0' case, see Fig. 3.5. The fragmentation potential minima are of interest here, because the corresponding preformation factor P_0 becomes the largest, compared to its neighbours. This is depicted in the inset of Fig. 3.5. Apparently for both the cases, a strong minima around doubly magic Z_2=50 and N_2=80 (^{133}Te) is observed, and hence the corresponding maxima in preformation profile, labelled as 'Sym'. However the prominence of the same remains intact only when the shell corrections 'δU' are included in the binding energy term. In other words, a closer look at the potential energy minima for δU=0 case indicates some contribution of asymmetric fission fragments as well, specifically in the mass region of A_2=101-105, denoted as 'Asym'. The preformation factor in the inset also depicts the similar result of a favoured symmetric to favoured asymmetric fragmentation as one switch from δU$\neq$0 to δU=0 configurations. That is, with the inclusion of shell corrections our DCM analysis clearly depicts pure symmetric behaviour in preformation profile which changes to triple humped mass distribution for the case of δU=0 case. These observations suggest that the shell corrections play a significant role and hence are necessary to make concrete predictions of the SF decay.

3.3 Conclusions

In this chapter, the SF decay of various isotopes of Z=103-112 nuclei appearing as the end product in α-decay chains of ^{282}113, ^{287}114, ^{287}115, ^{288}115, ^{291}116, ^{293}117, ^{294}117 and ^{294}118 nuclei is studied. The DCM (ℓ=0) gives a good description of SF half-lives of the chosen nuclei, for the static choice of β_2-deformations. The importance of 'hot compact' and 'cold elongated' configurations is examined, supporting the result of 'hot compact' configurations. The competitive behaviour of α-decay and SF processes have been analyzed, which could give significant information with respect to the dynamics involved in superheavy mass region. The potential energy surfaces are shown to display the effects of closed shell effects at Z=50, N=82 for the most probable fission fragments in the symmetric fission window. For the choice of δU$\neq$0, a clear preference for the symmetric fission fragment is seen in an agreement with experimental observations for heavy and superheavy nuclei, which otherwise changes to triple humped structure for

δU=0 case.

After studying the SF in the superheavy mass region, the study is extended to the light particle and heavy ion induced fission of actinide nuclei in chapter 4. It will be of further interest to understand the fission dynamics of compound nuclei formed via variety of nuclear reactions.

Bibliography

[1] G. N. Flerov and K. A. Petrzhak, Phys. Rev. **58**, 275 (1940).

[2] Yu. Ts. Oganessian and V. K. Utyonkov, Nucl. Phys. A **944**, 62 (2015); and references therein.

[3] S. Hofmann, Radiochim. Acta **99**, 405 (2011).

[4] Niyti, G. Sawhney, M. K. Sharma and R. K. Gupta, Phys. Rev. C **91**, 054606 (2015).

[5] Yu. Ts. Oganessian *et al.*, Phys. Rev. C **87**, 014302 (2013).

[6] Yu. Ts. Oganessian *et al.*, Phys. Rev. C **87**, 054621 (2013) .

[7] J. Khuyagbaatar *et al.*, Phys. Rev. Lett. **112**, 172501 (2014).

[8] Yu. Ts. Oganessian *et al.*, Phys. Rev. C **70**, 064609 (2004).

[9] Yu. Ts. Oganessian *et al.*, Phys. Rev. C **74**, 044602 (2006).

[10] Yu. Ts. Oganessian *et al.*, Phys. Rev. Lett. **109**, 162501 (2012).

[11] S. Hofmann *et al.*, Eur. Phys. J. A **52**, 180 (2016).

[12] N. Wang *et al.*, Phys. Rev. C **85**, 041601(R) (2012).

[13] G. Sawhney, A. Kaur, M. K. Sharma and R. K. Gupta, Acta Phys. Pol. B **48**, 629 (2017).

[14] A. Kaur, G. Sawhney, M. K. Sharma and R. K. Gupta, Proceedings of the DAE Symp. on Nucl. Phys. **62**, 514 (2017).

[15] A. Kaur, G. Sawhney, M. K. Sharma and R. K. Gupta, Int. J. Mod. Phys. E **27**, 1850043 (2018).

[16] Y. Qian and Z. Ren, Phys. Rev. C **90**, 064308 (2014).

[17] X. J. Bao, S. Q. Guo, H. F. Zhang, Y. Z. Xing, J. M. Dong and J. Q. Li, J. Phys. G: Nucl. Part. Phys. **42**, 085101 (2015).

[18] K. P. Santhosh and B. Priyanka, Nucl. Phys. A **940**, 21 (2015).

[19] R. K. Gupta, M. Balasubramaniam, R. Kumar, N. Singh, M. Manhas and W. Greiner, J. Phys. G: Nucl. Part. Phys. **31**, 631 (2005).

[20] M. R. Lane, K. E. Gregorich, D. M. Lee, M. F. Mohar, M. Hsu, C. D. Kacher, B. Kadkhodayan, M. P. Neu, N. J. Stoyer, E. R. Sylwester, J. C. Yang and D. C. Hoffman, Phys. Rev. C **53**, 2893 (1996).

Chapter 4

Light particle and heavy ion induced fission of actinide nuclei

Earlier chapter demonstrates the dynamical features of spontaneous fission (SF) in the superheavy mass region. The obtained results were quite interesting in terms of barrier characteristics, fission fragment mass distributions and identification of most probable decay fragments. Moreover, the role of deformations, orientations and shell effects was duly addressed for the SF decay of superheavy nuclei. By acquiring the confidence from the study of SF, now the present chapter will focus on the analysis of light particle and heavy ion induced fission of actinide nuclei. The angular momentum (ℓ) effects were salient in the previous chapter, as study was concerned with the process of spontaneous emission. Here, in the present chapter angular momentum effects are duly incorporated along with the deformation and orientation degree of freedom. This chapter is partitioned into two major sections, where first section (4.2) contains the study of light particle (n and p) induced fission of actinide nuclei. While, the second section (4.3) deals with the decay of ^{216}Th* actinide nucleus formed via heavy ion induced reaction (^{32}S+^{184}W). The results of these studies are published in Refs. [1–4]. A general description of considered light particle and heavy ion induced reactions is discussed in following section.

4.1 Introduction

The light particle induced fission is a subject of great interest, since the discovery of n-induced fission of Uranium. This is attributed to the fact that n-induced fission reactions provide a deep insight into the reaction dynamics and help in attaining a comprehensive picture of the formation and decay aspects of nuclear systems. Amongst several

n-induced reactions, the ones involving actinide target nuclei have gained special attention due to their wide applicability. This is so the actinide nuclei produced in nuclear reactors steer us towards the generation of nuclear power and are a boon for accelerator driven systems (ADS) [5]. Several studies were done to comprehend the fission characteristics and their dependence on incident energy, temperature, angular momentum and deformation etc. However, no consistent description has been attained as yet to address these quantities which inturn help in studying various competing channels involved in decay process of nuclear systems. The present chapter aims to examine the fission decay of actinide nuclei formed in n+^{232}Th and n+^{238}U nuclear reactions at incident energies varying from E_n=32.8 MeV to 59.9 MeV. It has been observed that the relative study of reactions involving neutron beam incident on diverse target nuclei aids in understanding the behavior of different actinide nuclei formed under similar reaction conditions. This work is extended further for two more actinide nuclei produced in n-induced reactions, i.e., ^{233}Pa* and ^{239}Np* at common incident energy E_n=32.8 MeV. Moreover, a comparative analysis of the reactions involving neutral (neutron) as well as charged particle (proton) projectile beam is also carried out at relatively lower incident energy E∼27 MeV, where experimental data is available. Both the n- and p-induced reactions and their subsequent fission cross-sections form an interesting prospect of research at higher incident energy as such studies may impart significant inputs in the sub-critical aspect of the ADS reactors. The related results and discussions are presented in section 4.2.

Apart from the light particle induced fission, the decay dynamics involving heavy ion induced reaction is also explored in this chapter. The heavy ion induced reactions play a significant role in the extension of periodic table, synthesis of new elements, and production of isotopes beyond β-stability line. When, we replace the light particle with heavier projectile, one would expect some change in the dynamics involved. Beside this, the entrance channel characteristics such as mass asymmetry, Coulomb repulsion, projectile energy, deformations, orientations etc., strongly influence the reaction dynamics. The literature reveals that, the nuclear reactions having small mass asymmetry and large Coulomb repulsion, are more prone to non-compound nucleus (nCN) processes. Which means that, the probability of nCN process in light particle induced reactions is negligible due to large mass asymmetry and small Coulomb repulsion factor. Here, an effort is

made in section 4.3, to explore the distinct contribution of competing CN and nCN decay channels in the dynamics of ^{32}S+^{184}W$\rightarrow$^{216}Th* reaction. For this reaction, the entrance channel mass asymmetry α_e is 0.703, which is smaller than the "Businaro-Gallone mass asymmetry" [6] i.e. α_{BG}=0.864. Hence, according to Ref. [7, 8], the nCN fission may be present in the decay of ^{216}Th* nucleus. Moreover, nCN component is expected to compete with CN process at $Z_PZ_T \geq 1000$ [9], due to the large entrance channel Coulomb repulsion. The product of Z_PZ_T for the considered reaction is 1184, hence exist a possibility of hindrance in the CN formation. In view of this, DCM approach is utilized to explore the relevant contribution of decay processes for CN [Evaporation residue (ER) and fusion-fission (ff)] and nCN [quasi fission (QF) and fast fission (FF)] processes for ^{32}S+^{184}W reaction, in reference to the experimental findings of Zhang *et al.*, [10]. Interestingly, the experimental data [10] is available across the Coulomb barrier for this reaction, which provide us opportunity to investigate the decay dynamics involved via CN and nCN channels across the Coulomb barrier. Finally, the results are concluded in section 4.4.

4.2 *n* and *p* induced fission of actinide nuclei

This section divided into three sub-sections, and reveals interesting aspects associated with the dynamics of n- and p-induced reactions and related structure effects. First of all, section 4.2.1 represents the calculated fission excitation functions of n+^{232}Th$\rightarrow$^{233}Th* and n+^{238}U$\rightarrow$^{239}U* reactions using DCM [11–15] at incident energies E_n=32.8 MeV-59.9 MeV, and compared with the experimental findings of Ryzhov *et al.* [16]. To examine the effect of deformations, the calculations are carried out using spherical choice of fragmentation as well as after the incorporation of quadrupole (β_2) deformation for optimum orientations θ_i^{opt} criteria [17]. Apart from ^{233}Th* and ^{239}U* nuclei, the n-induced reactions have been studied for two other nuclei i.e. ^{233}Pa* and ^{239}Np* under similar reaction conditions. Beside this, section 4.2.2 represents the impact of moment of inertia on the n-induced fission of ^{233}Th* nucleus for the choice of sticking (I_S) and non-sticking (I_{NS}) moment of inertia. A comparative analysis of n- and p-induced fission of actinide nuclei is made in section 4.2.3. Note that the fission cross-sections for nuclear systems formed in n-induced reactions are obtained using partial wave analysis by employing angular

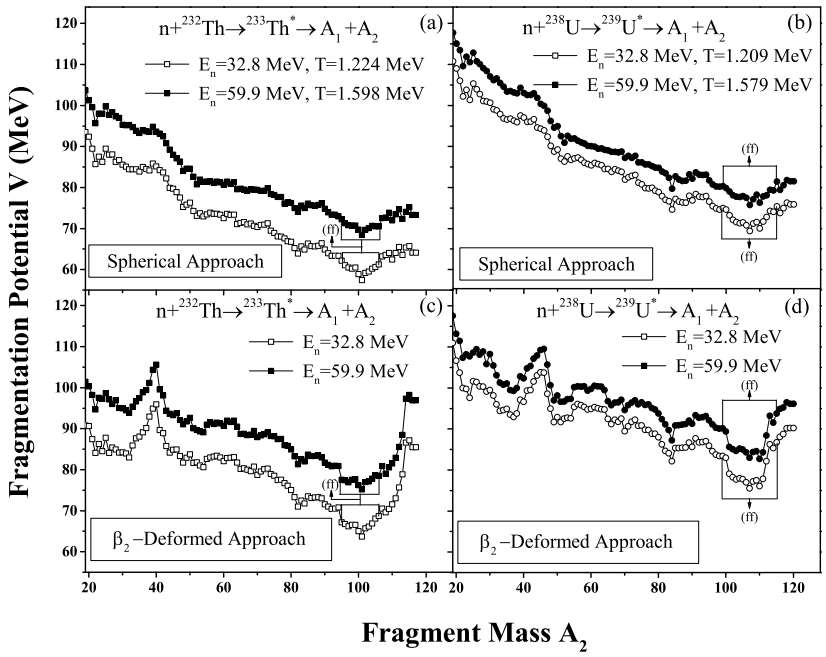

Figure 4.1: Fragmentation potential $V(A_2)$ at extreme E_n values plotted for the decay of $^{233}Th^*$ and $^{239}U^*$ nuclei for (a,b) spherical approach and (c,d) β_2-deformed choice of fragmentation.

momentum in the range ℓ=0$\hbar$ to ℓ=ℓ_{max}. Owing to different characteristics at extreme ℓ-values, the fragmentation potential, preformation probability and other observable of DCM are elaborated at ℓ_{max} values, as such higher ℓ-values are relevant for addressal of fission dynamics.

4.2.1 n-induced fission of actinide nuclei

Fig. 4.1 illustrates the fragmentation potential for fissioning $^{233}Th^*$ and $^{239}U^*$ nuclei at extreme E_n, i.e., 32.8 MeV and 59.9 MeV. Figs. 4.1(a) and (b) show the behavior of actinide nuclei for spherical approach while Figs. 4.1(c) and (d) depict the fragmentation potential for β_2-deformed choice of fragments. One may observe that at particular incident energy, for both spherical and deformed choices, the fragmentation potential decreases with increase in mass (A_2) and attains minimum value for a certain range of fragment mass (marked in the figure as fission fragments (ff)) which is different for $^{233}Th^*$ and $^{239}U^*$ nuclei. In general, the fragments with lower fragmentation potential possess higher preformation probability (as evident from Fig. 4.2 ahead) and hence lead to the most favourable products contributing in the fission decay mode. Besides this, the variation

of potential energy surface reveals that for either of the actinide nuclei under study, the fragmentation potential is asymmetric for spherical as well as deformed approach through being relatively less asymmetric for spherical choice as compared to the deformed approach. Panel (a) and (b) suggest that although the structure of fragmentation potential is independent of incident energy, its magnitude increases on going from E_n=32.8 MeV to 59.9 MeV. The difference in magnitude of fragmentation potential at extreme energies is more for ^{233}Th* nucleus and relatively less for ^{239}U* nucleus. This observation also remains consistent for the fragmentation potential obtained using quadrupole (β_2) deformation approach, shown in Figs. 4.1(c) and (d). Interestingly, the results obtained in the present study for ^{233}Th* and ^{239}U* nuclei are compared with those obtained from an earlier work of ^{240}Np* nucleus formed in n-induced reactions at relatively much lower energies (E_n∼0-20 MeV) [14]. From the comparative study of results obtained for these actinide nuclei it may be said that for spherical approach, the observations drawn for higher energies i.e. E_n=32.8-59.9 MeV accord with that obtained at lower energy i.e. E_n∼0-20 MeV. However, with the inclusion of deformations the behavior at higher energy (E_n=32.8 MeV and 59.9 MeV) is different from that at lower energy (E_n=0 MeV and 20 MeV), as for the latter case the structure of fragmentation potential changes as one goes from minimum to maximum energy. This suggests that the impact of deformations is more evident at lower energies when compared with heavier one. In other words it may be said that, for n-induced reaction the incident energy plays a crucial role so far as the inclusion of deformation is concerned. Apparently, the potential energy surfaces are modified, with the incorporation of deformations, the effect being more perceptible for the heavy mass fragments (A_2=32-44). However, in present study the effect of deformations is not significant for the contributing fission region under study. In reference to this observation, further study for the fission dynamics of actinide nuclei has been carried out with the use spherical approach only.

After analyzing the variation of fragmentation structure, the dynamics of n-induced reactions is investigated through the behavior of preformation probability $P_0(A_i)$. In DCM, P_0 helps in analyzing the mass distribution of a given nucleus and is obtained by solving Schrödinger equation using the fragmentation potential. Figs. 4.2(a) and (b) show the preformation probability at minimum E_n=32.8 MeV while Figs. 4.2(c) and (d)

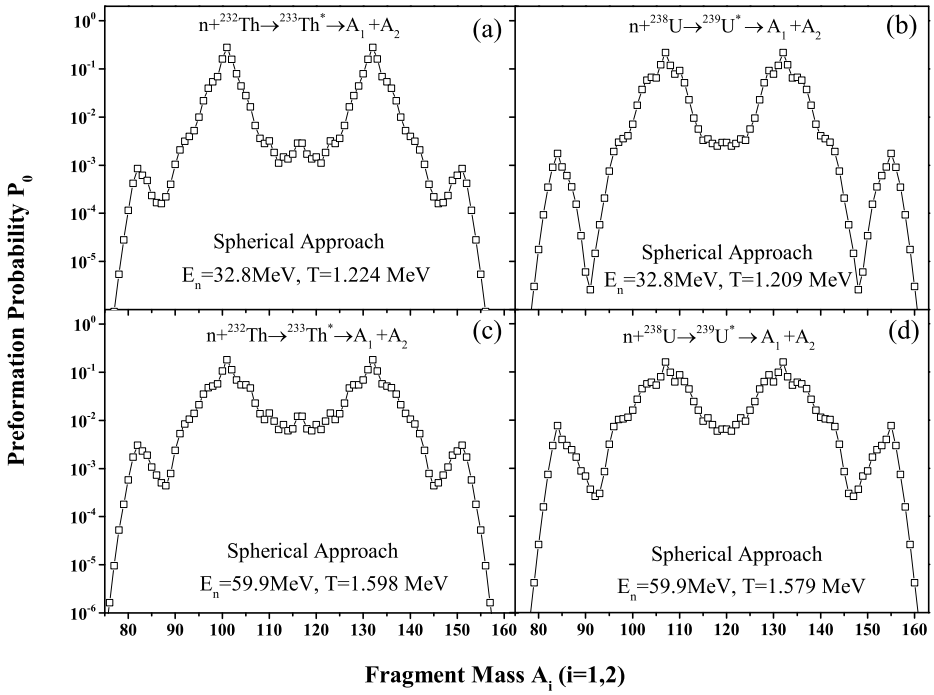

Figure 4.2: Fragment preformation probability $P_0(\mathrm{A}_i;\ i{=}1{,}2)$ for the $n{+}^{232}\mathrm{Th}{\rightarrow}^{233}\mathrm{Th}^*$ and $n{+}^{238}\mathrm{U}{\rightarrow}^{239}\mathrm{U}^*$ reactions at (a,b) minimum energy, E_n=32.8 MeV and (c,d) maximum energy, E_n=59.9 MeV for the spherical choice of fragmentation.

depict the behavior at maximum energy, E_n=59.9 MeV for either of the actinide nuclei for spherical approach. As observed earlier from Fig. 4.1, the fragment mass distribution for $^{233}\mathrm{Th}^*$ as well as $^{239}\mathrm{U}^*$ nuclei is asymmetric. A deeper look of Fig. 4.2(a) and (b) reveals that for $^{233}\mathrm{Th}^*$ nucleus, although the fragment mass distribution is asymmetric yet a small hump appears around A/2 region, representing the emergence of some symmetric fission fragments which does not appear in the preformation profile of $^{239}\mathrm{U}^*$ nucleus. This behavior of mass distribution at $\ell{=}\ell_{max}$ remains consistent for minimum as well as maximum energy. Interestingly, this observation through DCM based analysis is in reasonable agreement with experimental [16] outcomes which report that the symmetric fission is relatively more for $^{233}\mathrm{Th}^*$ nucleus as compared to $^{239}\mathrm{U}^*$ nucleus. The global asymmetric fragment distribution and a diminutive difference around symmetric fission region could aid in exploring the nuclear-structure effects related to actinide nuclei. Although small, yet emergence of symmetric peak along with dominant asymmetric distribution suggests a probability of sub-structure effects in the decay of $^{233}\mathrm{Th}^*$. Apart from producing the fragment mass distribution and indicating the probability of various mass regions, DCM

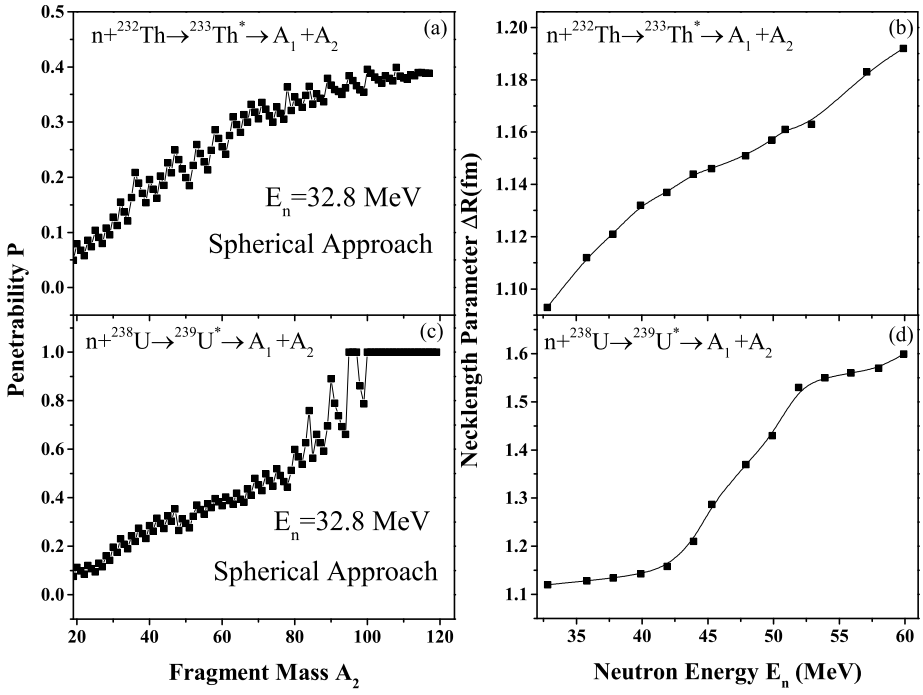

Figure 4.3: (a) The penetrability $P(\mathrm{A}_2)$ plotted at minimum energy and (b) best-fitted ΔR as a function of E_n, for the fissioning ^{233}Th* nucleus using spherical fragmentation. Panel (c) and (d) represent the same but for ^{239}U* nucleus.

also has the ability of identifying the dominant fission fragments, which contributes in the fission excitation functions of a chosen reaction. The fragments in the range A_2=95-106 (and complementary fragments) have major contribution towards fission excitation functions of n+^{232}Th$\rightarrow^{233}$Th* reaction, whereas fragments A_2=99-115 (along with complimentary fragment) contribute for n+^{238}U$\rightarrow^{239}$U* reaction. It may be noted that, the contributing fission fragments for either of the nuclei remain consistent at all the chosen energies. Thus, it may be said that for the n-induced reactions, the choice of contributing fission fragments depends mainly on the mass of CN and the fragmentation structure is independent of the energy range involved.

The cross-sections in DCM depend upon the P_0, and P which are estimated using the WKB method. Thus after analyzing the variation of P_0, the behavior of penetrability P of fission fragments for the actinide nuclei is explored. Fig. 4.3(a) and (c) represent the $P(\mathrm{A}_2)$ plotted for ^{233}Th* and ^{239}U* nuclei at minimum energy and maximum angular momentum. Simultaneously, in Fig. 4.3(b) and (d), the best fit values of "neck-length parameter (ΔR)", optimized to calculate fission excitation functions for the same actinide nuclei are studied as a function of incident E_n varying from 32.8 MeV-59.9 MeV. From the

Table 4.1: The DCM-obtained excitation functions for the fission decay of ^{233}Th* and ^{239}U* nuclei produced in n-induced reactions at respective ΔR values. The cross-sections have been shown for the spherical approach at all the incident energies and compared with the fission data [16].

^{232}Th(n,f)					^{238}U(n,f)				
E_n	Temperature	$\triangle$R	$\sigma_{Fission}^{DCM}$	$\sigma_{Fission}^{Expt.}$	E_n	Temperature	$\triangle$R	$\sigma_{Fission}^{DCM}$	$\sigma_{Fission}^{Expt.}$
(MeV)	(MeV)	(fm)	(b)	(b)	(MeV)	(MeV)	(fm)	(b)	(b)
32.8	1.224	1.093	0.818	0.814	32.8	1.209	1.120	1.712	$1.718^{+0.04}_{-0.04}$
35.8	1.271	1.112	0.832	0.831	35.8	1.257	1.128	1.688	$1.685^{+0.04}_{-0.04}$
37.8	1.301	1.121	0.852	0.857	37.8	1.286	1.134	1.674	$1.669^{+0.04}_{-0.04}$
39.9	1.332	1.132	0.896	0.889	39.9	1.316	1.143	1.710	$1.708^{+0.05}_{-0.04}$
41.9	1.362	1.137	0.888	0.893	41.9	1.345	1.158	1.694	$1.695^{+0.04}_{-0.04}$
43.9	1.390	1.144	0.916	0.886	43.9	1.373	1.210	1.682	$1.682^{+0.03}_{-0.05}$
45.3	1.410	1.146	0.884	0.893	45.3	1.392	1.287	1.680	$1.692^{+0.04}_{-0.04}$
47.9	1.445	1.151	0.886	0.909	47.9	1.427	1.370	1.668	$1.678^{+0.04}_{-0.05}$
49.9	1.472	1.157	0.906	0.919	49.9	1.454	1.430	1.636	$1.643^{+0.04}_{-0.05}$
50.9	1.486	1.161	0.922	0.929	51.9	1.480	1.530	1.672	$1.678^{+0.08}_{-0.01}$
52.9	1.511	1.163	0.916	0.923	53.9	1.505	1.550	1.552	$1.636^{+0.05}_{-0.04}$
57.1	1.564	1.183	0.934	0.936	55.9	1.530	1.560	1.520	$1.655^{+0.05}_{-0.05}$
59.9	1.598	1.195	0.860	0.949	58.0	1.556	1.570	1.410	$1.655^{+0.04}_{-0.04}$
					59.9	1.579	1.599	1.408	$1.613^{+0.04}_{-0.04}$

variation of penetrability, it is found that with increase in fragment mass, the penetrability increases and attains a maximum value, as it approaches the fission region. Comparing its variation with Fig. 4.1(a) (open circles), it is observed that the behavior of penetrability is opposite to that of fragmentation potential. In other words, the fragments having minimum fragmentation potential have higher preformation probability and hence the maximum penetrability through the decay barrier. This further confirms that fragments in the range A_2=95-106 and A_2=99-115 have the highest probability to penetrate the fission barrier and thus contribute towards the fission decay of ^{233}Th* and ^{239}U* nuclei formed in n-induced reactions. After analyzing the fragment mass distribution and identifying the favorable fission decay fragments for both the actinide nuclei, the variation of best fit values of the neck-length parameter is examined in Fig. 4.3(b) and (d). It is evident that, ΔR follows the trend observed for penetration probability and shows increment with increase in E_n being relatively large at the highest energy as compared to lowest incident energy. By employing these values of ΔR, we could address the experimental data [16] at all energies in contrast to the theoretical MCFx calculations (plotted in Fig. 8 of Ref [16]).

Table 4.1 presents the DCM estimated fission contributions for ^{233}Th* and ^{239}U* nuclei together with the available experimental results [16] and the fitted ΔR-values. These fission cross-sections are calculated using partial wave analysis by employing angular momentum in the range ℓ=0$\hbar$ to ℓ=ℓ_{max}. By comparing the ΔR's of ^{233}Th* and ^{239}U* nuclei tabulated in Table 4.1, it may be observed that ^{233}Th* accounts lesser magnitude of ΔR in comparison with ^{239}U*. In DCM, the ΔR parameter is used to predict the time scale of fragment emission, thus suggesting that at comparable incident energy, the decay of ^{239}U* nucleus is more prompt than that of ^{233}Th* nucleus.

In addition to the above study, another observable of DCM is the index of barrier lowering, ΔV_B (=V(R_a)-V_B). The DCM has in-built property of barrier lowering which is incorporated via the ΔR [18]. Fig. 4.4 represents the barrier modification ΔV_B plotted for contributing fission fragments for ^{233}Th* and ^{239}U* nuclei at a common angular momentum, i.e. the maximum ℓ-value for ^{233}Th* nucleus. Although, the emitted fragments for both nuclei are different, it is observed that ΔV_B for ^{233}Th* as well as ^{239}U* nuclei follow a similar trend and is relatively lower (in magnitude) for ^{239}U* nucleus. It may

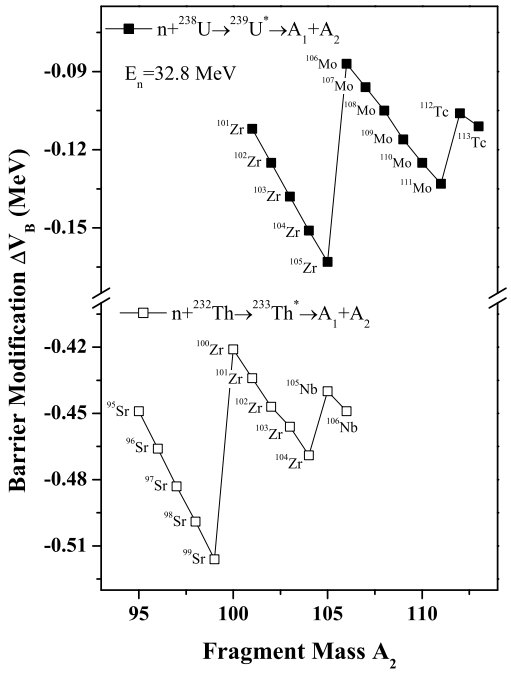

Figure 4.4: The index of barrier lowering $\Delta V_B(\mathrm{A}_2)$ plotted for ^{233}Th* (open squares) and ^{239}U* nuclei (filled squares) produced in n-induced reactions at minimum E_n=32.8 MeV

be noted that the ΔV_B parameter depends upon the actually used barrier and peak of the barrier. The steps shown in figure may be associated with the difference in the decay barrier heights (V_B) of the decaying fission fragments as one moves from Sr to Nb and Zr to Tc for ^{233}Th* and ^{239}U* compound nuclei respectively. For the isotopes of a emerging decay fragment (A_2), $\Delta \mathrm{V}_B$ is minimum in magnitude for lighter mass fragment and increases with increase in addition of neutrons. However, for higher charge fragment relatively lesser barrier modification is needed, which is due to different Coulomb components for these fragments.

So far, the relative study of ^{233}Th* and ^{239}U* nuclei are analyzed by investigating the effect of incident energy, role of deformations and prediction of fission excitation functions at certain energies. To have further insight of n-induced fission, a comparative investigation of two more nuclei, i.e. ^{233}Pa* and ^{239}Np* have been carried out. It is assumed that ^{233}Pa* and ^{239}Np* nuclei are formed under similar reaction conditions as that of ^{233}Th* and ^{239}U* nuclei. Interestingly, all the four nuclei possess similar isospin (N/Z ratio) of $\sim$1.5 whereas, their most probable fission fragment is different being A_2=101, 100, 107

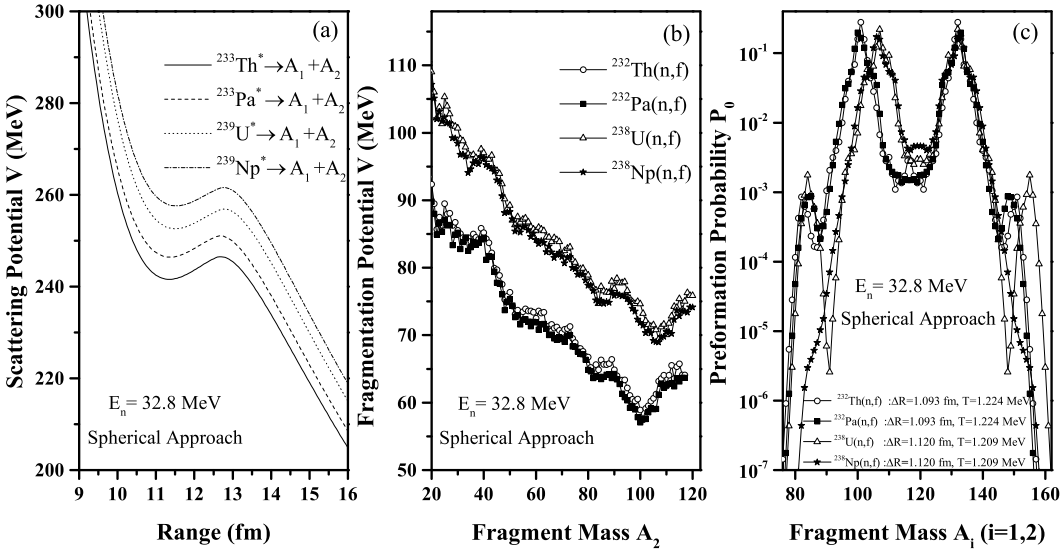

Figure 4.5: (a) Scattering potential V(MeV) for ^{233}Th*, ^{233}Pa*, ^{239}U* and ^{239}Np* nuclei generated in n-induced reactions at E_n=32.8 MeV, plotted for the most probable decay channel and corresponding maximum angular momentum values. Panel (b) and (c) depict the fragmentation potential and preformation probability respectively for given nuclei at incident energy E$_n$=32.8 MeV and ℓ=ℓ_{max} by considering spherical approach.

and 106 for ^{233}Th*, ^{233}Pa*, ^{239}U* and ^{239}Np* nuclei respectively. Apparently, for the reactions exhibiting fission decay mode, the fission fragments as well as decay barriers are of great interest. In framework of DCM, owing to the most probable fission fragments the scattering potential is plotted in Fig. 4.5(a) for all four nuclei at common incident energy, E_n=32.8 MeV and respective angular momentum, i.e. ℓ_{max}=145$\hbar$ for ^{233}Th*, ^{233}Pa* and ℓ_{max}=151$\hbar$ for ^{239}U*, ^{239}Np* nuclei. From the figure it is observed that, both barrier position and barrier height are different for all actinides thereby resulting in different tunneling probability for each of them. The barrier height is minimum for ^{233}Th* and increases on going from ^{233}Pa* to ^{239}U* to ^{239}Np* nucleus. A similar trend for the scattering potential is obtained at a common angular momentum also. Thus, it may be said that independent of the chosen angular momentum, the barrier modification needed for a given actinide nucleus decreases with increment in charge number. This result is consistent with that attained earlier in Fig. 4.4. The relative behavior of these four actinide nuclei is further studied by analyzing the fragmentation potential and preformation probability. Figs. 4.5(b,c) depict the potential energy surface and mass distribution for the decay of ^{233}Th*, ^{233}Pa* and ^{239}U*, ^{239}Np* nuclei at incident energy E_n=32.8 MeV. It

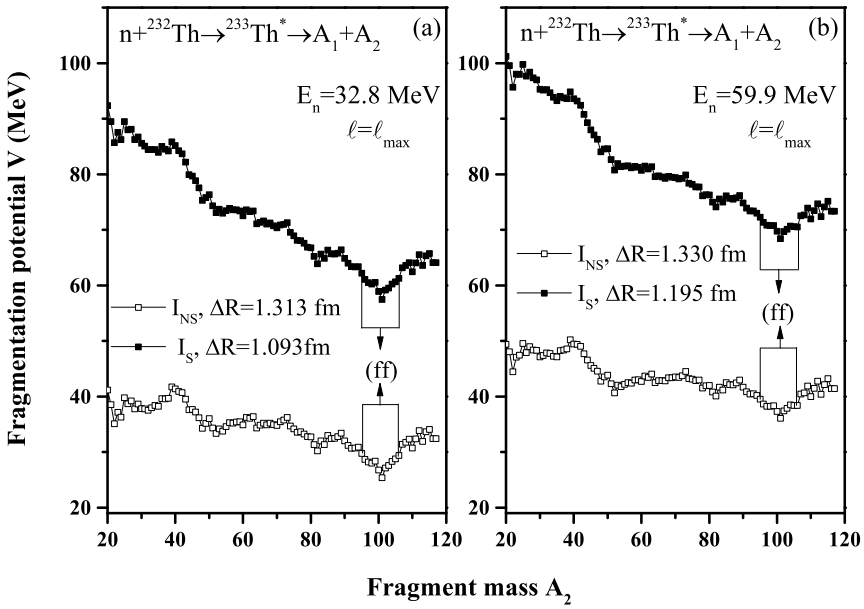

Figure 4.6: Fragmentation potential V(A_2) shown at (a) E_n=32.8 MeV and (b) E_n=59.9 MeV, for ^{233}Th* produced in n-induced reaction using I_S and I_{NS} case.

may be noted that except for some minor variation observed for lighter nucleus ^{233}Th*, the behaviour of fragmentation potential and hence preformation probability for all nuclei is almost identical. This observation is independent of the angular momentum chosen, thus revealing that the variation of mass distribution follows a systematic trend.

Table 4.2: The DCM obtained fission excitation functions for ^{233}Th* nucleus at various E_n for the choice of I_{NS} moment of inertia and compared with the measured fission data [16]. ΔR values are also listed, where ℓ_{max}=39$\hbar$.

E_n (MeV)	Temperature (T) (MeV)	ΔR (fm)	$\sigma_{Fission}^{DCM}$ (b)	$\sigma_{Fission}^{Expt.}$ (b)
32.8	1.224	1.313	0.448	0.814
39.9	1.332	1.317	0.328	0.889
45.3	1.410	1.319	0.258	0.893
52.9	1.511	1.326	0.224	0.923
59.9	1.598	1.330	0.168	0.949

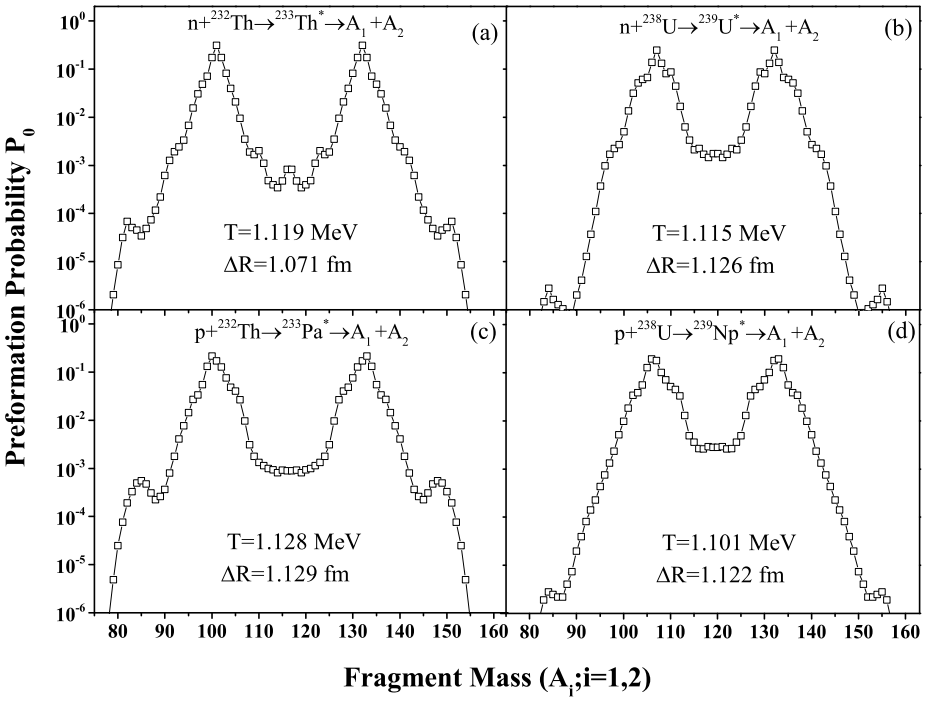

Figure 4.7: Preformation probability $P_0(\mathrm{A}_i)$ shown at E∼27 MeV, for the decay of (a,b) ^{233}Th* and ^{239}U* nuclei formed in n-induced reactions (c,d) ^{233}Pa* and ^{239}Np* nuclei formed in p-induced reactions.

4.2.2 Impact of I_S and I_{NS} moment of inertia on n-induced fission

Further, to see the impact of sticking (I_S) and non-sticking (I_{NS}) choices of moment of inertia on the decay of ^{233}Th* nucleus, the behaviour of fragmentation potential is analyzed at E_n=32.8 MeV and 59.9 MeV, as illustrated in Fig. 4.6. The impact of moment of inertia enters the fragmentation potential via the rotational energy term. The structure of potential energy surfaces in the heavy mass region does not change much, whereas the magnitude of potential is higher for the sticking limit as compared to I_{NS} choice. Moreover, the most probable fission fragments remain same (i.e., A_2=95-106) for both the cases. Although by replacing the I_S limit with I_{NS}, the maximum angular momentum ℓ_{max} reduces significantly and looks more realistic, but the estimated fission excitation functions are much lower than the measured data [16] as evident from Table 4.2. In view of above analysis, it has been observed that for DCM based calculations the I_S choice is relatively favourable for the estimation of decay cross-sections because of the presence of proximity potential such as Blocki *et al* [19].

Table 4.3: The DCM obtained fission and experimental [20–22] excitation functions for n+^{232}Th→^{233}Th*, n+^{238}U→^{239}U*, p+^{232}Th→^{233}Pa* and p+^{238}U→^{239}Np* reactions at E∼27 MeV.

Reaction	Compound Nucleus	Temperature (MeV)	ΔR (fm)	$\sigma_{Fission}^{DCM}$ (b)	$\sigma_{Fission}^{Expt.}$ (b)
^{232}Th(n,f)	^{233}Th	1.119	1.071	0.678	0.677
^{238}U(n,f)	^{239}U	1.115	1.126	1.580	1.571
^{232}Th(p,f)	^{233}Pa	1.128	1.129	1.198	1.190
^{238}U(p,f)	^{239}Np	1.101	1.122	1.558	1.540

4.2.3 Comparative analysis of n- and p-induced fission

Lastly, the behavior of n-induced reactions at relatively lower energy i.e. E∼27 MeV is studied. Also the role of projectile is examined by studying reactions involving charged particle-proton beam as projectile in addition to the neutral neutron beams. Fig. 4.7(a,b) shows the preformation probability of n+^{232}Th→ ^{233}Th* and n+^{238}U→^{239}U* reactions compared with p+^{232}Th→ ^{233}Pa* and p+^{238}U→^{239}Np* reactions plotted in panel (c,d) at E∼27 MeV. By comparing the upper panel of Fig. 4.7 with upper panel (a,b) of Fig. 4.2, we found that the structure of ^{233}Th* and ^{239}U* nuclei remain identical independent of the energy involved. Minor variation in mass distribution of ^{233}Th* nucleus around the symmetric fission fragments is still evident at lower energies. However, the change in magnitude of preformation probability is observed while going from E_n=32.8 MeV to 27 MeV. Further, on comparing the mass distribution for n-induced reactions (upper panel) with that of p-induced reactions (lower panel) the mass distributions for all the four actinide nuclei are asymmetric, independent of the projectile used. It is noticed that the structure of preformation probability is almost identical for chosen reactions, except for some minor variations in heavy mass fragment region. Whereas, the fission fragments (ff) contributing towards n-induced reactions are identical to that observed for the p-induced reactions. This suggests that the contribution of fission fragments is independent of choice of projectile (i.e. proton and neutron). An explicit representation of the cross-sections for neutron as well as proton induced reaction for the use of spherical approach is presented

in Table 4.3, and show good agreement with the measured fission data [20–22].

4.3 Various fission mechanisms of $^{216}Th^*$ formed in heavy ion induced reaction

After analyzing the n- and p-induced fission of actinide nuclei, this section is devoted to the investigation of various fission mechanisms of $^{216}Th^*$ nucleus formed in heavy ion induced reaction $^{32}S+^{184}W$ at center-of-mass energies around the Coulomb barrier (i.e., $E_{c.m.}$=118.8 to 195.9 MeV). As discussed in section 4.1, this heavy ion induced reaction has possibility to decay via various CN and nCN fission mechanisms such as fusion-fission (ff), quasi fission (QF) and fast fission (FF). The DCM approach has been used to address the CN and nCN processes governed in the decay of pre-actinide, actinide and superheavy nuclei [12–14, 23–27]. It may be noted that the collective clusterisation approach is being utilized for the first time to investigate the dynamics associated with fast fission mechanism. First, in section 4.3.1, the CN (ff) and nCN (QF and FF) fission contributions are studied within DCM. The characteristic behaviour of fragmentation potential, preformation probability P_0, tunneling probability P and scattering potential are analyzed at different incident energies and angular momentum values for considered mechanisms. In this study, the deformation effects are included up to the quadrupole deformations (β_2-static) using optimum orientations ($\theta_i^{opt.}$) approach. Knowing that the anisotropy (A) is an effective tool to investigate the presence/absence of CN and nCN components, the fission anisotropies are obtained within standard saddle-point statistical model (SSPSM) [28] by utilizing DCM parameters. In addition to this, compound nucleus fusion/formation probability P_{CN} is determined as a function of centre-of-mass energy $E_{c.m.}$, to see the impact of CN and nCN contributions in the total capture cross-sections. Further, section 4.3.2 presents the possible role of temperature-dependent deformations (β_2-dynamic) on the various decay mechanisms of $^{216}Th^*$ nucleus.

4.3.1 CN and nCN fission of $^{216}Th^*$ at energies across the barrier

Fig. 4.8(a) depicts the fragmentation potential $V_R(\eta,T)$ for $^{216}Th^*\rightarrow A_1+A_2$ reaction at two extreme energies $E_{c.m.}$=118.8 and 195.9 MeV, at minimum (ℓ_{min}) angular momentum, while Fig. 4.8(b) depicts the behaviour at maximum (ℓ_{max}) angular momentum. The cal-

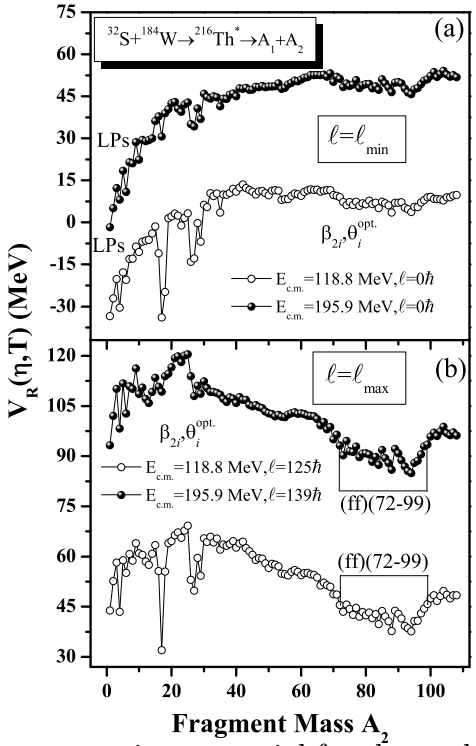

Figure 4.8: Mass fragmentation potential for the nuclear system ^{216}Th* formed in ^{32}S+^{184}W reaction at extreme energies $E_{c.m.}$=118.8 and 195.9 MeV, using the best fitted ΔR's, plotted for (a) minimum (ℓ_{min}) and (b) maximum (ℓ_{max}) values of angular momentum.

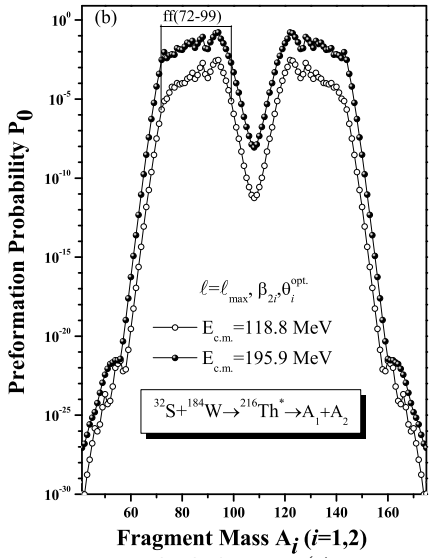

Figure 4.9: The preformation probability $P_0(A_i; i=1,2)$ for the fission of excited ^{216}Th* nucleus at two extreme $E_{c.m.}$=118.8 and 195.9 MeV, for ℓ_{max} states.

culated T-dependent collective potential energy $V_R(\eta,T)$ gives the relative contribution of possible decay fragments. It is noticed from figure that lower ℓ-states are energetically more favourable for light particles (LPs) and higher ones for the fission fragments (ff). The magnitude of fragmentation potential show increment with increase in $E_{c.m.}$ and ℓ-values. At extreme energies, the structure of fragmentation potential for evaporation residues ($A_2 \leq 4$) and intermediate mass fragments (IMFs) is different whereas the structure of fission region remains almost same. Further, at higher angular momentum and extreme energies, the fission region depicts a potential energy minima (equivalently, the maxima in preformation probability P_0, see Fig. 4.9). This confirms that the fission component dominates at the large ℓ-value. Moreover, at extreme $E_{c.m.}$, the minima in fragmentation potential corresponds to the same fragment mass range, i.e. A_2=72-99 (plus complementary fragments). The variation of potential energy surface reveals that the ^{216}Th* shows asymmetric mass distribution, which is in line with the observations drawn for ^{233}Th* nucleus formed in neutron induced reaction, $n+^{232}\text{Th}\rightarrow^{233}\text{Th}^*$ studied in the pervious section 4.2.1. This suggests that, the potential energy surface(s) for Th nucleus are independent of the nature of projectile and energy range involved.

After studying the fragmentation potential, the dynamics of $^{32}\text{S}+^{184}\text{W}$ reaction through the preformation probability P_0 (see Fig. 4.9), varying with fragment mass at ℓ_{max} is analyzed, as fission contribution becomes dominant at higher ℓ-states. Comparing the preformation profile at extreme energies, it is observed that the magnitude of P_0 changes while the mass distribution for fission fragments remains identical and asymmetric in nature, independent of the $E_{c.m.}$.

As stated above, the anisotropy of fission products serves as an effective probe to explore the CN and nCN contributions in the heavy ion induced reactions. Henceforth, in this work, the fission fragment anisotropies (A) of $^{32}\text{S}+^{184}\text{W}$ reaction are estimated within standard saddle-point statistical model (SSPSM) [28] by utilizing DCM-based parameters for the non-sticking (I_{NS}) choice of moment of inertia [25]. Note that in DCM, the fission excitation functions are obtained using the sticking-limit of moment of inertia (I_S). In the later choice, the touching nuclei rotate around their center-of-mass. The choice of I_S-limit is attributed to the utilization of proximity potential of Ref. [19]. However, the non-sticking limit I_{NS} is favoured for anisotropy calculations [29, 30]. Generally, the I_{NS}-

Table 4.4: The SSPSM/DCM calculated fission anisotropies using non-sticking limit I_{NS} for moment of inertia for ^{32}S+^{184}W reaction at various $E_{c.m.}$ and compared with experimental anisotropies [10]. Also shown are the anisotropy-fitted neck-length parameter ΔR and other relevant quantities.

$E_{c.m.}$	E^*_{CN}	T	ℓ_{max}	ΔR	Anisotropy (A)	
(MeV)	(MeV)	(MeV)	($\hbar$)	(fm)	Cal.	Expt.
118.8	37.2	1.266	16	0.726	1.50	1.51
123.1	41.5	1.336	25	1.070	2.10	2.16
127.3	45.8	1.402	27	1.130	2.22	2.27
131.5	50.0	1.464	33	1.250	2.67	2.74
135.8	54.3	1.525	34	1.260	2.68	3.06
141.1	58.5	1.582	35	1.270	2.71	3.28
144.4	61.8	1.626	36	1.300	2.74	3.80

limit is used to determine the experimental ℓ-value. Table 4.4 presents the calculated and experimental fission anisotropies for ^{216}Th* nucleus at different incident energies. The estimated anisotropies match nicely with the experimental anisotropies, except for higher excitation energies above the Coulomb barrier (∼136 MeV). The deficient in anisotropy at higher energies indicates the presence of some competing nCN processes, e.g. QF and FF. In SSPSM approach, it is assumed that the fission fragments may decay towards the symmetry axis of the compound system and the projection of the total angular momentum on this axis is conserved from saddle to scission point [31]. For heavier nuclear systems, this assumption may not be justified due to the different nuclear configurations at these points. Therefore, in the present case, the SSPSM may not just properly describe the fission anisotropies in reactions with massive nuclei at higher energies. Hence, it may be concluded that the anomalous behaviour of fission anisotropies indicates the presence of nCN content in the decay of ^{216}Th* nucleus especially at above barrier energies.

In addition to this, the mass asymmetry (α_e) of interacting nuclei and the product of $Z_P Z_T$ play significant role to decide the contributions from nCN fission processes. As discussed in chapter 1, section 1.4, that if $\alpha_e < \alpha_{BG}$ then there is a possibility of nCN contributions [32]. Here, α_{BG} is "Businaro Gallone mass asymmetry parameter" [6].

Table 4.5: The DCM-calculated fusion-fission σ_{ff}, quasifission σ_{QF} and fast fission σ_{FF} cross-sections for $^{216}Th^{*}$ nucleus at $E_{c.m.}$'s ranging from 118.8 to 195.9 MeV. The predicted evaporation residue (ER) contribution using ΔR_{ER}=ΔR_{ff}+0.5 fm are also presented. The total sum of all evaporation and fission excitation functions (i.e.$\sigma_{Capt.}$=σ_{ER}+σ_{ff}+σ_{QF}+σ_{FF}) compared with the data of Ref. [10]. Also other relevant quantities are shown below.

$E_{c.m.}$ (MeV)	E^{*}_{CN} (MeV)	T (MeV)	ℓ_{max} ($\hbar$)	ΔR_{ER} (fm)	σ_{ER} (mb)	ΔR_{ff} (fm)	σ_{ff} (mb)	ΔR_{QF} (fm)	σ_{QF} (mb)	ΔR_{FF} (fm)	σ_{FF} (mb)	$\sigma^{DCM}_{Capt.}$ (mb)	$\sigma^{Expt.}_{Capt.}$ (mb)
118.8	37.2	1.266	125	1.169	0.00173	0.669	0.0096	0.300	0.0263	0.529	0.0024	0.04	0.04
123.1	41.5	1.336	125	1.250	0.0951	0.750	0.886	0.625	1.45	0.545	0.007	2.44	2.35
127.3	45.8	1.402	125	1.392	0.0852	0.892	16.08	0.848	12.7	0.549	0.012	28.87	22.97
131.5	50.0	1.464	125	1.490	0.974	0.990	47.0	0.918	28.8	0.566	0.0306	76.80	81.01
135.8	54.3	1.525	125	1.554	1.48	1.054	82.6	0.960	42.9	0.577	0.064	127.04	132.27
141.1	58.5	1.582	126	1.584	2.20	1.084	109.4	0.990	58.3	0.628	0.756	170.66	189.33
144.4	61.8	1.626	126	1.625	3.87	1.125	141.0	1.020	75.5	0.668	2.44	222.81	237.06
157.6	76.0	1.800	129	1.675	7.53	1.175	264.0	1.090	150.0	0.750	52.8	474.33	580.0
183.2	101.0	2.072	136	1.680	10.7	1.180	292.0	1.210	460.0	0.845	154.4	917.10	985.0
195.9	114.0	2.200	139	1.685	17.2	1.185	300.0	1.240	581.0	0.846	216.0	1114.2	1110.0

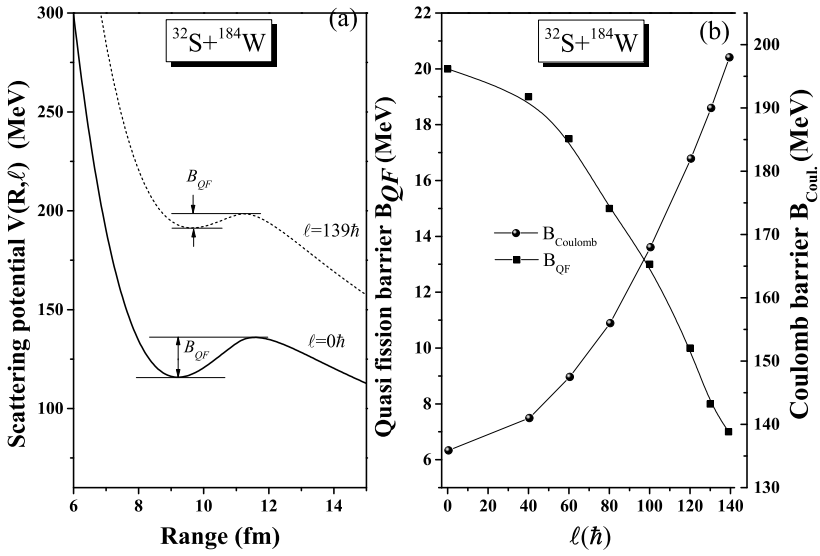

Figure 4.10: (a) Variation of interaction potential ($V(R) = V_P + V_C + V_\ell$) with R (fm) for quasifission at $E_{c.m.}$=195.9 MeV for ℓ_{min} and ℓ_{max} values. (b) Variation of quasifission barrier (B_{QF}) and Coulomb barrier ($B_{Coul.}$) with $\ell(\hbar)$ at $E_{c.m.}$=195.9 MeV.

For the considered ^{32}S+^{184}W reaction, α_e(=0.703)< α_{BG}(=0.864), which suggests the existence of nCN content. Further, due to the large entrance channel Coulomb repulsion (i.e. Z_PZ_T=1184), the nCN content is expected to contribute towards the total capture cross-sections.

Therefore, after attaining an insight of the fusion-fission dynamics and fission anisotropies, the contribution of competing nCN decay channels in the decay of ^{216}Th* nucleus is estimated. As per the experimental observations of Zhang *et al.* [10], the capture cross-sections ($\sigma_{capt.}$) includes only contributions from CN and nCN processes, i.e. $\sigma_{capt.}$=σ_{CN}+σ_{nCN}. The pure compound nucleus formation cross-sections (σ_{CN}) includes evaporation residue (ER) and fusion-fission (ff) excitation functions: σ_{CN}=σ_{ER}+σ_{ff}. On the other hand, the hinderance in the formation of CN can be addressed in terms of nCN cross-sections (σ_{nCN}) which involve contributions from quasifission (QF) and fast fission (FF) processes, i.e. σ_{nCN}=σ_{QF}+σ_{FF}. The ΔR-values for ff, QF and FF are optimized in reference to [10], where relative contribution of different fission mechanisms is explored. Note that the excitation functions are estimated using partial wave analysis as described in Eqs. (2.38-2.41) of chapter 2. The QF contributions are calculated by considering preformation probability equal to unity for the entrance channel [33] see Eq. (2.40) of

chapter 2, since for quasifission process the reactant partners are supposed to retain their identity [34, 35]. Here, the penetration probability is calculated as for the decay fragments identical to incoming channel (P_{ic}) using WKB approximation. Further, the fast fission products has alike properties as that of usual ff fragments [36]. In this case, P_0 is calculated by solving Schrödinger equation for fission fragments (A_2=72-99 plus complementary fragments) for angular momentum values varying from ℓ_{Bf} to ℓ_{max} (where ℓ_{Bf} is an angular momentum where fission barrier disappears [37]). Here, barrier penetration probability is considered to be maximum (i.e. P=1) in agreement with the Ref. [38]. ℓ_{Bf} is 70$\hbar$ as per the results obtained by Ref. [39] using the finite range model. Thus, the fast fission contributions are calculated using the Eq. (2.41) of chapter 2. Table 4.5 represents the DCM estimated excitation functions along with corresponding value of neck-length parameter ΔR, temperature T, excitation energies E^*_{CN} and center-of-mass energies $E_{c.m.}$ for ER, ff, QF and FF processes. The ER cross-sections (σ_{ER}) are predicted by using $\Delta R_{ER} = \Delta R_{ff}$+0.5 fm. Note that, the lighter fragments are generally emitted first from the hot and rotating nuclei, establishing the fact that light particle emission occurs prior to the fission process. Keeping this in mind, higher ΔR is taken for ER formation as compared to the fission decay [27]. The estimated σ_{ER} are observed to be negligible small, in accordance with the experimental observations [10]. DCM based cross-sections of ER, ff, QF and FF processes, i.e. $\sigma^{DCM}_{capt.}$ show nice agreement with experimental measured [10] capture data ($\sigma^{Expt.}_{capt.}$) at all energies.

Next, to explore the quasifission (QF) process, the interaction potential V(R,ℓ) is plotted in Fig. 4.10(a) for ^{32}S+^{184}W reaction at $E_{c.m.}$=195.9 MeV, for the minimum (ℓ=0) and maximum (ℓ_{max}=139$\hbar$) angular momentum values. QF is a process when non-equilibrated composite system disintegrates into two parts without reaching the equilibrated shape of compound nucleus (CN). According to the DNS model [10], the depth of the potential well is called quasifission barrier (B_{QF}), as marked in the figure 4.10(a). It is evident from the figure that the interaction potential changes due to the increase in the rotational energy V$_\ell$, and the depth of potential well show decrement with increase in ℓ. That means the value of QF barrier decreases, on the contrary the Coulomb barrier $B_{Coul.}$ increases with increase in ℓ, similar observations can be seen in Fig. 4.10(b) plotted for B_{QF} and $B_{Coul.}$ as a function of ℓ. Clearly, it indicates that at higher ℓ-values, the higher Coulomb barrier

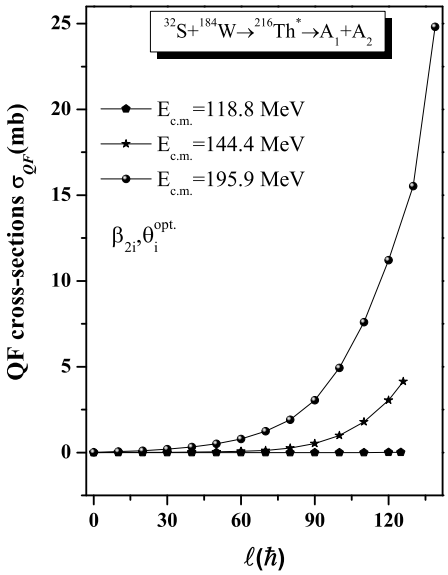

Figure 4.11: (a) A plot of quasifission cross-sections σ_{QF} vs. $\ell(\hbar)$ for ^{216}Th* nucleus at energies $E_{c.m.}$=118.8, 144.4 and 195.9 MeV.

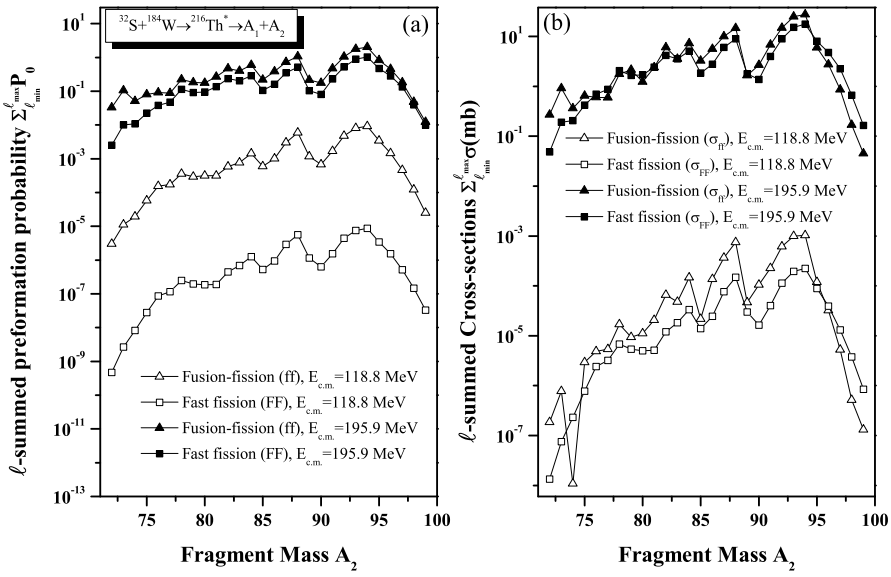

Figure 4.12: (a) ℓ-summed preformation probability $P_0(A_2)$ plotted for ff and FF decay of ^{216}Th* nucleus at two extreme $E_{c.m.}$. Panel (b) represent the same but for ℓ-summed fusion-fission (σ_{ff}) and fast fission (σ_{FF}) excitation functions.

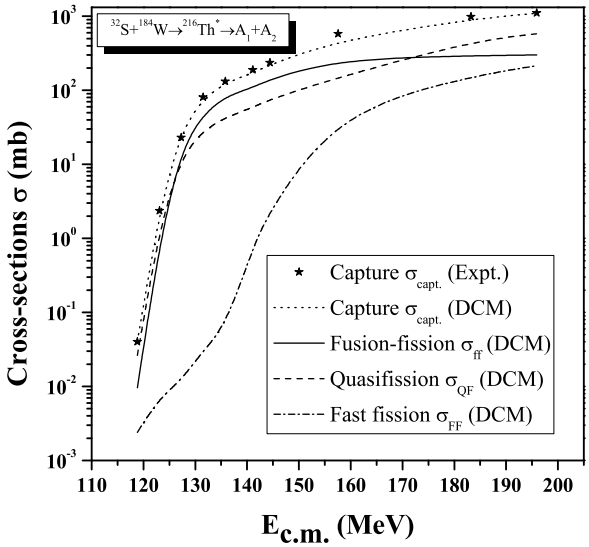

Figure 4.13: Individual contribution of different fission channels as a function of $E_{c.m.}$ and comparison of DCM estimated capture excitation functions with experimental [10] capture data for $^{32}S+^{184}W\rightarrow^{216}Th^*$ reaction.

and lower QF barrier reduces the possibility of formation of equilibrated CN state, and hence the contribution of QF component increases at higher ℓ-values.

The QF cross-sections (σ_{QF}) are shown as a function of ℓ, for three $E_{c.m.}$'s, as shown in Fig. 4.11. At lowest $E_{c.m.}$=118.8 MeV, the variation in QF cross-section at a given ℓ-value is not very significant as compared to two higher $E_{c.m.}$=144.4 and 195.9 MeV. Where the QF contribution is quite small at lower angular momentum values (upto ℓ=50$\hbar$), but for ℓ >50$\hbar$, σ_{QF} increases with increase in ℓ. This result further supports that higher E^*_{CN} and higher ℓ exhibit maximum contribution of quasifission.

After studying the variation of angular momentum and collision energy for the QF mechanism, Fig. 4.12 depicts the ℓ-summed P_0 and σ as a function of contributing fragments (A_2) of fusion-fission (ff) and fast fission (FF) processes for $^{216}Th^*$ nucleus at two extreme $E_{c.m.}$=118.8 MeV and 195.9 MeV. The ff is analyzed for partial waves ℓ=0 to ℓ=ℓ_{max}, and FF process contributes at $\ell_{Bf} \leq \ell \leq \ell_{max}$ window. From figure, it is seen that the preformation probability for both processes follows similar trend, exhibiting significantly large magnitude for ff process. Whereas, at highest $E_{c.m.}$ the probability of preformed FF fragments starts competing with the preformation probability of ff fragments. Similar kind of results can be seen from the panel (b) of Fig. 4.12, the σ_{ff} is larger in magnitude than σ_{FF} at lowest energy, however they compete with each other at

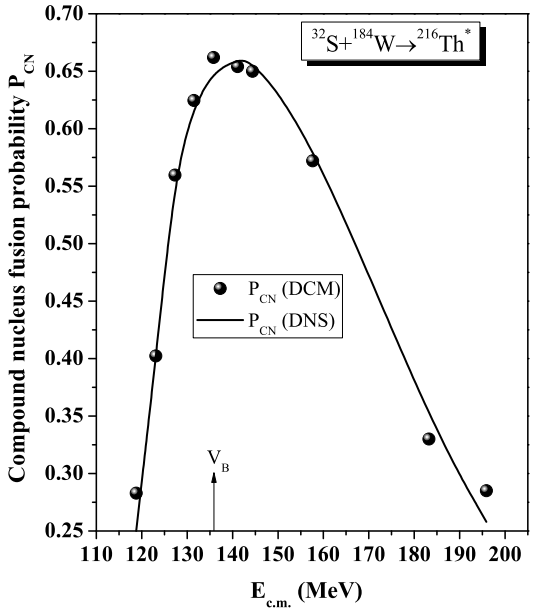

Figure 4.14: DCM calculated compound nucleus fusion/formation probability P_{CN} as a function of $E_{c.m.}$ for ^{32}S+^{184}W$\rightarrow^{216}$Th* reaction, and compared with the DNS calculted P_{CN}.

highest energy. From Fig. 4.11 and 4.12, one may conclude that the nCN fission components has more prominent contribution at higher ℓ-values and higher energies. This observation is in agreement with the conclusion extracted from the anomalous behaviour of fission anisotropies A (see Table 4.4) that the above barrier energies contribute most towards the nCN content.

A relative analysis of DCM obtained excitation functions of fusion-fission, quasi fission and fast fission mechanisms with $E_{c.m.}$ is presented in Fig. 4.13. The predicted ER cross-sections (σ_{ER}) are not shown in this figure as they have negligible values (see Table 4.5). Clearly, one can see from the figure that the contribution of both CN and nCN processes is large at higher energies. The fusion-fission is major contributor to the capture data at energy window 127.3<$E_{c.m.}$<157.6 MeV. Whereas, above 157.6 MeV the multinucleon transfer process such as quasifission has more contribution than fusion-fission, which means that CN formation is hindered at higher energies. The contribution from another nCN process i.e. fast fission is relatively small as compared to other decay processes, but starts competing the fusion-fission process at very high energies. The DCM calculations are made to identify the individual contribution of the different decay processes. It is worth mentioning that the sum of all three fission excitation functions (i.e. $\sigma^{DCM}_{Capt.}$) is in

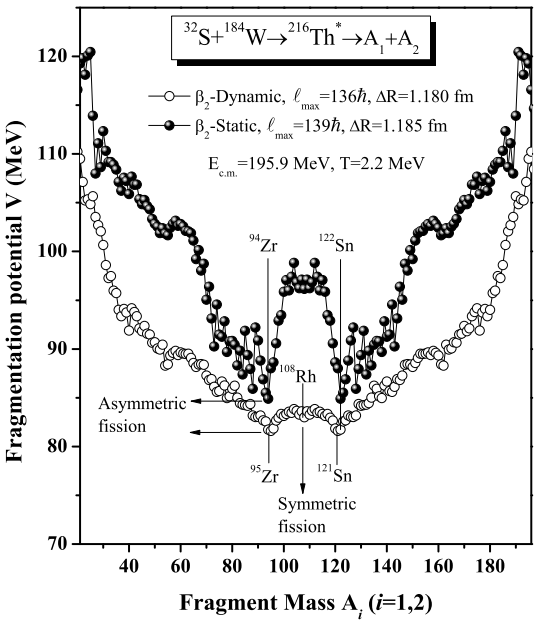

Figure 4.15: Fragmentation potential $V(A_i)$ for ^{216}Th* nucleus shown at $E_{c.m.}$ =195.9 MeV (T=2.2 MeV) for β_2-static and β_2-dynamic deformations of fragments.

agreement with the experimental [10] capture cross-section ($\sigma_{Capt.}^{Expt.}$) over a wide spread of centre-of-mass energies.

Further, the compound nucleus fusion/formation probability (P_{CN}) is calculated for ^{216}Th* nucleus within the framework of DCM at various $E_{c.m.}$-values. The CN fusion probability P_{CN} is a parameter which describes the probability of the complete fusion. If P_{CN} ∼1, it is assumed that there is complete formation of compound nucleus, otherwise presence of other nCN decays is anticipated. The P_{CN} is calculated using following [40]:

$$P_{CN} = \frac{\sigma_{CN}}{\sigma_{CN} + \sigma_{nCN}} = \frac{\sigma_{ER} + \sigma_{ff}}{\sigma_{ER} + \sigma_{ff} + \sigma_{QF} + \sigma_{FF}}. \tag{4.1}$$

Fig. 4.14 illustrates the variation of DCM-calculated P_{CN} as a function of $E_{c.m.}$ for the ^{216}Th* nucleus, and compared with the ones obtained by the dinuclear system model (DNS) [10]. Figure clearly shows the strong hindrance to the fusion/formation of CN at the lowest as well as highest center-of-mass energies. The CN fusion factor first increase with energy upto ∼136 MeV (around Coulomb barrier energy), and then shows decrement with increase in $E_{c.m.}$. Initially, the projectile has not enough energy to overcome the barrier and fuse with the target, hence P_{CN} has smaller values at lower $E_{c.m.}$. However, at above barrier energies, the lowering of P_{CN} factor is connected with the emerging

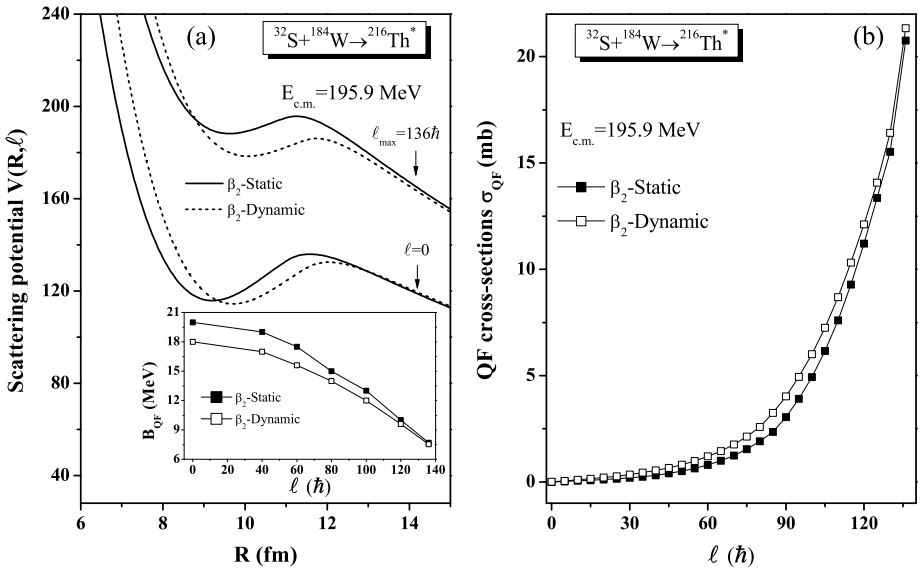

Figure 4.16: (a) DCM calculated scattering potential V(R) plotted for ^{32}S+^{184}W reaction at $E_{c.m.}$=195.9 MeV for β_2-static and β_2-dynamic deformations. Inset of figure shows the comparison of quasifission barrier B_{QF} for both type of deformations. (b) Calculated quasifission cross-sections σ_{QF} plotted for ^{32}S+^{184}W reaction for both choice of deformations.

contribution of nCN fission i.e quasifission and fast fission. The P_{CN} >0.5 for ^{216}Th* nucleus in the energy range 127.3< $E_{c.m.}$ <157.6 MeV due to the large fusion-fission contribution as compared to the nCN excitation functions, see Fig. 4.13. The largest value of P_{CN} for the studied reactions is 0.66.

4.3.2 Role of "dynamic deformations" on the various decay mechanisms of ^{216}Th* nucleus

In this section, the influence of T-dependent deformations of decaying fragments is investigated by comparing the results with the static choice of deformations. Fig. 4.15 depicts the fragmentation potential $V(A_2)$ for ^{216}Th* nucleus at highest $E_{c.m.}$=195.9 MeV (T=2.2 MeV) plotted for β_2-static and β_2-dynamic choices of deformations. Note that at highest $E_{c.m.}$=195.9 MeV the nCN fission mechanisms compete with the CN processes as depicted in section 4.3.1, hence the effect of β_2-dynamic deformations is analyzed at highest energy. Figure indicates that decay structure of fragmentation potential is significantly modified when β_2-static deformations are replaced with the β_2-dynamic deformations. The asymmetric fission forms the dominant decay mode for the choice of β_2-static deformations as discussed in previous section. Whereas, after the inclusion of T-dependent deformations the symmetric fission starts competing the asymmetric component. The

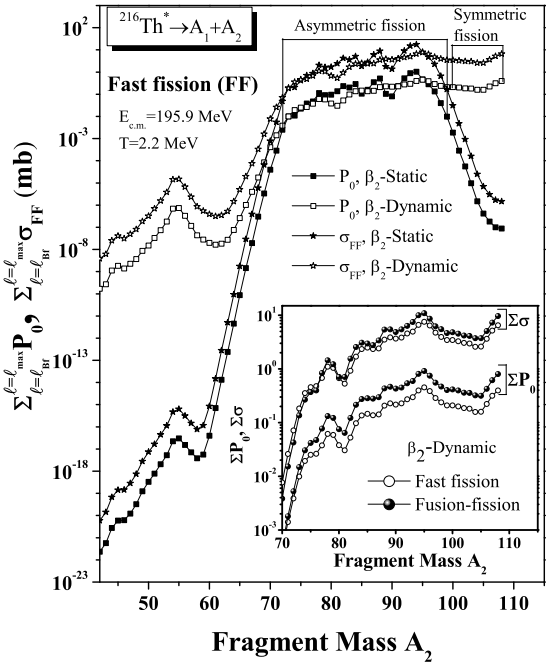

Figure 4.17: (a) The ℓ-summed $P_0(A_2)$ and $\sigma(A_2)$ for the FF process of ^{216}Th* for both β_2-static and β_2-dynamic deformations at $E_{c.m.}$=195.9 MeV. Inset of figure represents the variation of ℓ-summed P_0 and σ for both FF and ff mechanisms for β_2-dynamic case.

DCM-calculations suggest that symmetric fission contributes ∼31% towards the total fusion-fission cross-section of the ^{216}Th* nucleus for β_2-dynamic choice at $E_{c.m.}$=195.9 MeV. Independent of the type of deformations the choice of most preferred decay fragments in the asymmetric fission remains identical. It may be noted that at higher temperature (e.g. T=2.2 MeV), the characteristic behaviour of fragmentation potential is similar for spherical and dynamical choice of deformations (not shown here). Broadly speaking, for the case of β_2-dynamic, the mass distribution gets broaden and more decay fragments start contributing to the fission process including asymmetric (A_2=72-99) and symmetric (A_2=100-108) fission fragments.

For further analysis, the interaction potential V(R) is calculated for ^{32}S+^{184}W reaction using β_2-static and β_2-dynamic choice of deformations as shown in Fig. 4.16(a) at $E_{c.m.}$=195.9 MeV. The use of T-dependent deformations influence the barrier characteristics (barrier position and barrier height), which inturn effect the penetration probability and thereby effect excitation functions. For the case of β_2-dynamic deformations the interaction radius is higher and the interaction barrier is lower as compared to β_2-static

Table 4.6: The DCM-estimated fission excitation functions using β_2-dynamic deformations of fragments for ^{216}Th* system at $E_{c.m.}$=195.9 MeV (T=2.2 MeV).

ΔR	ℓ_{max}	σ
	Fusion-fission (ff)	
1.180 fm	136$\hbar$	302 mb
	Quasifission (QF)	
1.257 fm	136$\hbar$	584 mb
	Fast fission (FF)	
0.550 fm	136$\hbar$	232 mb

case. It may be noted that the minute change in the distance between the two interacting nuclei influence the equilibrium between nuclear, rotational and Coulomb forces. Following this description, the quasifission barrier (B_{QF}) is extracted from the scattering plot (Fig. 4.16(a)) for the β_2-dynamic deformations and compared with the β_2-static case. As interaction radius is large for the dynamic deformations in comparison with the static one, the V_P, V_C and V_ℓ potentials get influenced due to their dependence on R. Hence the overall interaction potential (barrier pocket and barrier height) gets modified after the inclusion of β_2-dynamic deformations. Therefore, the magnitude of B_{QF} is different for both the choices of deformations, i.e. relatively higher magnitude is observed for β_2-static case, as depicted in the inset of Fig. 4.16(a). As a consequence, the QF excitation functions are effected by the choice of deformations as depicted in Fig. 4.16(b). The QF excitation functions increase with increase in ℓ, independent of the choice of deformations, where the magnitude of σ_{QF} is larger for β_2-dynamic case in comparison with the β_2-static deformations.

Finally, to explore the relative study of static and dynamic deformations on fast fission (FF) process, the ℓ-summed preformation probability $P_0(A_2)$ and excitation functions $\sigma(A_2)$, with summation upto ℓ_{max}, are plotted in Fig. 4.17 at $E_{c.m.}$=195.9 MeV. Note that FF process contributes only for $\ell_{Bf} \leq \ell \leq \ell_{max}$ window where fission barrier vanishes. Fig. 4.17 depicts that σ follows the behaviour of P_0, which exhibits an interesting structure with significant contribution of P_0 factor for fission fragments. The behavior of preformation probability P_0 gets modified after the incorporation of dynamic deformations. The mass

distribution starts broadening, both symmetric and asymmetric fission fragments have contribution towards the total fission of ^{216}Th* nucleus. These results are in agreement with the information drawn from Fig. 4.15 for ff process. Beside this, the variation of ℓ-summed P_0 and σ (see inset of Fig. 4.17) for both ff and FF processes shows that the contribution of fast fission competes with the ff component in agreement with β_2-static case at considered energy regime. The cross-sections for ff, QF and FF processes is given in Table 4.6.

4.4 Summary

This chapter consists the fission decay analysis of light particle (n and p) and heavy ion (^{32}S) induced fission of actinide nuclear systems. The temperature, angular momentum, deformations and orientations effects are duly incorporated. First, the fission dynamics of n+^{232}Th$\rightarrow$ ^{233}Th* and n+^{238}U$\rightarrow$^{239}U* reactions is studied at incident energies varying from, E_n=32.8 MeV-59.9 MeV and it is observed that the mass division remains asymmetric independent of choice of projectile and incident energy. As the deformations effects are relatively salient in fission mass region so the analysis is done using spherical approach. Interestingly, the DCM calculations show a minor hump around the symmetric fission fragments in the mass distribution of ^{233}Th* nucleus which disappears completely for heavier nucleus ^{239}U*, in agreement with the experimental measurements. The excitation functions of contributing fission fragments find nice agreement with measured data at all energies. Note that the barrier modification for heavier mass ^{239}U* nucleus is relatively low as compared to ^{233}Th* nucleus. Besides this, from the relative study of isobars of ^{233}Th* and ^{239}U*, i.e ^{233}Pa* and ^{239}Np*, it is observed that the mass distribution for all these nuclei is almost identical. Finally, the relative effect of I_S and I_{NS} moment of inertia is studied, and the result suggests that I_S choice is favourable for the estimation of fission cross sections.

Apart from above, different competing decay mechanisms (ER, ff, QF, FF) emerging via CN and nCN processes of heavy-ion induced reaction ^{32}S+^{184}W$\rightarrow$^{216}Th* are studied within the framework of DCM. The analysis is carried out at energies varying from $E_{c.m.}$=118.8 MeV to 195.9 MeV for the use of β_2-static deformed choice of fragmentation using optimum orientations. The measured fission anisotropies are anomalous with regard

to the SSPSM calculated anisotropies, indicating the presence of nCN content at above barrier region. For the decay of ^{216}Th* nucleus, the fission structure shows asymmetric pattern independent of center-of-mass energy, as observed for n-induced fission of ^{233}Th* nucleus. The capture cross-sections are calculated by adding CN ($\sigma_{ER} + \sigma_{ff}$) and nCN ($\sigma_{QF} + \sigma_{FF}$) contributions, which show good agreement with experimental measurements. As expected, the predicted σ_{ER} are small at all collision energies.

The small QF barrier at higher ℓ-values indicates the large contribution of quasifission mechanism. Consequently, the possibility of compound nucleus formation reduces at higher angular momentum. The fast fission component is analyzed at higher ℓ window ($\ell_{Bf} \leq \ell \leq \ell_{max}$), where the fission barrier disappears. In addition to ℓ-dependence, the CN and nCN contributions also show energy dependence. The contribution of QF and FF increases with increase in energy and start competing the ff process at above barrier energies. The calculated compound nucleus fusion/formation probability P_{CN} depicts strong hinderance to the CN formation at lower and higher energies. The small value of P_{CN} at higher $E_{c.m.}$ is connected with large nCN contributions. Whereas, at lower $E_{c.m.}$ values, the projectile may not have enough energy to cross the barrier and fuse with target nucleus, thereby probability of CN formation is reduced. The maximum value of P_{CN} is 0.66 near the Coulomb barrier. Finally, the role of dynamic deformations on CN and nCN decay of ^{216}Th* nucleus is explored at highest energy. The study reveals that both symmetric and asymmetric fission component start contributing towards the total fission excitation functions after the inclusion of dynamic deformations, whereas the asymmetric fission is the prime contributor for β_2-static case. The barrier characteristics are different for static and dynamic deformations, and accordingly affect the contribution of various decay mechanisms involved in the dynamics of ^{32}S+^{184}W reaction.

At the end, it is concluded that the fission dynamics is different for light particle and heavy ion induced reactions. However, the mass distributions show asymmetric behavior for actinide nuclei formed in both type of reactions. For the case of heavy ion induced reaction, the non-equilibrated nCN processes such as QF and FF contribute in the reaction dynamics at higher energies. However, these effects are absent in light particle induced fission. This represents that the size of reaction partners strongly influence the reaction dynamics and related aspects. Motivating from this analysis, further in chapter 5, a

comparison of tightly bound and loosely bound projectile induced reactions is worked out by considering light as well as heavy mass targets. The main emphasis is once again to explore distinctive features of fission dynamics.

Bibliography

[1] A. Kaur, G. Kaur and M. K. Sharma, Proceedings of the DAE-BRNS Symp. on Nucl. Phys. **61**, 516 (2016).

[2] A. Kaur, G. Kaur and M. K. Sharma, Braz. J. Phys. **48**, 608 (2018).

[3] A. Kaur and M. K. Sharma, AIP Conference Proceedings **2006**, 030001 (2018).

[4] A. Kaur and M. K. Sharma, Phys. Rev. C **99**, 044611 (2019).

[5] C. D. Bowman, Annu. Rev. Nucl. Part. Sci. **48**, 505 (1998); J. -L. Biarrotte, S. Bousson, T. Junquera, A. C. Mueller and A. Olivier, Nucl. Instr. Meth. Phys. Res. A **562**, 656 (2006).

[6] U. L. Businaro and S. Gallone, Nuovo Cimento **5**, 315 (1957); K. Thomas, R. Davies and A. J. Sierk, Phys. Rev. C **31**, 915 (1985).

[7] V. S. Ramamurthy and S. S. Kapoor, Phys. Rev. Lett. **54**, 178 (1985).

[8] V. S. Ramamurthy, S. S. Kapoor, R. K. Choudhury, A. Saxena, D. M. Nadkarni, A. K. Mohanty, B. K. Nayak, S. V. Sastry, S. Kailas, A. Chatterjee, P. Singh and A. Navin, Phys. Rev. Lett. **65**, 25 (1990).

[9] R. Rafiei, R. G. Thomas, D. J. Hinde, M. Dasgupta, C. R. Morton, L. R. Gasques, M. L. Brown and M. D. Rodriguez, Phys. Rev. C **77**, 024606 (2008).

[10] H. Q. Zhang, C. L. Zhang, C. J. Lin, Z. H. Liu, F. Yang, A. K. Nasirov, G. Mandaglio, M. Manganaro and G. Giardina, Phys. Rev. C **81**, 034611 (2010).

[11] A. Kaur, M. K. Sharma, Nucl. Phys. A **957**, 274 (2017).

[12] N. Grover, I. Sharma, G. Kaur and M. K. Sharma, Nucl. Phys. A **959**, 10 (2017).

[13] G. Kaur, K. Sandhu and M. K. Sharma, Phys. Rev. C **94**, 014615 (2016).

[14] A. Kaur, G. Kaur and M. K. Sharma, Nucl. Phys. A **941**, 152 (2015).

[15] N. Grover, G. Kaur and M. K. Sharma, Phys. Rev. C **93**, 014603 (2016).

[16] I. V. Ryzhov, S. G. Yavshits, G. A. Tutin, N. V. Kovalev, A. V. Saulski, N. A. Kudryashev *et al.*, Phys. Rev. C **83**, 054603 (2011).

[17] R. K. Gupta, M. Balasubramaniam, R. Kumar, N. Singh, M. Manhas, and W. Greiner, J. Phys. G: Nucl. Part. Phys. **31**, 631 (2005); R. K. Gupta, M. Manhas and W. Greiner, Phys. Rev. C **73**, 054307 (2006).

[18] S. K. Arun, R. Kumar and R. K. Gupta, J. Phys. G: Nucl. Part. Phys. **36**, 085105 (2009).

[19] J. Blocki, J. Randrup, W. J. Swiatecki and C. F. Tsang, Ann. Phys. (NY) **105**, 427 (1977).

[20] M. B. Chadwick, P. Oblozinsky, M. Herman, N. M. Greene *et al.*, Nuclear Data Sheets **107**, 2931-3060 (2006).

[21] S. A. Badikov, C. Zhenpeng, A. D. Carlson, E. V. Gai *et al.*, International Evaluation of Neutron Cross-Section Standards, International Atomic Energy Agency Vienna (2007).

[22] S. Isaev, R. Prieels, Th. Keutgen, J. V. Mol, Y. E. Masri and P. Demetriou, Nucl. Phys. A **809**, 1 (2008).

[23] G. Sawhney, A. Kaur, M. K. Sharma and R. K. Gupta, Phys. Rev. C **92**, 064303 (2015).

[24] G. Kaur and M. K. Sharma, Phys. Rev. C **87**, 044601 (2013); G. Kaur and M. K. Sharma, Nucl. Phys. A **884**, 36 (2012).

[25] G. Sawhney, G. Kaur, M. K. Sharma and R. K. Gupta, Phys. Rev. C **88**, 034603 (2013).

[26] Rajni, R. Kumar and M. K. Sharma, Phys. Rev. C **90**, 044604 (2014).

[27] M. Kaur and M. K. Sharma, Eur. Phys. J. A **50**, 61 (2014).

[28] R. Vandenbosch and J. R. Huizenga, *Nuclear Fission* (Academic, New York, 1973).

[29] G. Sawhney, R. Kumar and M. K. Sharma, Phys. Rev. C **86**, 034613 (2012).

[30] M. Kaur, M. K. Sharma and R. K. Gupta, Phys. Rev. C **86**, 064610 (2012).

[31] C. Wagemans, *The Nuclear Fission Process* (CRC Press, Boca Raton, FL, 1991).

[32] R. G. Thomas, R. K. Choudhury, A. K. Mohanty, A Saxena and S. S. Kapoor, Phys. Rev. C **67**, 041601(R) (2003).

[33] R. Kumar, M. Bansal, S. K. Arun and R. K. Gupta, Phys. Rev. C **80**, 034618 (2009).

[34] B. B. Back *et al.*, Phys. Rev. C **53**, 1734 (1996); **32**, 195 (1985).

[35] B. B. Back, Phys. Rev. C **31**, 2104 (1985).

[36] A. K. Nasirov, K. Kim, G. Mandaglio, G. Giardina, A. Muminov and Y. Kim, Eur. Phys. J. A **49**, 147 (2013).

[37] B. Borderie, M. Berlanger, D. Gardes, F. Hanappe, L. Nowicki, J. Peter, B. Tamain, S. Agarwal, J. Girard, C. Gregoire, J. Matuszek and C. Ngo, Z. Phys. A: Atoms and Nuclei **299**, 263 (1981).

[38] S. S. Kapoor and V. Ramamurthy, Pramana -J. Phys. Vol. **33**, 161 (1989).

[39] A. J. Sierk, Phys. Rev. C **33**, 2039 (1986).

[40] A. Kaur, S. Chopra and R. K. Gupta, Phys. Rev. C **90**, 024619 (2014).

Chapter 5

Decay analysis of Ge and At isotopes formed in tightly and loosely bound projectile induced reactions

5.1 Introduction

Preceding chapter was devoted to the fission decay investigation of various actinide nuclear systems produced via light particle and heavy ion induced reactions at various bombarding energies. It has been emphasised earlier that the entrance channel properties decisively effect the fission dynamics. The replacement of light particle projectile with the heavier one may lead to the contribution of non-compound nucleus fission content in the total reaction cross-sections. This is due to the fact, that the large Coulomb and rotational energies are associated with the heavy ion induced reactions. Here, a detailed analysis of compound nucleus (CN) and non-compound nucleus (nCN) fission mechanisms is carried out in terms of bombarding energy, angular momentum and dynamic deformation effects etc. The availability of radioactive ion beams at several laboratories has provided an opportunity to explore the extraordinary properties of exotic nuclei. Therefore, tightly and loosely bound He-projectiles with mass number A=3-8 are selected to explore the distinct decay mechanisms by using dynamical cluster-decay model (DCM) approach. The possible contribution of evaporation residue (ER) is also explored in addition to fusion-fission (ff) decay channels of CN. A brief overview of chosen reactions is provided in subsequent paragraph.

The nature of projectile plays very important role in the formation and decay process of the CN. Generally, the CN formed via tightly bound projectiles disintegrate through

light particle emission and/or fusion-fission (ff) channels. The probability of each decay channel depends upon the mass of CN, excitation energy (E^*_{CN}) and related angular momentum (ℓ) etc. However, when a loosely bound projectile strikes the target, the breakup and transfer processes also start contributing towards the total cross-sections. The unusual properties of loosely bound projectile influence the reaction dynamics in two ways, (i) the reduction in the potential barrier due to the larger radius of a loosely bound nucleus, leads to the fusion enhancement, (ii) the loosely bound projectile breaks into two parts due to weak binding of its nuclear constituents, which in turn reduces the complete fusion contributions. The later effect is dominant especially at energies above the Coulomb barrier. The possible role of loosely bound projectile, the reaction excitation functions of different mechanisms induced by tightly and loosely bound projectiles may be compared by opting a suitable target. The selection of target projectile combination is vital to have stable nuclear systems in the outgoing channel. In case of light mass targets, the contribution of evaporation residue is prominent due to the small size of CN. However, the probability of fission enhances when heavier target nuclei are used. Plenty of theoretical and experimental work have been done to understand the dynamics of reactions involving loosely bound projectiles at energies across the barrier [1–4]. Though, this is yet an enigma to the investigators due to complex interplay between the complete fusion and breakup reactions.

In view of above discussion, this chapter is divided into two parts. The first part (i.e. section 5.2) deals with decay of ^{68,70}Ge* compound nuclei formed in ^{4,6}He-induced reactions involving light mass target i.e. ^{64}Zn. In the second part (section 5.3), ^{3,4,6,8}He projectiles are induced on heavier mass target ^{209}Bi to produce the excited $^{212-217}$At* isotopes, which further decay via fission process. Here, ^{3,4}He and ^{6,8}He are tightly and loosely bound nuclei, respectively. It is expected that the light mass ^{68,70}Ge* compound nuclei mainly decay via ER channel. Whereas, ff-channel is the one of the main decay mode of heavier mass $^{212-217}$At* isotopes. In next section the decay analysis of Ge isotopes is explored.

5.2 Decay analysis of $^{68,70}Ge^*$ isotopes formed in $^{4,6}He+^{64}Zn$ reactions

The decay analysis of $^{68}Ge^*$ and $^{70}Ge^*$ compound systems formed respectively in $^{4}He+^{64}Zn$ and $^{6}He+^{64}Zn$ reactions, at center-of-mass energies across the barrier ($E_{c.m.}$~5-16 MeV), is investigated within the framework of DCM [5–10]. Section 5.2.1 deals with the $^{68}Ge^*$ nucleus formed via ^{4}He beam, which mainly de-excites by one- and two-particle evaporation channels like γ, n, p, $2p$, $n\alpha$, $p\alpha$ and 2α. Interestingly, one-particle emission is the dominant decay mode for $^{68}Ge^*$ nuclear system, whereas the contribution of $n\alpha$, $p\alpha$ and 2α is negligible [11, 12]. Moreover, the γ-channel is also not included in the present calculations due to its negligible contribution towards the total reaction excitation functions. The experimental excitation functions of these evaporation channels are addressed individually by optimizing the "neck-length parameter ΔR". The fission contributions are also predicted for this reaction, which comes out to be rather small. Therefore, in both reactions, the fusion process leads to the production of evaporation residues (ERs), hence $\sigma_{fus} \approx \sigma_{ER}$, as the contribution of the ff-channel is not significant for $^{4}He+^{64}Zn$ and $^{6}He+^{64}Zn$ reactions. In section 5.2.2, the fusion cross-sections are addressed for $^{70}Ge^*$ nucleus by summing all the excitation functions of $(2n)^{68}Ge$, $(np)^{68}Ga$, $(2np)^{67}Ga$ and $(n\alpha)^{65}Zn$ evaporation residues. A correlation of calculated and experimental fusion excitation functions for $^{6}He+^{64}Zn \rightarrow ^{70}Ge^*$ reaction suggests the possibility of occurrence of breakup and transfer events due to loosely bound feature of the ^{6}He projectile. It may be noted that, ^{65}Zn ER may also formed via breakup and two neutron ($2n$) transfer process, in addition to the αn evaporation channel [13]. Further, the suppression in $2np$ excitation functions is associated with the incomplete fusion of residual component of ^{6}He nucleus i.e. $^{4}He+^{64}Zn$. Thus, an effort is made to estimate the breakup+transfer contribution by including the relevant energy corrections in reference to the breakup of ^{6}He projectile into ^{4}He and $2n$. Finally, a comparative study of tightly and loosely bound projectile induced nuclear reactions is carried out in section 5.2.3, to analyze the influence of halo structure of the projectile on the considered reaction dynamics. The obtained results from these studies are published in Ref. [14].

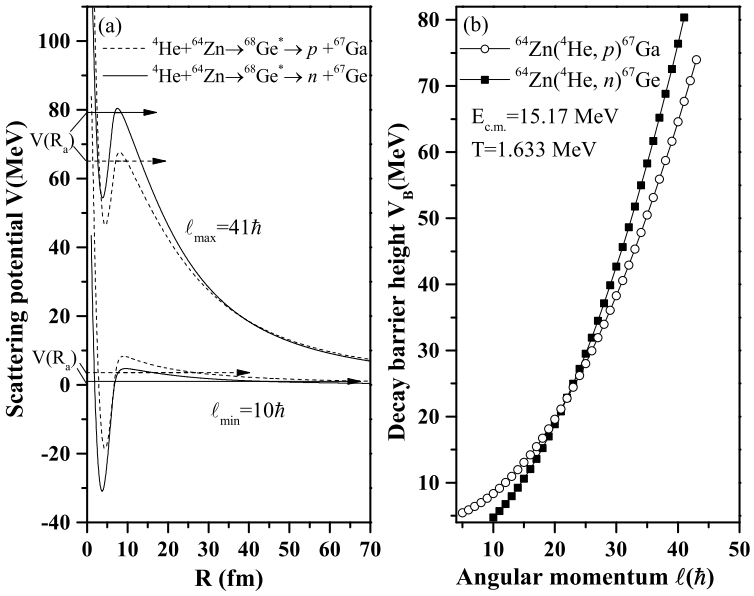

Figure 5.1: (a) Scattering potential V(R) for ^{68}Ge*→p+^{67}Ga and ^{68}Ge*→ n+^{67}Ge decay channels at $E_{c.m.}$=15.17 MeV, estimated for ℓ_{min}=10ħ and ℓ_{max}=41ħ values. (b) Variation of DCM-calculated decay barrier height as a function of $\ell(\hbar)$ for both emissions.

5.2.1 Evaporation residue and fission decay of ^{68}Ge* nucleus formed using tightly bound ^{4}He beam

To explore the dynamics engaged with the one particle emission, the barrier characteristics of ^{68}Ge*→p+^{67}Ga and ^{68}Ge*→n+^{67}Ge decay channels are plotted in Fig. 5.1(a) at highest incident energy E$_{c.m.}$=15.17 MeV and extreme angular momentum states ℓ=10ħ and 41ħ. Interestingly, both the decay channels show different barrier characteristics at different ℓ-states. Clearly, at ℓ_{min}=10ħ, the barrier height (V$_B$) is higher for proton-emission in comparison to the neutron-decay, and is maintained upto ℓ=22ħ as depicted from Fig. 5.1(b). However, these results show reverse trend at higher angular momentum states upto ℓ_{max}=41ħ. This may be due to the interplay between the various potentials contributing towards the barrier height. In order to explore this, Fig. 5.2(a) is plotted which depicts the centrifugal potential for proton and neutron emissions at different angular momentum states. The centrifugal potential remains higher for neutron-decay for majority of ℓ-states. The same is true for the proximity potential, but not shown here. However, with the addition of the Coulomb term in Fig. 5.2(b), the magnitude of the

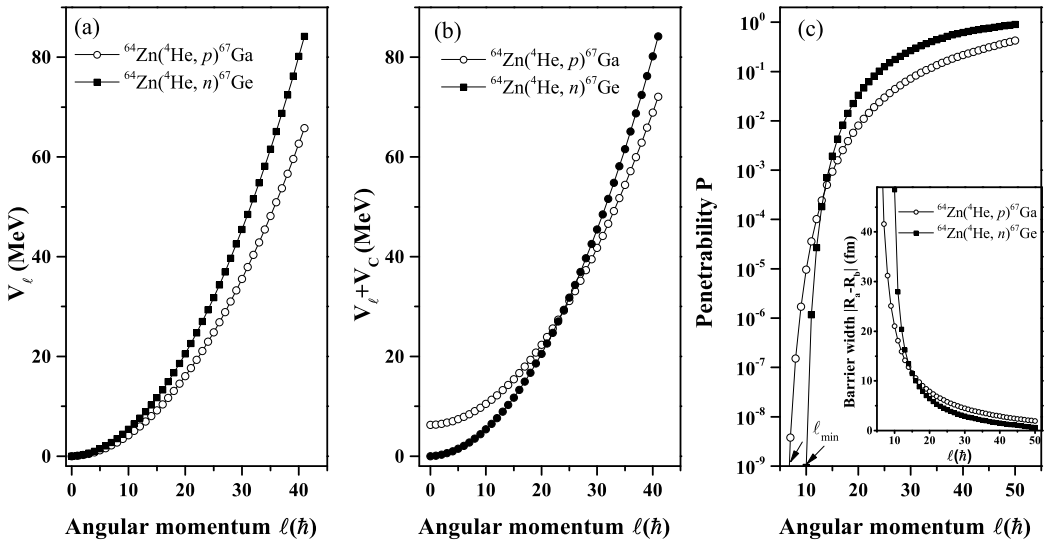

Figure 5.2: (a) Variation of the centrifugal potential V_ℓ for the proton and neutron emissions with $\ell(\hbar)$ at highest $E_{c.m.}$=15.17 MeV. (b) Same as that of panel (a), but plotted for Coulomb+centrifugal potentials. (c) Variation of DCM-calculated barrier penetrability (P) as a function of $\ell(\hbar)$ for the same. The inset of Fig.(c) shows the behavior of barrier width varying with angular momentum.

potential for the neutron emission decreases for lower ℓ-values, leading to higher barrier height for the proton decay. Elaborating this, the larger barrier height for the proton emission at lowest ℓ-state is mainly due to the dominance of Coulomb term at lower angular momentum states, where the suppression in the magnitude of centrifugal potential is simultaneously noticed. At lower ℓ-states, $\ell(\ell+1)\sim\ell^2$ term in the centrifugal potential, does not contribute much, hence the dominance of Coulomb factor can be felt for the proton decay. However, the Coulomb potential remains zero for the neutron emission resulting higher barrier for the proton at $\ell_{min}=10\hbar$ state. In contrast to this, the magnitude of the centrifugal potential competes the Coulomb term and gradually becomes larger in magnitude for the higher ℓ-values. Due to less influence of the Coulomb term at higher ℓ-states, the barrier height get suppressed for the proton emission (see Fig. 5.1(b)). In other words the Coulomb and centrifugal potentials play a significant role to define the barrier characteristics of the proton and neutron decays. Note that the emergence of the flip due to different barrier characteristics for proton and neutron emission channels also effect the penetration path (see Fig. 5.2(c)). In addition to the barrier height, barrier width also plays important role to describe the penetration of the fragment through the

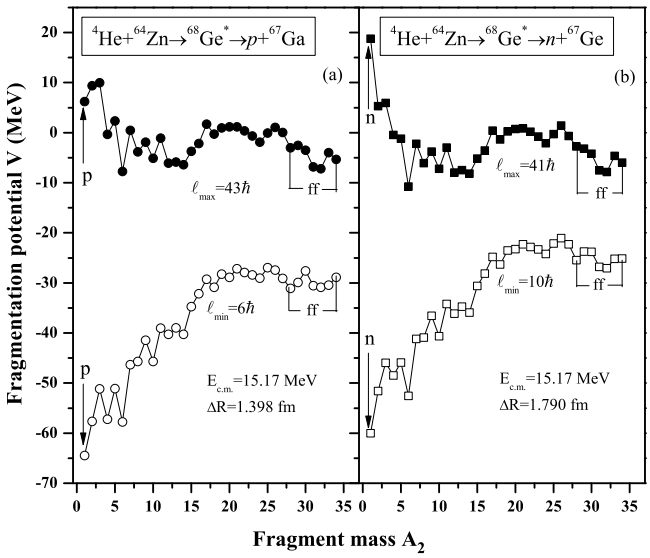

Figure 5.3: Mass-fragmentation potential $V(A_2)$ at $E_{c.m.}$=15.17 MeV for (a)^{64}Zn(^{4}He, p)^{67}Ga and (b)^{64}Zn(^{4}He,n)^{67}Ge decay channels, using best-fit ΔR's, plotted for ℓ_{min} and ℓ_{max} values.

barrier, as evident from Eq. (2.34) in chapter 2. Depending on these factors, the penetrability P shows different behavior for p- and n-decay channels, plotted in Fig. 5.2(c). Specifically, the variation of decay barrier width ($|R_a$-$R_b|$) can be depicted from the inset of Fig. 5.2(c) to illustrate that the penetrability increases exponentially with decrease in barrier width and vice versa. However, it is noticed that P increases with increase in ℓ for both decay channels and in turn sets the minimum value of angular momentum, slightly different for both particles.

In the next step, to investigate the fragmentation path of $^{68}Ge^*$ nucleus via p- and n-particle evaporation channels, the mass-fragmentation potential $V(A_2)$ is illustrated in Figs. 5.3(a,b) at $E_{c.m.}$=15.17 MeV. The results are obtained for both the decay channels using different neck parameter (ΔR), tuned in reference to experimental data. To examine the comparative contribution of energetically favoured fragments, the fragmentation paths are plotted for ℓ_{min} and ℓ_{max} values. One may notice from Figs. 5.3(a) and (b) that the structure of fragmentation potential is almost independent of ℓ value for the fission fragments (ff), but for light particles (LPs) there are significant variations. At lower ℓ-values, the emission of light particles is favorable that means contribution of p- and n-particles is prominent, whereas fission fragments (marked in figure as 'ff') start competing

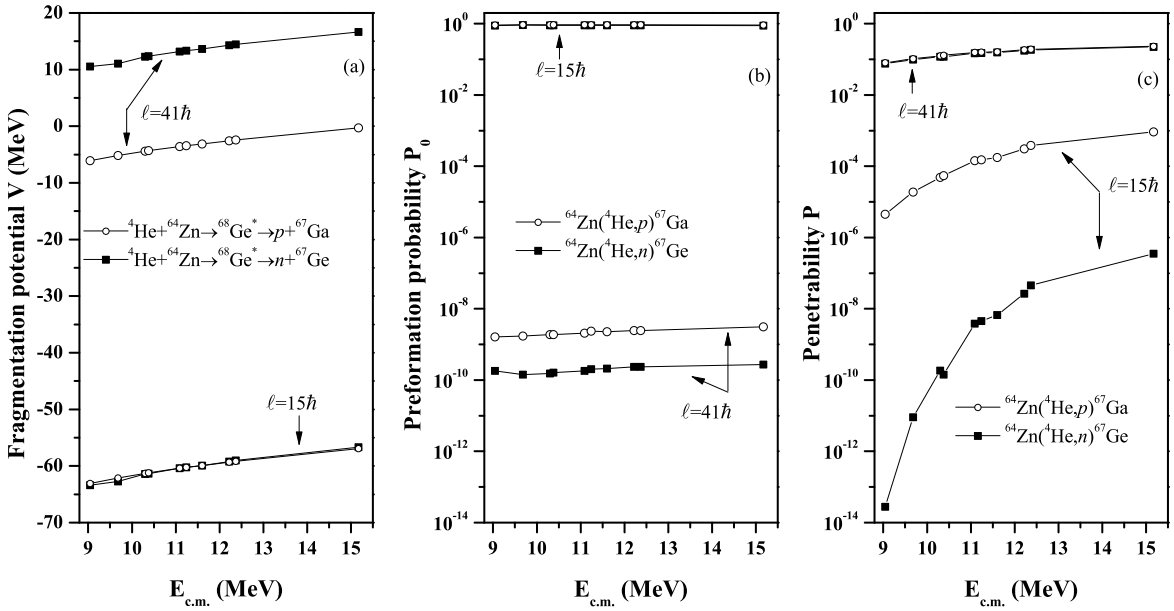

Figure 5.4: The energy ($E_{c.m.}$) dependence of (a) fragmentation potential (V), (b) preformation probability (P_0) and (c) penetrability (P) for proton and neutron evaporation channels at two ℓ-values, 15$\hbar$ and 41$\hbar$.

at higher ℓ-states. Following this, an attempt is made to estimate the fission excitation functions for the decay of $^{68}Ge^*$ nucleus within the framework of DCM, which may be verified by future experiment(s) (refer Table 5.2).

After analyzing the ℓ-dependence of fragmentation decay path for both decay channels, the effect of $E_{c.m.}$ on the fragmentation potential, preformation probability and penetrability is depicted in Figs. 5.4(a), (b) and (c) respectively, at two common ℓ=15$\hbar$ and 41$\hbar$ angular momentum states. These calculations are done at common ΔR, chosen to fit the p-evaporation channel contributions. Clearly, the magnitude of fragmentation potential increases slightly with $E_{c.m.}$ for p- and n-particle emissions. Interestingly, the fragmentation potentials for both channels overlaps at the ℓ=15$\hbar$ angular momentum state, indicating the fact that neutron and proton emissions are equally probable at lower angular momentum states. Whereas, for higher angular momentum the fragmentation behavior of the p- and n-decay channels differs significantly. For example at ℓ=41$\hbar$, the fragmentation potential is much higher for the neutron-emission as that of proton-decay. Lower fragmentation potential for the proton-decay seems to suggest that the p-emission is more favorable towards decay at higher angular momentum state. This outcome is as

per the observation of Fig. 5.1(a), where lower barrier is reported for the proton emission at ℓ_{max} value. This difference in fragmentation potential of n- and p-decay channels at higher ℓ-values enters primarily via rotational energy term due to difference in moment of inertia, as different daughter nuclei are produced in these two channels. It may be noted that ^{67}Ga (the daughter nucleus in p-channel) is prolate deformed with β_2=0.228, whereas ^{67}Ge (the daughter nucleus in n-channel) is oblately deformed with β_2=-0.299. As their radii are changed significantly, so moment of inertia changes accordingly. Note that the minima in the fragmentation potential corresponds to maxima in P_0 profile. The preformation factor P_0 shows opposite trend than that of the fragmentation potential in reference to the ℓ-value. One can see from Fig. 5.4(b), at lower ℓ-value, both n- and p-particles have quite higher magnitude of preformation probability, which in turn, represents that LPs are favorable at lower ℓ-states for all energies. Whereas, at higher ℓ, the P_0 has much lower magnitude, this is in agreement with Fig. 5.3(a) for the fragmentation case. Next, the variation of penetrability P is defined via Fig. 5.4(c), it shows similar results as shown by fragmentation potential, owing maximum magnitude at higher ℓ-state, and indicating the different barrier characteristics for both the emission channels. Also, barrier penetrability (P) shows increment with increase in $E_{c.m.}$ particularly at lower ℓ.

Using the combined effect of P_0 and P values, the ER cross-sections for p- and n-decay channels are calculated within DCM approach, presented in Tables 5.1-5.2, and compared with experimental data [11,12]. The DCM obtained results represent nice agreement with the measurements of Ref. [11,12]. The optimized ΔR's, which decides the enetry point of the penetration path, are listed in the tables and plotted in Fig. 5.5(a). The magnitude of ΔR is more for n-channel as compared to that of p-channel. It may be due to the reason that ^{68}Ge appears below the β stability line and hence seems more prone for p-emission which is in accordance with the result obtained from Fig. 5.4(a). As discussed earlier, the fission fragments (ff) may also contribute in the decay of ^{68}Ge* nucleus, particularly at higher ℓ-states. Thus, in this work, the fission contribution are predicted, and presented in Table 5.2, using ΔR_{ff}=ΔR$_n$-0.5 fm. It is relevant to mention that lighter fragments are generally emitted first from the hot and rotating nuclei, establishing the fact that light particle emission occurs prior to the fission process. Therefore, higher ΔR is considered for ER formation as compared to the fission decay. Similar analysis is carried out in the

Table 5.1: The calculated decay excitation functions for p-evaporation channels using DCM at various $E_{c.m.}$ for ^{4}He+^{64}Zn reaction and compared with experimental data [11, 12]. The other related observable like neck-length parameter (ΔR) and temperature (T) also listed.

$E_{c.m.}$	E^*_{CN}	T	ΔR	$\sigma_p(mb)$	
(MeV)	MeV	(MeV)	(fm)	DCM	Exp. [11, 12]
5.79	9.14	1.168	0.606	2.63×10^{-3}	$(2.65 \pm 0.38) \times 10^{-3}$
5.86	9.21	1.172	0.617	3.01×10^{-3}	$(3.03 \pm 0.40) \times 10^{-3}$
6.16	9.51	1.190	0.716	3.73×10^{-2}	$(3.73 \pm 0.42) \times 10^{-2}$
6.26	9.61	1.196	0.721	3.69×10^{-2}	$(3.69 \pm 0.42) \times 10^{-2}$
6.39	9.74	1.203	0.805	2.94×10^{-1}	$(2.94 \pm 0.33) \times 10^{-1}$
6.52	9.87	1.211	0.804	2.72×10^{-1}	$(2.76 \pm 0.31) \times 10^{-1}$
6.80	10.15	1.227	0.830	4.32×10^{-1}	$(4.38 \pm 0.49) \times 10^{-1}$
7.01	10.36	1.239	0.854	6.98×10^{-1}	$(7.08 \pm 0.80) \times 10^{-1}$
7.04	10.39	1.240	0.846	5.76×10^{-1}	$(5.88 \pm 0.66) \times 10^{-1}$
7.15	10.50	1.247	0.915	2.49	2.52 ± 0.28
7.51	10.86	1.267	0.964	5.89	5.95 ± 0.67
7.70	11.05	1.277	0.984	7.76	7.78 ± 0.88
7.96	11.31	1.291	0.991	7.98	7.96 ± 0.89
8.07	11.42	1.297	1.017	12.2	12.4 ± 1.4
8.47	11.82	1.318	1.091	36.5	36.6 ± 4.1
8.79	12.14	1.335	1.119	49.1	49.8 ± 5.6
9.04	12.39	1.348	1.152	72.4	72.3 ± 7.3
9.68	13.03	1.381	1.204	122	122 ± 13
10.30	13.65	1.412	1.242	171	172 ± 19
10.38	13.73	1.416	1.247	176	177 ± 20
11.09	14.44	1.45	1.290	253	254 ± 28
11.24	14.59	1.457	1.293	255	255 ± 28
11.60	14.95	1.474	1.301	263	265 ± 29
12.22	15.57	1.503	1.329	317	317 ± 36
12.37	15.72	1.510	1.341	343	344 ± 40
15.17	18.52	1.633	1.398	426	428 ± 50

Table 5.2: Same as table 5.1 but for n-evaporation channel. In addition to this, the predicted fission contributions (σ_{FF}) also listed.

$E_{c.m.}$	E^*_{CN}	T	ΔR	$\sigma_n(mb)$		$\sigma_{FF}(mb)$
(MeV)	(MeV)	(MeV)	(fm)	DCM	Exp. [11, 12]	at ΔR_n-0.5fm
9.04	12.39	1.348	1.361	10.6	10.6 ± 1.2	1.58×10^{-2}
9.68	13.03	1.381	1.470	41.3	41.7 ± 4.6	7.98×10^{-2}
10.30	13.65	1.412	1.553	70.2	70.4 ± 7.7	2.60×10^{-1}
10.38	13.73	1.416	1.570	73.5	73.6 ± 8.1	2.86×10^{-1}
11.09	14.44	1.450	1.617	106	106 ± 12	5.54×10^{-1}
11.24	14.59	1.457	1.623	109	109 ± 12	5.84×10^{-1}
11.60	14.95	1.474	1.640	120	120 ± 13	7.18×10^{-1}
12.22	15.57	1.503	1.693	165	165 ± 18	14.44×10^{-1}
12.37	15.72	1.510	1.709	178	178 ± 19	17.56×10^{-1}
15.17	18.52	1.633	1.790	238	240 ± 26	37.20×10^{-1}

earlier work [15] of DCM, based on the decay of Xe-nucleus. At different neck-length parameters 'ΔR_{ff}', the predicted excitation functions of fission fragments (A_2=28-34 and their complementary fragments) are found to be negligibly small, indicating the fact that Ge-nucleus decays primarily via light particles, and fission fragments contribution is negligibly small. Moreover, if the ff cross-sections are calculated at ΔR_{ff}=ΔR_p-0.5 fm, i.e. at the neck-length parameter of proton emission, the fission contribution reduces further. Hence the collective clusterization in light mass region, does not reinforce the fragmentation to follow the fission path, instead ER formation is preferred. In addition to this, the "barrier modification" (ΔV_B) another observable of DCM which can be related to the ΔR (equivalently, R_a), is examined in Fig. 5.5(b). Apparently, ΔV_B (in magnitude) for each particle emission is maximum for lowest $E_{c.m.}$ and minimum at the highest one. It is clear from figure that larger barrier modification is needed for proton-emission in comparison with neutron.

One-particle emission is dominant decay mode of $^{68}Ge^*$ nucleus, as explained earlier. However, experiments [11, 12] also suggest that two-particle emission channels play significant role at energies above than 20 MeV due to the large threshold of multi-nucleon clusters. Although, this work is focused at lower incident energies, but an effort is made

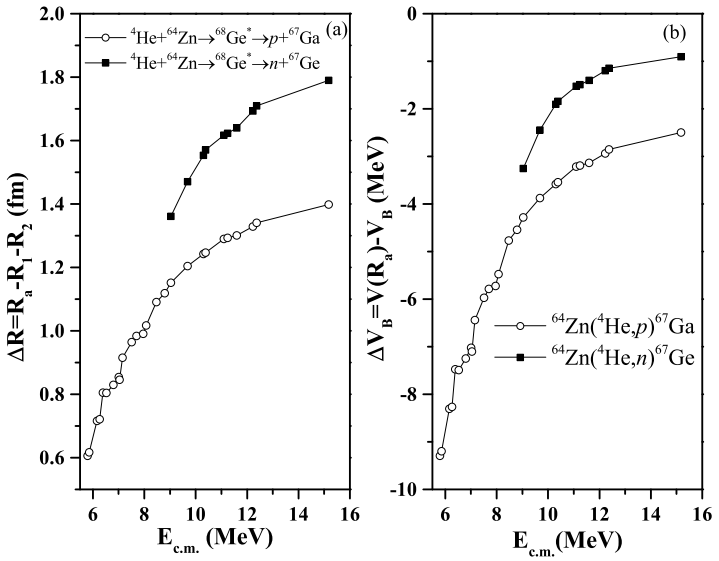

Figure 5.5: (a) ΔR and (b) ΔV_B varying with $E_{c.m.}$ for the decay of $^{68}Ge^*$ nucleus via neutron (solid squares) and proton (open circles) decay channels.

here to check the relative contribution of two-particle emission of $^{68}Ge^*$ nucleus generated in $^4He+^{64}Zn$ reaction. The cross-sections of $^{68}Ge^*\rightarrow 2p+^{66}Zn$ and $^{68}Ge^*\rightarrow \alpha n+^{63}Zn$ decays are calculated at two extreme energies $E_{c.m.}$= 5.79 MeV and 15.17 MeV. The DCM calculated cross-sections are comes out to be σ_{2p}=1.77$\times 10^{-4}$ mb and $\sigma_{\alpha n}$= 1.35$\times 10^{-2}$ mb at lowest $E_{c.m.}$= 5.79 MeV which increases with increase in $E_{c.m.}$ and read as σ_{2p}=1.27 mb and $\sigma_{\alpha n}$=15.17 mb at highest $E_{c.m.}$= 15.17 MeV. These cross-sections are calculated at same ΔR as observed for p-emission, because the previous study [9] of DCM indicates almost similar magnitude of ΔR for one-particle and multi-nucleon emissions. Hence it is evident from above discussion that the estimated cross-sections for $2p$ and αn don't contribute much towards the total reaction excitation functions, as reported in the experimental work [12].

5.2.2 Decay of $^{70}Ge^*$ formed via loosely bound projectile ^6He

After analyzing the dynamics of tightly bound ^4He-induced reaction, the study is extended further to explore the decay of excited $^{70}Ge^*$ nuclear system formed via interaction of two-neutron halo '^6He' projectile and ^{64}Zn target. Interestingly, in recent experiment [13], $^6He+^{64}Zn\rightarrow^{70}Ge^*$ reaction has been studied at various energies across the barrier ranging $E_{c.m.}$ =7.54 to 16.1 MeV. The total fusion excitation functions (σ_{fus}) are obtained

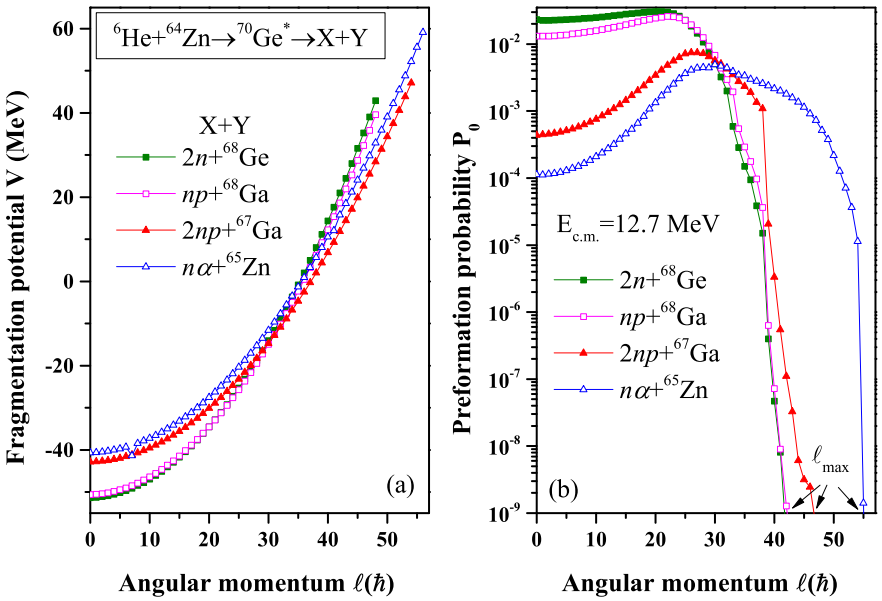

Figure 5.6: The fragmentation potential (V) and preformation probability P_0 vs ℓ plotted for evaporation residues $(2n)^{68}$Ge, $(np)^{68}$Ga, $(2np)^{67}$Ga and $(n\alpha)^{65}$Zn for the de-excitation of ^{70}Ge* system formed via using loosely bound nucleus as a projectile at energy 12.7 MeV.

by measuring the excitation-functions of various evaporation residues (ERs) $(2n)^{68}$Ge, $(np)^{68}$Ga, $(2np)^{67}$Ga and $(n\alpha)^{65}$Zn, as light charged particle emission is the primary decay mode of ^{70}Ge* nuclear system. Apart from ERs, the breakup and transfer events also contribute to the total cross-sections due to loosely bound nature of the ^{6}He projectile. Hence in this section, the evaporation residue, breakup+transfer cross-sections (or equivalently incomplete fusion cross-sections) are addressed using DCM, for overall knowledge of the dynamics of $^{6}He+^{64}Zn\rightarrow^{70}Ge^*$ reaction, so that loosely bound nature of ^{6}He nucleus be explored. The detailed analysis of the above work is carried out in the subsequent discussion.

To study the decay of ^{70}Ge* nucleus, the fragmentation potential V(ℓ) and preformation probability $P_0(\ell)$ are presented in Fig. 5.6 for the evaporation residues of ^{70}Ge* nucleus, corresponding to energy $E_{c.m.}$= 12.7 MeV, above the Coulomb barrier. The different ER decay modes which are shown in figure represent multi-nucleon clusters and heavy residual nuclei, i.e., X+Y$\rightarrow 2n+^{68}$Ge (solid squares), $np+^{68}$Ga (open squares), $2np+^{67}$Ga (solid triangles) and $n\alpha+^{65}$Zn (open triangles). Clearly, the fragmentation potentials for all ER channels show increment with increase in angular momentum. The result

Table 5.3: Excitation functions for individual ER $2n$, np, $2np$ and $n\alpha$ channels with optimized ΔR values for the decay of $^{70}Ge^{*}$ at various $E_{c.m.}$. σ_{fus}^{DCM} calculated by adding all ERs excitation functions and compared with experimental fusion data [13].

$E_{c.m.}$ (MeV)	E^{*}_{CN} (MeV)	T (MeV)	ΔR_{2n} (fm)	$\sigma_{2n}(^{68}Ge)$ (mb)	ΔR_{np} (fm)	$\sigma_{np}(^{68}Ga)$ (mb)	ΔR_{2np} (fm)	$\sigma_{2np}(^{67}Ga)$ (mb)	$\Delta R_{n\alpha}$ (fm)	$\sigma_{n\alpha}(^{65}Zn)$ (mb)	σ_{fus}^{DCM} (mb)	$\sigma_{fus}^{Expt.}$ (mb)
7.54	30.20	2.036	1.592	9.97	-	-	-	-	1.349	14.2	24.17	128.43
9.15	31.81	2.088	1.860	44.6	-	-	1.433	3.37	1.447	18.7	66.67	283.07
10.60	33.26	2.133	1.980	70.1	1.890	106	1.700	16.2	1.650	32.8	225.1	501.08
11.83	34.49	2.171	2.140	116	1.980	139	1.910	34.0	2.020	53.8	342.8	553.85
12.70	35.36	2.197	2.300	165	2.070	174	2.120	55.1	2.070	51.7	445.8	809.01
13.80	36.46	2.230	2.306	164	2.030	150	2.350	72.9	2.150	49.0	435.9	817.81
15.00	37.66	2.266	2.300	153	2.170	209	2.400	72.2	2.200	45.9	480.1	863.29
16.10	38.76	2.298	2.260	141	1.965	114	2.430	71.5	2.250	42.0	368.5	781.04

reflects that light charged particle emission is probable at small values of angular momentum states, due to lower fragmentation potential and larger preformation probability, as shown in Figs. 5.6(a) and 5.6(b) respectively. Similar results are obtained for the decay of ^{68}Ge* nucleus, where the evaporation residue formation dominates at lower ℓ states. Moreover, Fig. 5.6(a) shows that at lower ℓ-states the fragmentation potential increases with increase in mass of the multi-particle cluster, i.e., maximum for $n\alpha$ and minimum for $2n$ cluster, whereas reverse trend is observed at higher ℓ values. As explained earlier in section 5.2.1, this happens because of the relative contribution of Coulomb, proximity and centrifugal potentials to the total fragmentation potential. Due to this, a flip in the magnitude of the fragmentation potential arises around ℓ=30$\hbar$. Similar results are obtained from Fig. 5.6(b), plotted for the preformation probabilities of the decay fragments. The preformation probability shows increment upto certain ℓ-states, then sharply decreases near the ℓ_{max}-values of the cluster emission. The maximum values of the angular momentum can be estimated from Fig. 5.6(b), designated as a point where the contribution of the preformation probability is negligible. Above the ℓ_{max}-values the total cross-sections becomes significantly small.

In reference to above discussion, the angular momentum window $\ell_{min}\leq\ell\leq\ell_{max}$ is fixed and the excitation functions for the evaporation residues of ^{70}Ge* nucleus are estimated using Eq. (2.38) of chapter 2. The ℓ_{min} for all the decay fragments lies around 0$\hbar$, and ℓ_{max}-values are pointed in Fig. 5.6(b), which are different for different clusters. The obtained excitation functions are presented in Table 5.3 for all the clusters. The best-fit values of ΔR for individual ER channels along with T and $E_{c.m.}$ are also listed in Table 5.3. Different ΔR values indicate unique reaction time scales for individual evaporation residue channels. It is of interest to note that the total calculated fusion excitation functions (σ_{fus}^{DCM}) of ^{70}Ge* compound system, i.e., sum of individual ER excitation functions, deviate from the experimental measured fusion excitation functions ($\sigma_{fus}^{Expt.}$) [13]. It is clearly depicted from Fig. 5.7(a) and (b) that the $2n$ and np clusters show nice agreement with the experimental data. Whereas, the mismatch between experimental and calculated excitation functions is observed for the $(n\alpha)^{65}$Zn-cluster (see Fig. 5.7(c)), which is responsible for the decrement in the fusion excitation functions and signify the large contribution of breakup and transfer channels. Moreover, the excitation functions of $2np$-

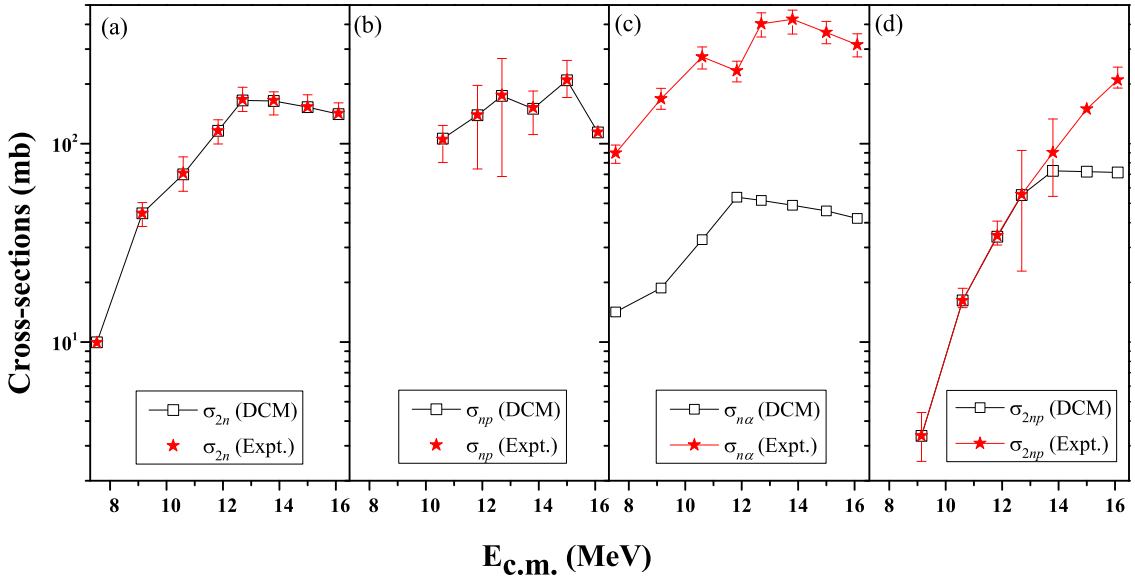

Figure 5.7: Comparison of experimental cross-sections with calculated ones for (a) $2n$, (b) np, (c) $n\alpha$ and (d) $2np$ evaporation channels at several $E_{c.m.}$'s for the ^{6}He+^{64}Zn reaction.

cluster are also underestimated at above barrier energies as shown in Fig. 5.7(d). The results remain intact even at higher values of neck-length parameters. The suppression in the $n\alpha$ and $2np$ excitation functions is governed mainly through the loosely bound nature of the ^{6}He projectile, responsible for the breakup and transfer events. The loosely bound ^{6}He nucleus breaks up into two parts ^{4}He and $2n$ which act as new projectiles and interact with the ^{64}Zn target nucleus individually. It may be noted that ^{65}Zn nucleus is not formed only via $n\alpha$ evaporation channel, but also find its genesis in the breakup and two-neutron transfer channels of ^{6}He projectile, which is addressed in the subsequent discussion, by employing the relevant energy correction. Also, the suppression in $2np$ excitation functions is related with the incomplete fusion of other part of ^{6}He nucleus with target nucleus i.e. ^{4}He+^{64}Zn. In reference to above discussion, the contribution of breakup and transfer channels is included in the present analysis as the difference between estimated and experimental cross-sections, which reads as

$$\begin{aligned} \sigma_{breakup+transfer} &= (\sigma_{n\alpha}^{Expt.} - \sigma_{n\alpha}^{DCM}) \\ &+ (\sigma_{2np}^{Expt.} - \sigma_{2np}^{DCM}) \end{aligned} \tag{5.1}$$

Note that the breakup of loosely bound projectile and interaction of its one part with the

Table 5.4: The obtained breakup+transfer excitation functions using DCM for $1n$ decay channel for $^{66}Zn^*$ excited system formed in the $2n$+^{64}Zn reaction, and $2p$ decay channel for $^{68}Ge^*$ produced in ^{4}He+^{64}Zn reaction at modified energies $E^c_{c.m.}$.

$E^c_{c.m.}$ (MeV)	E^*_{CN} (MeV)	T (MeV)	ΔR (fm)	σ (mb)
$2n$+^{64}Zn→$^{66}Zn^*$→$1n$+^{65}Zn				
2.670	22.08	1.805	1.265	89
3.229	22.64	1.827	1.340	162
3.746	23.16	1.847	1.398	241
3.824	23.24	1.850	1.366	177
4.489	23.90	1.875	1.462	349
4.878	24.92	1.889	1.472	345
5.304	24.72	1.905	1.473	320
5.690	25.10	1.920	1.475	305
^{4}He+^{64}Zn→$^{68}Ge^*$→$2p$+^{66}Zn				
9.470	12.82	1.370	1.570	17.5
10.30	13.65	1.412	2.060	76.0
11.05	14.40	1.448	2.450	112.0

target has been analysed earlier in [9,10]. The 2n and ^{4}He now act as new projectiles and interact with the ^{64}Zn target nucleus individually, and lead to the formation of $^{66}Zn^*$ and $^{68}Ge^*$ nuclear systems, which further decay via n+^{65}Zn and $2p$+^{66}Zn channels respectively. In the above process, the energy correction is required to address the breakup+tranfer process, because the interaction energy must be modified according to the charge and mass number of the new projectiles. The corrected energy (E^c) of new projectile is obtained as [10]

$$E^c = \frac{E}{A} \times A^p - \frac{E}{A} \times A^e \tag{5.2}$$

Here A^p is the mass of projectile before breakup and A^e is mass of ejectile which is an uninteracted outgoing fragment. Hence by including the relevant energy corrections, the breakup and transfer processes and subsequently the decay of $^{66}Zn^*$ and $^{68}Ge^*$ nuclear systems are studied. The modified center-of-mass energies ($E^c_{c.m.}$) and respective excitation energies (E^*_{CN}) are listed in Table 5.4. The corrected energies for breakup channels are smaller in magnitude as compared to the fusion process. Accordingly, the cross-sections are calculated for $1n$ decay of $^{66}Zn^*$ and $2p$ decay of $^{68}Ge^*$ via breakup

and transfer reactions. The temperature (T) and best-fit ΔR values are reported in Table 5.4 and both increase with increase in energy. The angular momentum contributing to the breakup+transfer cross-sections has the limiting values ℓ_{min}=12$\hbar$ and ℓ_{max}=45$\hbar$. The total sum of DCM calculated breakup+transfer and fusion excitation functions show good agreement with the experimental fusion data (refer Fig. 5.8). Broadly speaking, the suppression in the total fusion contributions of ^{70}Ge* CN due to $n\alpha$ and $2np$ channels is compensated through the breakup+transfer events leading to ^{66}Zn* and ^{68}Ge* nuclear systems, followed by $1n$ and $2p$ emission respectively. Conclusively, the loosely bound nature of the ^{6}He projectile influences the dynamics of ^{6}He+^{64}Zn reaction as the total contribution of breakup+transfer channel is reasonably higher than that of the fusion cross-sections.

5.2.3 Comparative analysis of fusion contributions of ^{4,6}He+^{64}Zn reactions

Finally, the comparison of ^{4}He+^{64}Zn and ^{6}He+^{64}Zn reactions is investigated in Fig. 5.8. As described earlier, the fusion excitation functions of nucleus formed in ^{4}He+^{64}Zn reaction match with the experimental data nicely. On the contrary, suppression in the DCM calculated fusion excitation functions are observed for ^{6}He+^{64}Zn reaction channel, due to mismatch in the excitation functions of $n\alpha$ and $2np$-clusters. The comparison of fusion excitation function of ^{4}He+^{64}Zn and ^{6}He+^{64}Zn reactions, depicts below barrier enhancement for ^{6}He+^{64}Zn case. However, the DCM calculated σ_{fus} for ^{6}He+^{64}Zn reaction bear lower magnitude at above barrier region than that for ^{4}He+^{64}Zn. These two results can be explained on the basis of structure properties of loosely bound projectile. The larger radius of the loosely bound projectile reduces the Coulomb barrier, as a result one can expect the fusion enhancement, as shown in Fig. 5.8 at sub-barrier energies.

Besides this, the low binding energy of the outer two neutrons of the ^{6}He nucleus results in larger contribution of breakup+transfer channels which could remove flux from the complete fusion and hence suppress the fusion excitation functions. The DCM results support that at the above-barrier energies, the breakup+transfer processes dominate and result in fusion suppression. Note that similar kind of results have been analyzed for the reactions of loosely bound projectile with heavy target (e.g. ^{11}Be+^{208}Pb [16]). Hence from the above discussion the loosely bound nature of the ^{6}He can be easily illustrated by

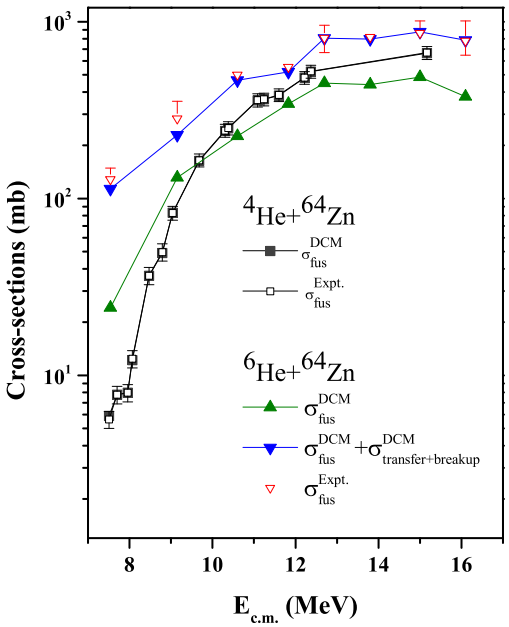

Figure 5.8: Variation of cross-sections with $E_{c.m.}$ for ^{4}He+^{64}Zn and ^{6}He+^{64}Zn reactions and compared with experimental data [11–13].

concluding following results: (i) The loosely bound character of the projectile is responsible for the breakup+ transfer channels which are addressed here via breakup and transfer channels of ^{6}He i.e. $2n$+^{64}Zn and ^{4}He+^{64}Zn. (ii) The comparison of the tightly and loosely bound projectile induced reactions reveals the peculiar dynamics of ^{6}He+^{64}Zn interacting pair. It has been emphasized that the loosely bound nature of ^{6}He is responsible for the sub-barrier fusion enhancement and above barrier fusion suppression.

5.3 Decay analysis of At* isotopes formed in ^{3,4,6,8}He+^{209}Bi reactions

It is emphasised in the previous sections that lighter ^{68,70}Ge* nuclei mainly decay via the ER channels, and predicted excitation functions of fission process are insignificant. In this section, the fission decay of $^{212-217}$At* isotopes produced in ^{3,4,6,8}He+^{209}Bi reactions is examined. A great deal of work have been devoted to measure the reaction cross-sections e.g. evaporation residue [17, 18], fission decay [19–21], ^{4}He yield [22, 23] and transfer and breakup channels [24, 25] of ^{6}He+^{209}Bi reaction. The abundance of neutrons in the loosely bound projectile is expected to have significant impact on the reaction excitation functions. The measured fission contribution of ^{6}He-induced reaction are larger than

the ^{4}He-induced fission contributions at energies higher than Coulomb barrier [19, 21]. However, the results of Kolata *et al.* [20] show large uncertainties in the fission measurements, suggesting that further explorations are required to have better understanding of dynamics. Therefore, it would be interesting to study the fission reactions involving neutron-deficient and neutron-rich He-projectiles on the same target say ^{209}Bi. The analysis is carried out within the framework of DCM. Note that, this study concentrate only on complete fusion-fission mechanism, which means that the contribution of the breakup and incomplete fusion components are not included in this analysis.

This study is divided into three sections. First of all , in section 5.3.1, the fission excitation functions of ^{212}At*, ^{213}At*, ^{215}At* compound nuclei formed, respectively, in ^{3}He+^{209}Bi, ^{4}He+^{209}Bi, ^{6}He+^{209}Bi reactions, are calculated by fixing the "neck-length parameter ΔR", in reference to the available above-barrier fission data [21, 26]. The ΔR-values increases with increase in E^*_{CN} for At isotopes (with CN mass number A_{CN}=212,213,215). Therefore, the linear fit equations of ΔR as a function of E^*_{CN} provide an opportunity to extend the fission analysis below barrier region as well as for heavier isotope ^{217}At* formed in ^{8}He+^{209}Bi reaction. Section 5.3.2 illustrates the fission decay path for four isotopes of At* nucleus in terms of fragmentation potential and fission fragment mass distributions. Further, the influence of N/Z ratio (of compound nuclei) on preformation probability P_0, penetrability P, fission cross-sections $\sigma_{fission}$ and most probable fission fragments, is duly addressed in section 5.3.3.

5.3.1 Fission contributions of $^{212-217}$At* nuclei

In order to calculate the fission excitation functions of ^{3,4,6,8}He+^{209}Bi nuclear systems, first the barrier characteristics of these reactions are analyzed. Fig. 5.9 illustrates the scattering potential (V=V_P+V_C +V_ℓ), for ^{3}He+^{209}Bi, ^{4}He+^{209}Bi, ^{6}He+^{209}Bi and ^{8}He+^{209}Bi reactions at common excitation energy E^*_{CN}=25 MeV, for two extreme ℓ values, i.e., 0$\hbar$ and 139$\hbar$. It is well known that Coulomb barrier (or fusion barrier) is lower for the reaction involving loosely bound projectile as a consequence of large radius. Similar results are observed from the figure that the lower Coulomb barrier is reported for the case of loosely bound projectiles (^{6}He and ^{8}He) as compared to tightly bound He-induced reactions. Another factor which is effecting the fusion barrier and potential well is the neutron number

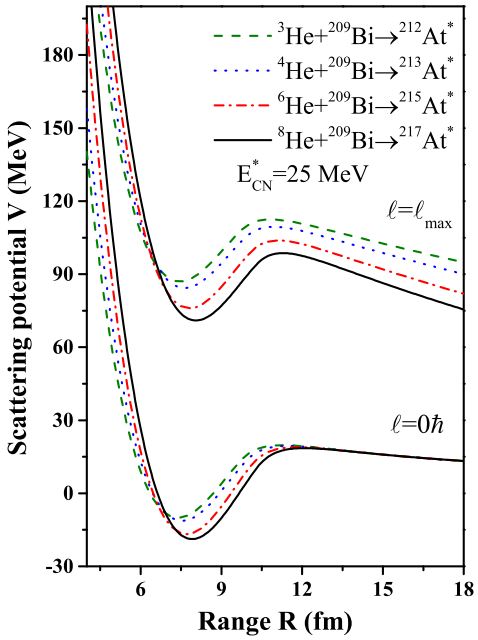

Figure 5.9: The scattering potential V(R) illustrated for ^{3}He+^{209}Bi, ^{4}He+^{209}Bi, ^{6}He+^{209}Bi and ^{8}He+^{209}Bi reactions at E^{*}_{CN}∼25 MeV, calculated for ℓ=0$\hbar$ and ℓ_{max} value.

(N) of the projectile. It is observed that the Coulomb barrier decreases and potential well becomes deeper with increase in neutron number in the projectile nucleus, independent of ℓ values. This is because of the fact that the radius increases with increase in neutron number or equivalently the mass number. The difference in the barrier characteristics significantly effect the tunneling probabilities of fragments through the barrier, and hence the fusion excitation functions. Ultimately, the fusion excitation functions are expected to increase as a function of neutron number of projectile and/or compound nucleus, since common target ^{209}Bi is used in present set of calculations. This in turn suggests that the neutron (N) to proton (Z) ratios of reaction partners are important to decide the fusion probability of a nuclear reaction. In general, the fusion excitation functions are the addition of ER and fission contributions. However, this study will concentrate only on the fission decay process from the complete fusion of He-induced reactions. In a recent work [27], the ER decay analysis has been carried out within the framework of DCM, for ^{9}Li+^{208}Pb reaction forming ^{217}At* compound nucleus, hence not included in present study. In view of above discussion, it will be of further interest to see the effect of abundance of

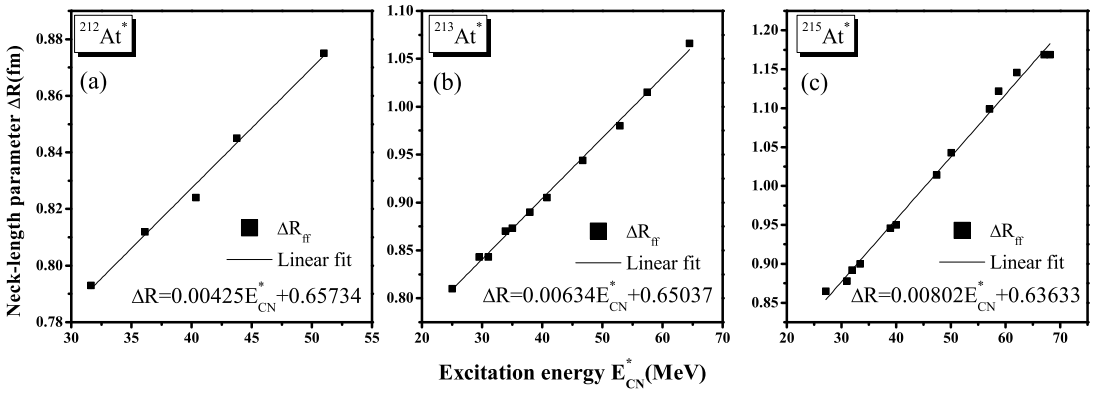

Figure 5.10: Plots of ΔR vs. E^*_{CN} obtained for (a)^{3}He+^{209}Bi (b) ^{4}He+^{209}Bi (c) ^{6}He+^{209}Bi reactions. The linear fit equation of ΔR are also presented for each case.

neutrons and loosely bound characteristics of projectile (such as barrier characteristics) on fission dynamics.

Table 5.5 represents the DCM-calculated fission excitation functions ($\sigma_{fission}$), and other related quantities of ^{212}At*, ^{213}At* and ^{215}At* nuclei. The cross-sections are fitted using the neck-length parameter ΔR in reference to the available fission data [21, 26] at above barrier energies. The obtained fission excitation functions demonstrate the nice agreement with experimental data. The fission contributions is higher for loosely bound projectile induced reaction (^{6}He) as compared to tightly bound projectile (^{3}He, ^{4}He) induced reactions. In other words, the fission excitation functions increases with increase in neutron number of projectile nucleus (or compound nucleus). As discussed earlier, it is of interest to explore the fission enhancement or suppression for ^{6}He induced reaction in reference to the use of tightly bound ^{4}He-induced reaction. An effort is made here to clarify this point, by calculating the fission excitation functions at same ΔR for ^{4}He+^{209}Bi and ^{6}He+^{209}Bi reactions. The DCM-calculated fission excitation functions are presented in Table 5.6 at different excitation energies E^*_{CN}. Even for same ΔR, the magnitude of fission excitation functions is higher for ^{6}He-induced reaction in comparison with tightly bound ^{4}He-induced one. This signify that the larger radius and lower barrier of loosely bound ^{6}He-induced reaction lead to the fission enhancement. Hence, it is evident here that the binding strength of projectile has strong influence on the fission contribution.

Note that the significance of "ΔR" parameter used in DCM based calculations is like

Table 5.5: DCM-estimated fission contributions ($\sigma_{fission}$) for ^{212,213,215}At* at above barrier excitation energies E^*_{CN}, and compared with experimental measurements. The fitted ΔR values and other calculated quantities are also presented.

E^*_{CN} (MeV)	$E_{c.m.}$ (MeV)	T (MeV)	ΔR (fm)	ℓ_{max} ($\hbar$)	$\sigma_{fission}$ DCM (mb)	$\sigma_{fission}$ Expt. (mb)
^{3}He+^{209}Bi$\rightarrow^{212}$At$^*\rightarrow$A$_1$+A$_2$						
31.63	24.86	1.180	0.793	143	0.866	0.897
36.12	29.35	1.260	0.812	144	3.28	3.20
40.35	33.58	1.330	0.824	145	10	10.14
43.76	36.99	1.363	0.845	145	18.46	18.41
50.99	44.22	1.492	0.875	146	38.4	38.55
^{4}He+^{209}Bi$\rightarrow^{213}$At$^*\rightarrow$A$_1$+A$_2$						
25.03	33.17	1.050	0.810	139	0.102	0.30
29.50	37.64	1.138	0.843	141	3.1	3.16
31.02	39.16	1.166	0.843	142	4.52	4.73
33.87	42.01	1.218	0.870	142	12.52	12.80
35.04	43.18	1.238	0.873	142	15.66	15.13
37.94	46.08	1.287	0.890	143	28.6	28.36
40.78	48.92	1.334	0.905	143	39	31.73
46.71	54.85	1.426	0.944	143	69.6	70.52
52.93	61.07	1.517	0.980	145	124.2	120.22
57.44	65.58	1.579	1.015	146	169.8	168.35
64.50	72.64	1.672	1.066	147	240	255.01
^{6}He+^{209}Bi$\rightarrow^{215}$At$^*\rightarrow$A$_1$+A$_2$						
27.15	25.62	1.087	0.865	142	6.56	6.62
31.02	29.49	1.161	0.878	143	13.56	13.34
31.90	30.37	1.177	0.892	143	21.8	22.44
33.38	31.85	1.203	0.900	143	35	34.08
38.91	37.38	1.297	0.946	144	108	106.01
39.99	38.46	1.315	0.950	144	109.6	107.47
47.39	45.86	1.430	1.014	146	262	255.63
50.04	48.51	1.468	1.043	146	318	315.58
57.05	55.52	1.566	1.099	147	458	460.18
58.76	57.23	1.589	1.122	147	516	514.78
62.09	60.56	1.633	1.146	149	710	708.52
67.05	65.52	1.696	1.169	149	832	828.40
68.13	66.59	1.709	1.169	150	890	880.88

Table 5.6: Fission cross-sections for ^{213,215}At* nuclei formed in ^{4,6}He-induced reactions at various excitation energies calculated using DCM, at common neck-length parameter ΔR.

E^*_{CN}	ΔR	^{213}At*		^{215}At*	
(MeV)	(fm)	($\hbar$)	(mb)	($\hbar$)	(mb)
19.0	0.771	136	5.9x10^{-4}	137	6.4x10^{-4}
25.0	0.810	139	0.102	142	0.168
40.0	0.905	143	39	145	45.6
50.0	0.980	145	124.2	146	154.8

the one used in scission and saddle point statistical models [28–32]. Further, the variation of ΔR with excitation energy E^*_{CN} is presented in Fig. 5.10. A linear increment is observed in ΔR with rise in E^*_{CN} values, which in turn used to predict the below barrier fission contributions (not measured so far), for At* isotopes formed in ^{3,4,6}He-induced reactions. The fission excitation functions are predicted by using the linear fit method for ΔR parameter as a function of E^*_{CN} (i.e. $\Delta R = mE^*_{CN} + c$, where m and c are slope and intercept, respectively) for all three studied nuclei as shown in Figure 5.10(a)-5.10(c), and given below:

$$\Delta R = 0.00425E^*_{CN} + 0.65734, \tag{5.3}$$

$$\Delta R = 0.00634E^*_{CN} + 0.65037, \tag{5.4}$$

$$\Delta R = 0.00802E^*_{CN} + 0.63633, \tag{5.5}$$

respectively, for ^{212}At*, ^{213}At* and ^{215}At* compound nuclei. The predicted $\sigma_{fission}$ at below barrier energies are listed in Table 5.7.

Further, the study is extended to another loosely bound projectile i.e. ^{8}He. In order to estimate the fission excitation functions for ^{8}He+^{209}Bi$\rightarrow^{217}$At* reaction, the slope (m) and intercept (c) values are extrapolated, which are obtained via linear fits of ΔR for ^{212}At*, ^{213}At* and ^{215}At* nuclei, see Fig. 5.11(a) and 5.11(b). Figures represent the plots of slope m and intercept c, and their extracted values as a function of A_{CN}. Using the extrapolated values of m and c, the new equation of ΔR as a function of E^*_{CN} for ^{8}He+^{209}Bi$\rightarrow^{217}$At* reaction reads as

$$\Delta R = 0.0097E^*_{CN} + 0.62229. \tag{5.6}$$

Table 5.7: The predicted fission excitation functions ($\sigma_{fission}$) at below barrier energy region ^{212,213,215}At* nuclei using extrapolated ΔR values. Besides this, the predicted fission contributions for ^{8}He+^{209}Bi$\rightarrow^{217}$At* reaction are also presented.

E^*_{CN} (MeV)	$E_{c.m.}$ (MeV)	T (MeV)	ΔR (fm)	ℓ_{max} ($\hbar$)	$\sigma^{DCM}_{fission}$ (mb)
		^{3}He+^{209}Bi$\rightarrow^{212}$At$^*\rightarrow$A$_1$+A$_2$			
19.0	12.23	0.920	0.738	137	3.36x10^{-4}
21.0	14.23	0.966	0.747	140	6.3x10^{-3}
23.0	16.23	1.010	0.755	140	8.0x10^{-3}
25.0	18.23	1.052	0.764	140	2.8x10^{-2}
25.89	19.12	1.070	0.767	141	5.12x10^{-2}
		^{4}He+^{209}Bi$\rightarrow^{213}$At$^*\rightarrow$A$_1$+A$_2$			
19.0	27.14	0.917	0.771	136	5.9x10^{-4}
21.0	29.14	0.963	0.784	138	8.24x10^{-3}
23.0	31.14	1.007	0.796	139	2.86x10^{-2}
		^{6}He+^{209}Bi$\rightarrow^{215}$At$^*\rightarrow$A$_1$+A$_2$			
19.0	17.47	0.913	0.789	135	6.36x10^{-4}
21.0	19.47	0.959	0.805	139	2.04x10^{-2}
23.0	21.47	1.002	0.821	140	1.72x10^{-1}
25.0	23.47	1.044	0.837	142	1.24
		^{8}He+^{209}Bi$\rightarrow^{217}$At$^*\rightarrow$A$_1$+A$_2$			
19.0	9.28	0.909	0.807	135	6.86x10^{-4}
21.0	11.28	0.954	0.826	138	2.24x10^{-2}
23.0	13.28	0.998	0.845	141	0.38
25.0	15.28	1.039	0.865	141	1.58
27.15	17.43	1.082	0.886	143	10.2
31.02	21.30	1.155	0.923	143	42.8
31.90	22.18	1.171	0.932	144	65.8
33.38	23.66	1.198	0.946	144	100
38.91	29.19	1.291	0.999	145	274
39.99	30.27	1.309	1.010	145	316
47.39	37.67	1.423	1.082	147	618
50.04	40.32	1.462	1.108	147	702
57.05	47.33	1.559	1.176	148	1316
58.76	49.04	1.582	1.192	149	1730
62.09	52.37	1.626	1.225	150	1980
67.05	57.33	1.688	1.273	151	1894
68.13	58.41	1.702	1.283	151	1778

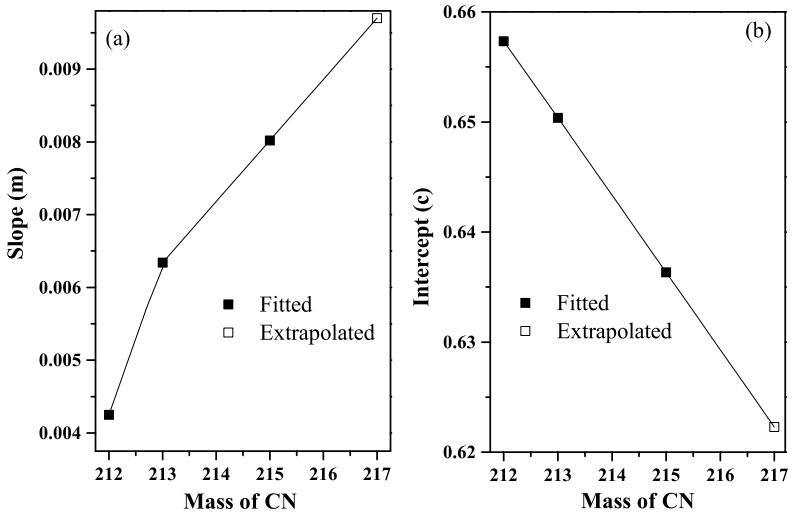

Figure 5.11: Variation of (a) Slope (m) and (b) intercept (c) with mass of CN for linear fit of ΔR as a function of excitation energy. Filled and open squares are, respectively, fitted and extrapolated values.

Utilizing this equation the values of ΔR are obtained at different E^*_{CN}, and used in turn to calculate the fission excitation functions for ^{8}He-induced reaction, and listed in Table 5.7.

Finally, the comparison of fission excitation functions of all considered reactions at below as well as above barrier energies is shown in Fig. 5.12. The inset of figure depict the broad view of fission contributions at sub-barrier region. Note that the excitation functions are calculated for the most energetic fission fragments i.e. A_2=72-92, 73-92, 76-92 and 78-93 (plus complementary fragments) respectively for ^{212}At*, ^{213}At*, ^{215}At* and ^{217}At* compound nuclei (see Fig. 5.14 and 5.15). The comparison of fission cross-sections for all He-induced reactions indicate that $\sigma_{fission}$ increases as a function of E^*_{CN}, and also with the increase in neutron number of projectile. This signify that the neutron number of the projectile and/or CN strongly influence the fission contributions. The similar trend is observed at below as well as above barrier region. However, the difference between fission cross-sections of 'At' isotopes is large at above barrier energies in comparison to below barrier region. The calculated results show nice agreement with experimental measurements [21, 26] available at above barrier energies for ^{3}He, ^{4}He and ^{6}He induced reactions. It will be of future interest to validate the below barrier predictions for A_{CN}=212,213,215 isotopes of At* and overall predictions for ^{217}At* nucleus formed in ^{8}He-induced reactions.

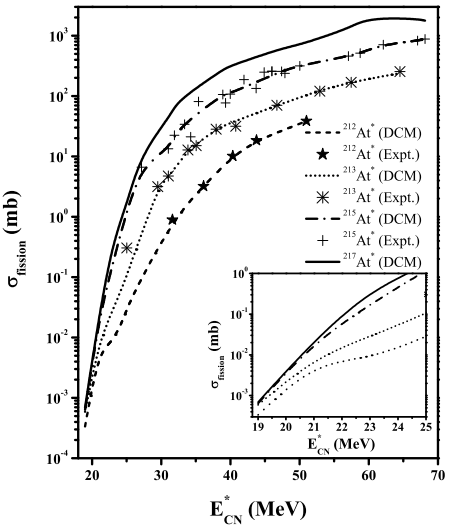

Figure 5.12: A comparison of fission excitation functions for $^{212-217}$At* nuclei at energies across the barrier, and compared with available fission data [21, 26]. Inset of figure show the broad view of below barrier fission cross-sections for all reactions.

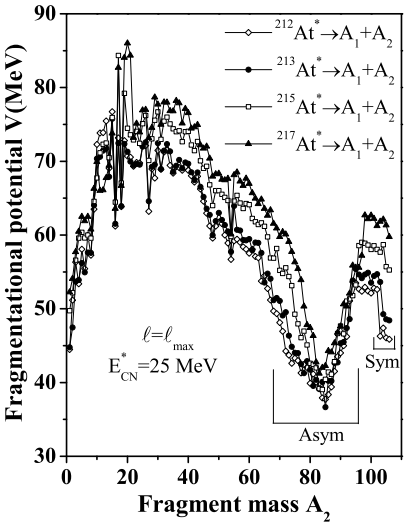

Figure 5.13: Variation of fragmentation potential V(A_2) at common excitation energy E^*_{CN}=25 MeV for At isotopes with mass number A_{CN}=212, 213, 215 and 217.

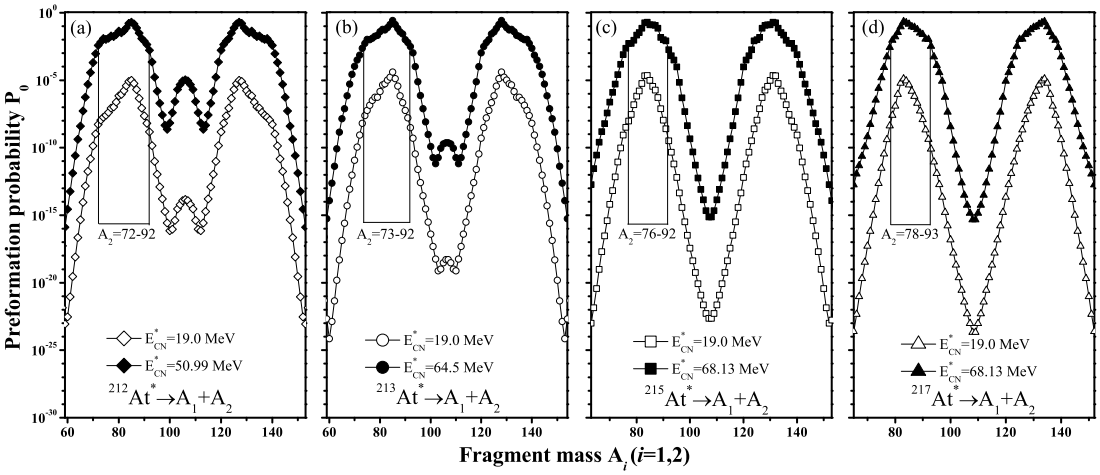

Figure 5.14: Preformation mass yield $P_0(A_i;\ i{=}1{,}2)$ for (a)^{212}At*, (b)^{213}At*, (c)^{215}At* and (d)^{217}At* compound nuclei at extreme E^*_{CN} values.

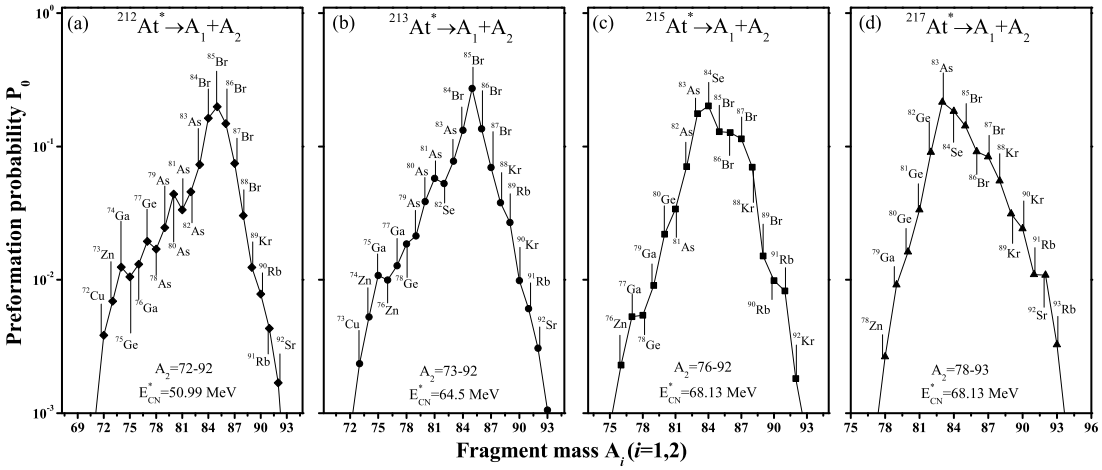

Figure 5.15: Identified most probable fission fragments are presented for (a)^{212}At*, (b)^{213}At*, (c)^{215}At* and (d)^{217}At* compound nuclei.

5.3.2 Fission fragment mass distributions of At* isotopes

In order to visualize the decay path of ^{212,213,215,217}At* isotopes, Fig. 5.13 illustrates the fragmentation potential V(A$_2$) at common excitation energy E^*_{CN}=25 MeV. It is noticed from figure that the structure of fragmentation potential is almost similar for the chosen At* isotopes, however its magnitude increases with the increase in mass number of CN. For each case, deep valley is observed at asymmetric fission (Asym) region, as marked in Fig. 5.13. Beside this, a small dip is seen around symmetric fission (Sym) window, which is relatively prominent for lighter CN as compared to heavier one.

Furthermore, the fission decay path of He-induced reactions is explored in terms of fission fragment mass distributions. Figs. 5.14(a)-5.14(d) present the preformation probability P_0(A$_i$) for ^{212,213,215,217}At* nuclei at extreme excitation energies E^*_{CN}. The fission fragment mass distributions gets modified with the addition of neutrons in CN. Although, it is clearly evident from figure that asymmetric fission forms the dominant decay mode for all At* isotopes studied at extreme compound nucleus excitation energies. A small hump around symmetric fragments with very small preformation probability is observed for two lighter mass systems i.e. ^{212}At* and ^{213}At*, which disappears for compound nuclei with more number of neutrons. The asymmetric fission fragments contributing the fission excitation functions, are marked in figure for each At compound nucleus. The individual identification of each contributing light asymmetric fission fragments (A$_2$) is made in Figs. 5.15(a)-5.15(d). It may be noted that the emergence of fission fragments remain same at

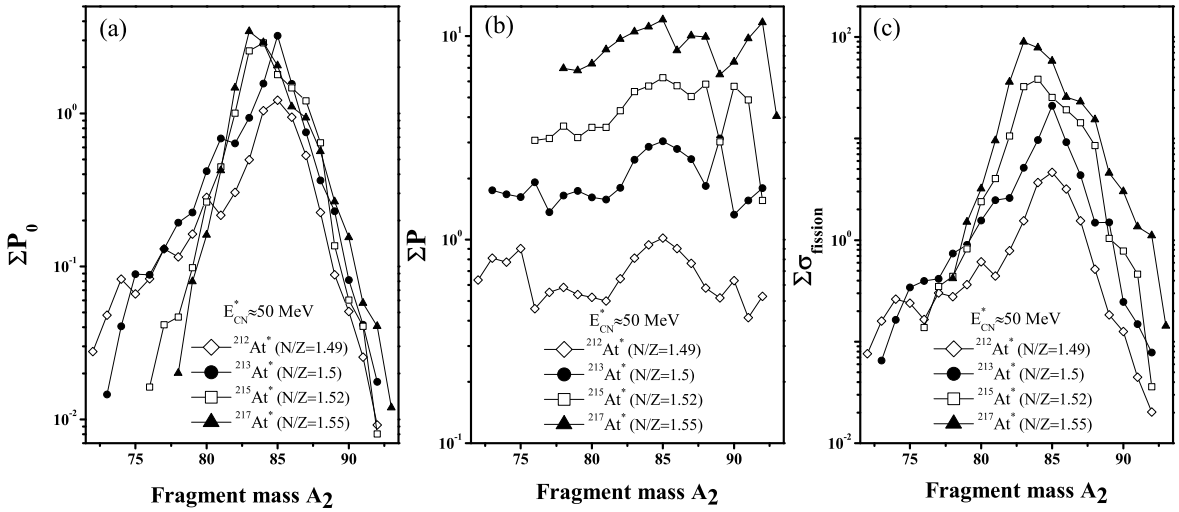

Figure 5.16: (a) ℓ-summed P_0 (b) ℓ-summed P and (c) ℓ-summed $\sigma_{fission}$ as a function of most probable light fission fragments A_2 at excitation energy E^*_{CN}=50 MeV.

all studied excitation energies.

5.3.3 N/Z dependence of various fission observables

This section is intend to examine the role of N/Z ratio on various nuclear observables used in DCM approach. Figs. 5.16(a)-5.16(c) illustrate behaviour of ℓ-summed preformation probability P_0, barrier tunneling P, and fission excitation functions $\sigma_{fission}$, with summation upto ℓ_{max} value, as a function of asymmetric fission fragments (A_2) for ^{212,213,215,217}At* nuclei. The calculated results are plotted at common excitation energy E^*_{CN}≈50 MeV. One can see from figure that the magnitude of preformation probability (P_0) of fission fragments is slightly different for different At isotopes. However, significant influence of N/Z ratio is seen on barrier penetrability P. The barrier penetrability of fission fragments increases with increment in the neutron number of CN. This can also relate with Fig. 5.9, where nuclear reaction with larger neutrons show lower barrier, and hence larger tunneling probabilities. Thus, ΣP has larger magnitude for nuclear systems with large N/Z ratio. Further, Fig. 5.16 shows the combine effect of P_0 and P in terms of fission excitation functions $\sigma_{fission}$. Figure illustrates that fission excitation functions follow the behavior of P_0, which suggests that structure effects are controlled via preformation factor P_0 and barrier tunneling probability P contributes towards the magnitude of cross-sections. Fig-

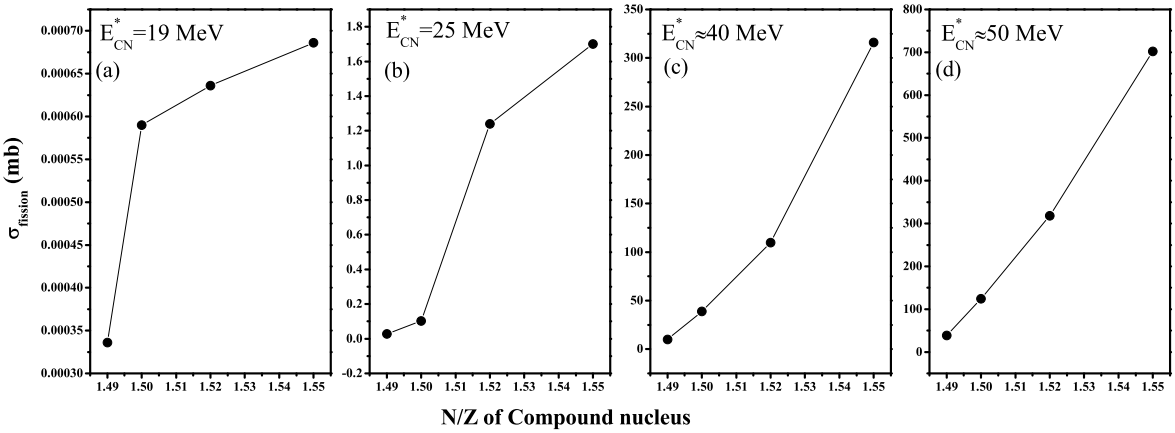

Figure 5.17: Variation of fission excitation functions with N/Z ratio of compound nucleus for (a)E^*_{CN}=19 MeV, (b)E^*_{CN}=25 MeV, (c)E^*_{CN}=40 MeV and (d)E^*_{CN}=50 MeV.

ure shows that fission cross-sections are higher for nuclei having large N/Z ratio. The total $\sigma_{fission}$ is plotted in Figs. 5.17(a)-5.17(d) as a function of N/Z of CN at various excitation energies E^*_{CN}≈19-50. Variation of $\sigma_{fission}$ show an increment with increase in N/Z ratio at each excitation energy E^*_{CN}. It represents that the fission cross-sections are larger for heavier nuclear isotopes, at below as well as above barrier energies.

Finally, Fig. 5.18(a) and 5.18(b) show the N/Z ratio of most probable light (A_2) and heavy (A_1) asymmetric fission fragments observed in the decay of ^{212,213,215,217}At* compound nuclei, as a function of "N/Z ratio" of compound nuclei. Most energetic fission fragments are also mentioned in the figure. Interestingly, for each case, the neutron number of most probable light fission fragments (A_2) is a magic number i.e. N=50. However, the atomic and neutron number of heavy asymmetric fission fragments lie in the vicinity of magic shell closures Z = 50 and N = 82, which manifests the impact of shell effects in the fission process.

5.4 Summary

In this chapter, the decay analysis of hot and rotating Ge and At isotopes formed in tightly and loosely bound He-induced reactions are investigated. First, the decay of ^{68}Ge* and ^{70}Ge* nuclear systems formed via tightly bound '^{4}He' and loosely bound '^{6}He' projectiles at various $E_{c.m.}$ is investigated. The DCM obtained results find good agree-

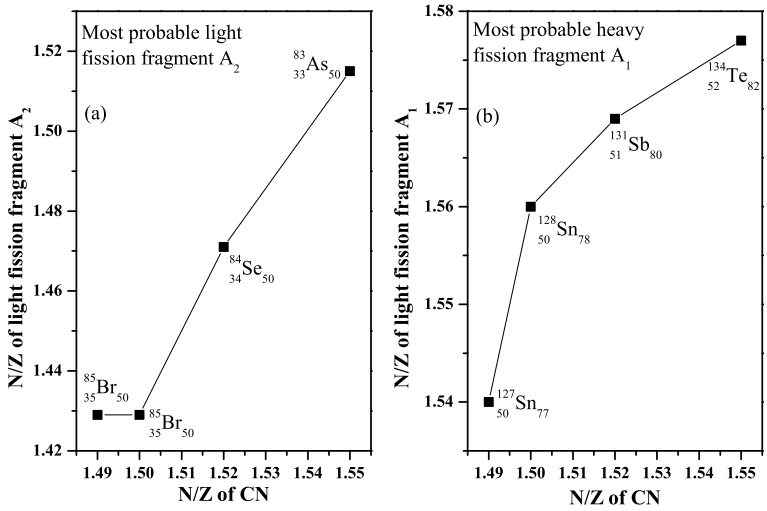

Figure 5.18: Variation of N/Z ratio of (a) light fission fragments and (b) heavy fission fragments with N/Z ratio of compound nucleus.

ment with experimental measurements for all the decay channels of ^{68}Ge* nucleus. The p- and n-emissions, which are dominant decay modes of ^{68}Ge* nucleus, show different barrier characteristics with respect to angular momentum (ℓ). Also, the E$_{c.m.}$-dependence and ℓ-dependence of fragmentation potential, preformation probability and barrier penetrability are duly addressed. Moreover, the fission contribution for the decay of ^{68}Ge* has been predicted, which comes out to be negligibly small due to lighter mass of compound system. Further, the excitation functions of various evaporation residues (ERs) $(2n)^{68}$Ge, $(np)^{68}$Ga, $(2np)^{67}$Ga and $(n\alpha)^{65}$Zn for the decay of ^{70}Ge* system are estimated and found that the σ_{ER} for (nα)^{65}Zn and $(2np)^{67}$Ga channel deviates from the experimental data. This deviation suggests the breakup of ^{6}He projectile (i.e. ^{6}He$\rightarrow 2n+^4$He) and transfer of $2n$ and ^{4}He leads to the formation of ^{66}Zn* and ^{68}Ge* nuclei. The breakup+transfer cross-sections are calculated by applying appropriate energy corrections. The total sum of fusion and breakup+transfer excitation functions represent good agreement with experimentally measured fusion data. Further, to understand the influence of the halo structure of ^{6}He, a comparative study of tightly bound '^{4}He' and loosely bound '^{6}He' projectile induced reactions has been carried out. A lower Coulomb barrier and smaller binding energy of loosely bound nucleus in turn influences the fusion cross-sections and related reaction mechanisms. Because of the loosely bound nature of ^{6}He nucleus, sub-barrier enhancement and above-barrier suppression are observed in the fusion cross-sections of ^{6}He+^{64}Zn

reaction.

After investigating the decay of lighter compound nuclei, the fission dynamics of ^{212,213,215,217}At* isotopes formed in tightly and loosely bound projectile induced reactions i.e. ^{3,4,6,8}He+^{209}Bi is investigated at excitation energies (E^{*}_{CN}) across the Coulomb barrier. Within DCM, the experimental fission excitation functions are addressed using ΔR parameter at above barrier region. The fission decay analysis is extended further at below barrier energies for ^{212,213,215}At* nuclei using linear fit equation of ΔR as a function of E^{*}_{CN}. Using the systematics of ^{212,213,215}At* isotopes, the fission contributions are predicted for another loosely bound and neutron-rich projectile induced reaction i.e. ^{8}He+^{209}Bi$\rightarrow^{217}$At* at E^{*}_{CN} across the barrier. An experimental verification is called for the fission contributions of ^{212,213,215}At* isotopes at below barrier region, and for ^{8}He+^{209}Bi across the Coulomb barrier. The fission excitation functions are observed to be sensitive towards the neutron number of projectile nucleus, which show an increment with increase in neutron number. Next, the fission fragment mass distributions of At isotopes are analyzed in terms of fragmentation potential and preformation probability yield. The mass distribution of fission fragments gets modified with the addition of neutrons in the highest isotope chosen for analysis. Interestingly, all At isotopes decay via asymmetric fission mode, irrespective of energy and angular momentum effects. Furthermore, the most energetic fission fragments are identified for each case, which lie in the neighbourhood of magic shell closures of Z or N=50 and N=82. It is emphasised that in isotopic analysis, the structure of contributing fission fragments is controlled via preformation factor and the magnitude of fusion cross-sections is influenced largely by the barrier tunneling probability.

The investigation of light particle, heavy ion and loosely bound projectile induced reactions (covered in this and previous chapters), depicts various dynamical and structural aspects of fission dynamics. This study is carried forward in the next chapter for the detailed analysis of fine structure effects in the fission fragment mass distributions for a wide range of nuclei studied at near and above Coulomb barrier energies.

Bibliography

[1] L. F. Canto, P. R. S. Gomes, R. Donangelo and M. S. Hussein, Phys. Rep. **424**, 1 (2006).

[2] N. Keeley, R. Raabe, N. Alamanos and J. L. Sidac, Prog. Part. Nucl. Phys. **59**, 579 (2007).

[3] N. Keeley, N. Alamanos, K. W. Kemper and K. Rusek, Prog. Part. Nucl. Phys. **63**, 396 (2009).

[4] W. Loveland, A. M. Vinodkumar, R. Yanez, L. Yao, J. King, J. Lassen and A. Rojas, Eur. Phys. J. A **54**, 140 (2018).

[5] A. Kaur and M. K. Sharma, Nucl. Phys. A **969**, 30 (2018).

[6] G. Kaur, K. Sandhu and M. K. Sharma, Phys. Rev. C **94**, 014615 (2016).

[7] N. Grover, G. Kaur and M. K. Sharma, Phys. Rev. C **93**, 014603 (2016).

[8] A. Kaur and M. K. Sharma, Nucl. Phys. A **957**, 274 (2017).

[9] G. Sawhney and M. K. Sharma, Eur. Phys. J. A **48**, 57 (2012).

[10] G. Kaur and M. K. Sharma, Nucl. Phys. A **884**, 36 (2012).

[11] A. Ornelas *et al.*, Phys. Rev. C **94**, 055807 (2016).

[12] Gy. Gyürky, P. Mohr, Zs. Fülöp, Z. Halász, G. G. Kiss, T. Szücs and E. Somorjai, Phys. Rev. C **86**, 041601(R) (2012).

[13] V. Scuderi *et al.*, Phys. Rev. C **84**, 064604 (2011).

[14] A. Kaur, K. Sandhu and M. K. Sharma, Commun. Theor. Phys. **70**, 565 (2018).

[15] M. Kaur and M. K. Sharma, Eur. Phys. J. A **50**, 61 (2014).

[16] K. Hagino, A. Vitturi, C. H. Dasso and S. M. Lenzi, Phys. Rev. C **61**, 037602 (2000).

[17] J. J. Kolata *et al.*, Phys. Rev. Lett. **81**, 4580 (1998).

[18] P. A. DeYoung *et al.*, Phys. Rev. C **58**, 3442 (1998).

[19] A. S. Fomichev, I. David, Z. Dlouhy, S. M. Lukyanov, Yu. Ts. Oganessian, Yu. E. Penionzkevich, V. P. Perelygin, N. K. Skobelev, O. B. Tarasov and R. Wolski, Z. Phys. A **351**, 129 (1995).

[20] J. J. Kolata *et al.*, Phys. Rev. C **57**, R6 (1998).

[21] Yu. E. Penionzhkevich, Yu. A. Muzychka, S. M. Lukyanov, R. Kalpakchieva, N. K. Skobelev, V. P. Perelygin and Z. Dlouhy, Eur. Phys. J. A **13**, 123 (2002).

[22] E. F. Aguilera *et al.*, Phys. Rev. Lett. **84**, 5058 (2000).

[23] E. F. Aguilera *et al.*, Phys. Rev. C **63**, 061603(R) (2001).

[24] J. P. Bychowski *et al.*, Phys. Lett. B **596**, 26 (2004).

[25] P. A. DeYoung *et al.*, Phys. Rev. C **71**, 051601(R) (2005).

[26] F. D. Becchetti *et al.*, Phys. Rev. C **28**, 1217 (1983).

[27] A. Kaur, P. Kaushal, Hemdeep and R. K. Gupta, Nucl. Phys. A **969**, 184 (2018).

[28] T. Matsuse, C. Beck, R. Nouicer and D. Mahboub, Phys. Rev. C **55**, 1380 (1997).

[29] B. D. Wilkins, E. P. Steinberg and R. R. Chasman, Phys. Rev. C **14**, 1832 (1976).

[30] S. J. Sanders, Phys. Rev. C **40**, 2091 (1989).

[31] S. J. Sanders *et al.*, Phys. Rev. C **44**, 2676 (1991).

[32] S. J. Sanders, A. Szanto de Toledo and C. Beck, Phys. Rep. **311**, 487 (1999).

Chapter 6

Fine structure effect in fission fragment mass distributions

In previous chapters, extensive analysis of decay dynamics is studied with particular focus on fusion-fission channel. The investigations are carried out for light and heavy mass compound nuclei formed via variety of projectiles over a wide range of incident energies spread across the Coulomb barrier. In addition to light particle induced fission, the compound nucleus (CN) and non-compound nucleus (nCN) channels were investigated for the case of heavy ion induced reactions. This chapter will focus on the interesting aspect of fission fragment mass distributions "termed as fine structure effect", and explored in terms of energy and mass of CN. It is indeed highly desirable to investigate the fine structure among the contributing fission fragments, which inturn may provide possibility of some exotic nuclei far from stability line. The fission fragment mass distributions are utilized as a probe to study the mass division of nuclear systems [1–3]. The structural effects are expected to reflect in the fragmentation potential due to the competition between distinct fission modes, i.e. symmetric (Sym) and asymmetric (Asym) fission. For this purpose, the fission dynamics is explored for various pre-actinide and actinide nuclei having mass A_{CN}=185-235 and Z_{CN}=83-92. ^{19}F nucleus is used as a common projectile for the chosen set of reactions studied in this chapter. The calculations are carried out at near and above barrier energies by employing the dynamical cluster-decay model (DCM). The outcomes from these calculations are presented in the coming sections and published in Refs. [4,5]. A brief introduction of this work is given below.

6.1 Introduction

This chapter confers the understanding of the fine structure effects in the mass distributions for a wide range of energies and fissioning nuclei (from proton-rich to neutron-rich systems). The investigation of fragment mass distribution as a function of center-of-mass energy ($E_{c.m.}$) and compound nucleus mass (A_{CN}) is carried out for ^{19}F-induced fission of several pre-actinide (Bi, Po, At, Rn and Ra) and two actinide (Pa and U) nuclei within the framework of DCM [6–14]. In a previous work [6,7], the fission decay of Fr pre-actinide nuclei produced in ^{19}F-induced reactions was analyzed using DCM, thus not included here. For the considered nuclei, the fission excitation functions are computed. The calculations are carried out by including β_2-quadruple deformation effects of decaying fragments with optimum orientations ($\theta_i^{opt.}$).

First, the section 6.2 of this chapter describes the energy dependence of fine structure effects that comes in picture via the fragmentation potential of the fissioning region, and is analysed for ^{201}Bi*, ^{206}Po*, ^{211}At* ^{212}Rn*, ^{216}Ra*, ^{227}Pa* and ^{228}U* compound nuclei formed in ^{19}F+^{182}W, ^{19}F+^{187}Re, ^{19}F+^{192}Os, ^{19}F+^{193}Ir, ^{19}F+^{197}Au, ^{19}F+^{208}Pb and ^{19}F+^{209}Bi reactions respectively. Further, the fission excitation functions are calculated, and compared with the experimental data of Refs. [15–17]. In section 6.3, the influence of shell corrections and deformations in the mass distributions is investigated. To identify the transitional mass region where symmetric to asymmetric fission transition takes place, the mass/isospin dependence of mass distributions of pre-actinide and actinide nuclei, is studied in section 6.4. Moreover, the most probable fission decay fragments are also identified.

6.2 Energy dependence of fission fragment mass distribution and fission cross-sections

The fragmentation potential $V_R(\eta, T)$ is an essential ingredient of the DCM-calculations, and its structure provides the information about energetically favoured decay modes of compound nuclei. Figs. 6.1(a)-6.1(c) present the fragmentation potential for ^{201}Bi*, ^{212}Rn* and ^{228}U* compound nuclei produced in ^{19}F-induced reactions at common $E_{c.m.}\sim$80 MeV. The first look of fragmentation potential suggests relatively more struc-

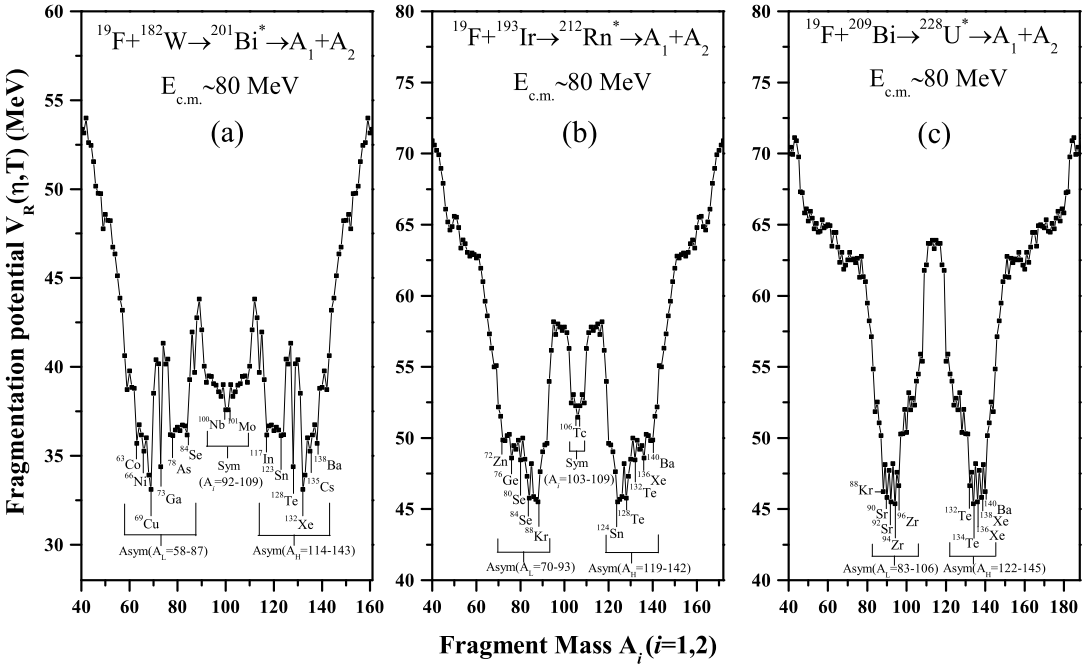

Figure 6.1: DCM-calculated fragmentation potential $V_R(\eta, T)$ for the compound nuclei ^{201}Bi*, ^{212}Rn* and ^{228}U* formed in ^{19}F+^{182}W, ^{19}F+^{193}Ir and ^{19}F+^{209}Bi reactions respectively, at $E_{c.m.}$~80 MeV.

tural effects in the lighter mass nucleus than the heavier one. The asymmetric fission (Asym) decay mode for considered nuclei is represented by the deep valleys corresponding to the light (A_L) and heavy (A_H) asymmetric fission fragments, as marked in Fig. 6.1. Very small probability of symmetric fission (Sym) channel is observed for ^{201}Bi* and ^{212}Rn* nuclei, where ^{228}U* nucleus decays via pure asymmetric fission channel. Note that all the calculated results are presented for maximum angular momentum values (ℓ_{max}), as fission decay is considered here. The energetically favoured fission fragments are identified and marked in the Fig. 6.1.

The minimum value of fragmentation potential corresponds to the highly preformed fragments, and hence preformation probability P_0 follow an inverse trend (see Fig. 6.2). To look for the fine-structure features in the fission region and their energy dependence, the behaviour of fission fragment mass distributions in terms of preformation probability P_0 of decaying fragments is further investigated. Figs. 6.2(a)-6.2(g) demonstrate the preformation probability P_0 of all considered pre-actinide (^{201}Bi*, ^{206}Po*, ^{211}At*, ^{212}Rn* and ^{216}Ra*) and actinide (^{227}Pa* and ^{228}U*) nuclei at extreme centre-of-mass energies.

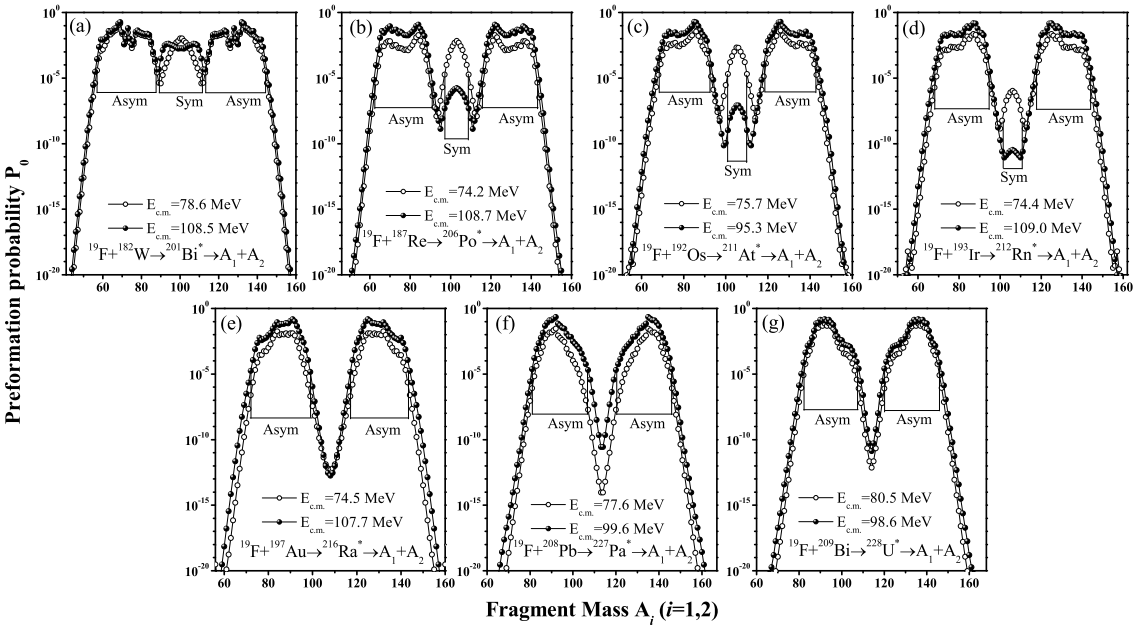

Figure 6.2: Preformation probability $P_0(\mathrm{A}_i)$ for the pre-actinide (a-d) and actinide (e-g) nuclei generated in ^{19}F-induced reactions at extreme $E_{c.m.}$ values.

The distinct valleys in the fission region of fragmentation potential (see Fig. 6.1) lead to corresponding peaks in the preformation profile. Therefore, some of the pre-actinide nuclei (^{201}Bi* to ^{212}Rn*) exhibit the triple humped mass distribution, which signify the presence of multi-mode fission i.e. symmetric and asymmetric. This suggests that lighter mass nuclei exhibit more structural effects than the heavier one. It can be depicted from preformation plots that the asymmetric channel is predominant for all considered nuclei at extreme energies. Same result was observed for ^{213,217}Fr* compound nuclei, presented in Ref. [6]. The shape of distinct peaks in the preformation profile give rise to the possibilities of fine-structure effects in the fission region. These structural effects and competition between distinct fission modes can be studied by investigating the variation of symmetric to asymmetric fission peaks ($\mathrm{P}_{Sym}/\mathrm{P}_{Asym}$) with $E_{c.m.}$ for nuclei showing triple humped mass distributions. Figs. 6.3(a) and 6.3(c) present the energy-dependent $\mathrm{P}_{Sym}/\mathrm{P}_{Asym}$ ratios for ^{201}Bi* and ^{206}Po* nuclei, whereas other pre-actinide and actinide compound nuclei decay mainly via asymmetric fission and hence such analysis is not relevant for them. These peak ratios are calculated for symmetric and asymmetric fission fragments as marked in Fig. 6.2. The behaviour of calculated peak ratios is similar, i.e broadly decreases with increase in $E_{c.m.}$ for both nuclei. This indicates that the contribution of symmetric

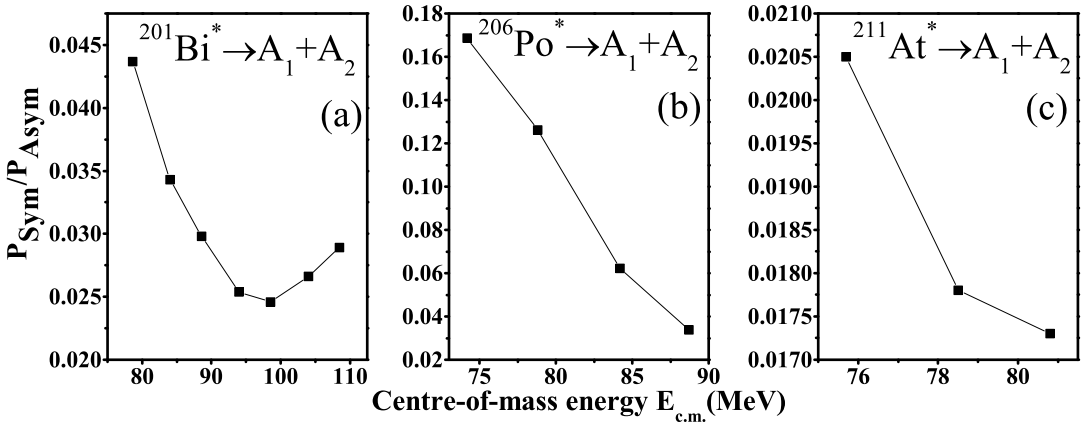

Figure 6.3: Variation of P_{Sym}/P_{Asym} with $E_{c.m.}$ for (a) ^{201}Bi*, (b) ^{206}Po* and (c) ^{211}At* compound nuclei.

component is relatively more at smaller energies. However, the asymmetric fission forms the predominant decay channel at considered energy range for all the pre-actinide and actinide nuclei reported in Fig. 6.2. The most energetic peaks of asymmetric fission with maximum preformation probability P_0 are seen at A_L:A_H= ^{69}Cu:^{132}Xe, ^{84}Se:^{122}Sn, ^{85}Br:^{126}Sn, ^{87}Kr:^{125}Sn, ^{91}Sr:^{125}Sn, ^{92}Sr:^{135}I and ^{92}Sr:^{136}Xe, respectively, for ^{201}Bi*, ^{206}Po*, ^{211}At*, ^{212}Rn*, ^{216}Ra*, ^{227}Pa* and ^{228}U* compound nuclei, where A_L and A_H are, respectively, the light and heavy asymmetric fission fragments. Interestingly, asymmetric fission (Asym) peaks arise around mass asymmetry $\eta_{Asym}\sim$0.2 for most of the cases. The predicted most probable heavy asymmetric A_H fragments are found to lie around magic shell closure of Z=50.

Further, the fission cross-sections of considered pre-actinide and actinide nuclei are calculated by fixing the ΔR parameter. Table 6.1 presents the DCM-obtained excitation functions for the energetically favoured fission fragments marked in Fig. 6.2. The calculated $\sigma_{fission}$ show good agreement with the data given in Refs. [15–17], except at few highest energies $E_{c.m.}\geq$100 MeV. Therefore, one may anticipate that the formation of equilibrated CN is hindered at higher incident energies due to possible contribution of non-compound nucleus (nCN) process. The presence of nCN process, such as quasi fission, is also observed experimentally in reaction involving ^{19}F as a projectile see Ref. [18]. Thus,

Table 6.1: The calculated fission excitation functions of several pre-actinide and actinide nuclei at various $E_{c.m.}$, and compared with the measured data [15–17]. The optimized values of ΔR parameter with other calculated quantities are also presented in the table.

$E_{c.m.}$	E^*_{CN}	T	ΔR	ℓ_{max}	Fission cross-section $\sigma_{fission}$	
(MeV)	(MeV)	(MeV)	($\hbar$)	(fm)	DCM (mb)	Expt. (mb)
$^{19}F+^{182}W\rightarrow^{201}Bi^*\rightarrow A_1+A_2$						
78.6	50.3	1.523	0.958	127	9.38	9.6±1.0
84.0	55.7	1.602	1.023	128	48.4	49.6±5.0
88.6	60.2	1.664	1.081	129	111.0	111.6±11.2
94.0	65.7	1.738	1.160	130	236.0	237.4±23.7
98.5	70.2	1.795	1.200	131	330.0	333.6±33.4
104.0	75.6	1.862	1.222	132	420.0	471.4±47.1
108.5	80.2	1.918	1.230	133	410.0	617.5±61.8
$^{19}F+^{187}Re\rightarrow^{206}Po^*\rightarrow A_1+A_2$						
74.2	49.7	1.496	0.829	135	0.46	0.46±0.05
78.8	54.2	1.561	0.888	137	10.04	10.2±1.0
84.2	59.7	1.637	0.975	138	54.0	54.0±5.4
88.7	64.2	1.697	1.050	139	130.0	130.2±13.0
94.2	69.7	1.767	1.130	140	264.0	261.3±26.1
98.7	74.2	1.822	1.169	142	404.0	403.3±40.3
104.2	79.7	1.888	1.185	143	478.0	538.9±53.9
108.7	84.2	1.940	1.186	144	474.0	653.9±65.4
$^{19}F+^{192}Os\rightarrow^{211}At^*\rightarrow A_1+A_2$						
75.7	49.32	1.472	0.828	140	1.058	1.09
78.5	52.10	1.512	0.868	140	6.32	6.36
80.8	54.42	1.545	0.897	140	13.18	13.16
83.2	56.82	1.578	0.933	141	33.0	33.16
86.4	60.02	1.621	0.978	142	68.8	68.62
89.2	62.82	1.658	1.018	143	113.6	113.86
95.3	68.92	1.736	1.107	144	248.0	248.78
$^{19}F+^{193}Ir\rightarrow^{212}Rn^*\rightarrow A_1+A_2$						
74.4	47.0	1.434	0.754	138	0.392	0.40±0.04
79.0	51.6	1.501	0.830	140	10.84	10.6±1.1
84.4	57.1	1.578	0.970	140	68.20	69.9±7.0
89.0	61.6	1.638	1.088	140	197.8	198.0±19.8
94.4	67.1	1.709	1.159	141	364.0	362.1±36.2
99.0	71.6	1.765	1.182	142	518.0	523.2±52.3
104.5	77.1	1.831	1.178	143	450.0	683.9±68.4
109.0	81.7	1.884	1.180	144	452.0	794.1±79.4

Table 6.2: Table 6.1 continued...

$E_{c.m.}$ (MeV)	E^*_{CN} (MeV)	T (MeV)	ΔR ($\hbar$)	ℓ_{max} (fm)	Fission cross-section $\sigma_{fission}$ DCM (mb)	Expt. (mb)
$^{19}F+^{197}Au \rightarrow ^{216}Ra^* \rightarrow A_1+A_2$						
74.5	37.9	1.277	0.754	134	0.366	0.369
78.3	41.7	1.339	0.831	134	9.12	9.117
81.8	45.2	1.393	0.963	134	64.2	63.89
85.6	48.9	1.449	1.070	134	176.8	177.70
89.3	52.7	1.502	1.133	135	320.0	324.28
92.9	56.3	1.552	1.161	136	460.0	460.18
96.7	60.1	1.603	1.170	136	470.0	601.88
100.4	63.8	1.651	1.167	137	446.0	720.66
104.0	67.4	1.696	1.175	137	460.0	828.40
107.7	71.1	1.742	1.180	138	494.0	926.70
$^{19}F+^{208}Pb \rightarrow ^{227}Pa^* \rightarrow A_1+A_2$						
77.6	27.48	1.064	0.964	122	1.53	1.55
78.6	28.48	1.083	0.975	122	3.66	3.61
80.6	30.48	1.119	0.993	124	13.38	13.24
83.6	33.48	1.172	1.075	124	115.6	116.6
90.0	39.48	1.277	1.174	126	390.0	404.4
99.6	49.48	1.521	1.180	128	390.0	825.6
$^{19}F+^{209}Bi \rightarrow ^{228}U^* \rightarrow A_1+A_2$						
80.5	31.4	1.134	0.943	123	6.22	6.3±0.6
82.2	33.1	1.163	0.958	124	16.34	16.8±1.1
83.4	34.3	1.184	0.982	124	33.2	34.0±2.0
85.1	36.0	1.212	1.016	125	74.8	75.0±5.0
86.2	37.1	1.231	1.040	125	105.8	108.0±6.0
87.5	38.4	1.252	1.080	125	156.6	159.0±9.0
91.4	42.3	1.313	1.150	126	318.0	318.0±30.0
95.1	46.0	1.368	1.170	126	386.0	399.0±20.0
98.6	49.5	1.418	1.176	127	428.0	551±30.0

the deviation of estimated fission excitation functions from the measured data [15–17] indicates the presence of quasi fission, as higher energies above the Coulomb barrier are more prone to the nCN content in agreement with the results presented in chapter 4.

6.3 Influence of "shell corrections" and "deformations" on the mass distributions

At low excitation energies, the microscopic shell effects impart significant role in fixing the suitable combination of decaying fragments. Although the present set of calculations are done at relatively higher energies (T≥1.5 MeV for most of the cases) and hence role of shell corrections are expected to be limited, which in turn mean that the fission dynamics may be influenced via some additional effects as well. In order to quantify such effects, initially the calculations are done with and without inclusion of shell corrections. Figs. 6.4(a)-6.4(d) show the preformation probability calculated by including and excluding the shell correction term (δU) in the potential for lighter and heavier mass nuclei i.e. for ^{201}Bi* and ^{228}U*, using spherical fragmentation only. The calculated results are plotted at T=0.5 MeV and 1.5 MeV for both compound nuclei. The fission mass division shifts from symmetric to asymmetric with the incorporation of δU term as shown in Fig. 6.4(a) and 6.4(b). It is known that a closed shell nucleus is more stable and occupies the minima position in fragmentation potential. Consequently, the preformation probability has maximum value for closed-shell fission fragments. This suggests that the shell corrections play significant job in the mass division of fissioning nuclei at lower temperature. While, at higher temperature T=1.5 MeV, see Fig. 6.4(c) and 6.4(d), the effect of microscopic energy (shell corrections) almost disappear and structural effects are significantly reduced. Hence, the symmetric mass distribution is observed for both cases at higher temperature.

Above results signify that there is another factor which is responsible for the evolution of structure in the fission region of mass distribution as observed in Figs. 6.1 and 6.2 for several compound nuclei. In order to resolve this aspect, the dependence of fragmentation potential (and preformation profile) on the deformations of decay fragments in binary fragmentation process, is analyzed. In Fig. 6.5, the specific role of deformations of fragments is explored for both ^{201}Bi* and ^{228}U* compound nuclei at T=1.5 MeV where shell effects significantly reduce, but structural effects are still present as shown in Fig. 6.2 for

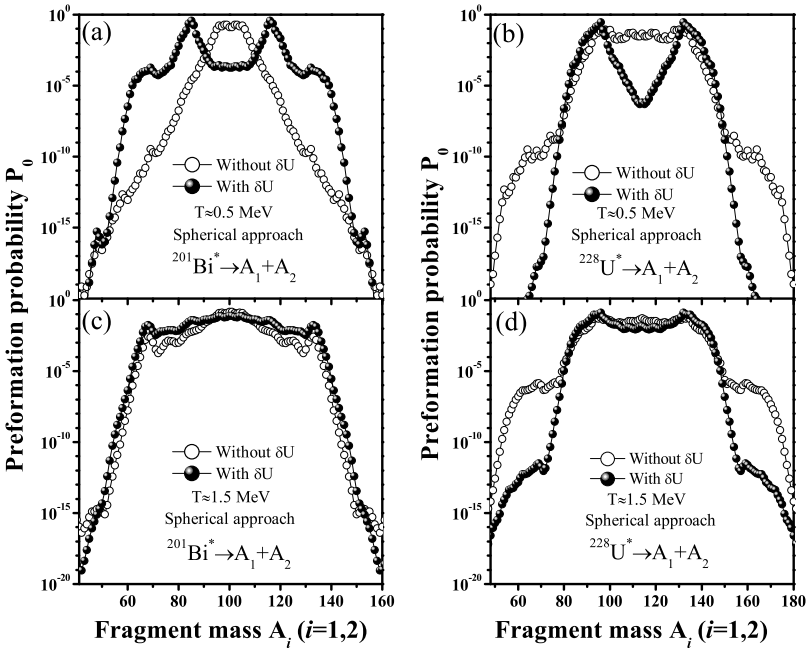

Figure 6.4: Preformation profile $P_0(\mathrm{A}_i)$ for fissioning ^{201}Bi* and ^{228}U* nuclei with and without the incorporation of δU term at temperature T=0.5 MeV and 1.5 MeV.

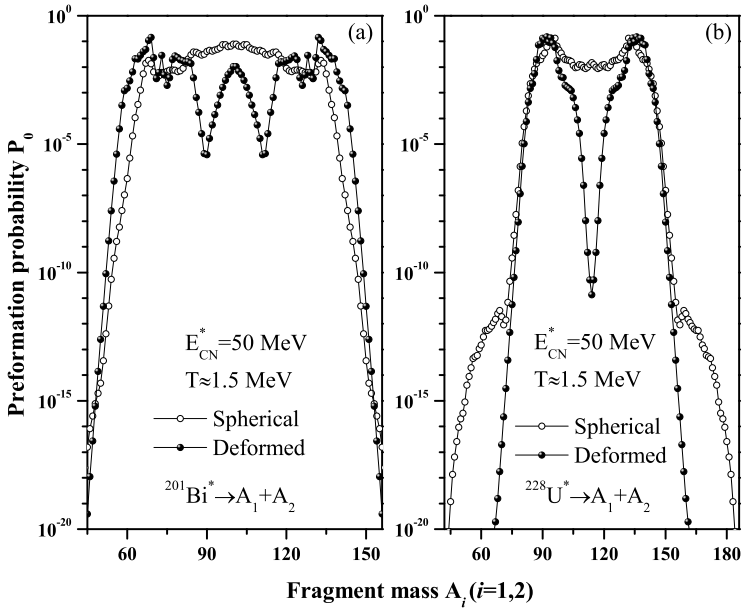

Figure 6.5: Preformation probability $P_0(\mathrm{A}_i)$ for (a) ^{201}Bi* and (b) ^{228}U* nuclei at T=1.5 MeV for spherical and deformed fragmentation.

various nuclei. It is noticed from figure that the structural effects in fissioning region enter via the inclusion of β_2-quadruple deformations for both pre-actinide (^{201}Bi*) and actinide (^{228}U*) nuclei. It is observed that the fragments on the peaks of preformation yield are spherical or near-spherical (with very small magnitude of β_2-deformation). Whereas, the fission fragments of the valleys are highly deformed. This indicates that the deformations of decaying fragments play crucial role in depicting the structural pattern in fissioning region, and hence on the overall governance of fission dynamics. This study is confined to β_2-deformations in the present analysis and it will be of future interest to see the corresponding effect of higher multipole deformations on the structural variation of fission fragments.

6.4 Mass dependence of fission fragment mass distributions

After studying the energy dependence of fragment mass distribution, fission cross-sections, and various factors effecting the fission dynamics, next the dependence of fragment mass distribution on mass of compound systems is explored, by studying the dynamics of a series of proton-rich to neutron-rich nuclei. The calculated results are presented in Figs. 6.6(a)-6.6(t) and 6.7(a)-6.7(h) for various pre-actinide and actinide nuclei from ^{185}Bi* to ^{235}U* produced in ^{19}F-induced reactions at common $E_{c.m.}$~80 MeV near the Coulomb barrier. The optimized value of ΔR at $E_{c.m.}$~80 MeV for different nuclei as tabulated in Table 6.1, is used to calculate the isotopic mass distributions. The main interest here is to identify the co-existence of both symmetric and asymmetric fission channels, and to identify the switching point where symmetric to asymmetric fission transition takes place. It is observed from figure that the lighter mass isotopes of considered nuclei show symmetric mass distribution. As the mass of compound nucleus A_{CN} increases, three peaked structure start appearing in the preformation profile, indicating the presence of two distinct modes of fission. However, for the further heavier isotopes, this three peaked mass structure gets converted to the two peaked mass distribution, which show the dominance of asymmetric fission. Broadly speaking, a transition from symmetric fission to asymmetric fission is observed as one goes from lighter to heavier mass isotope. The relevant details of transitional region and observed light and heavy asymmetric fission

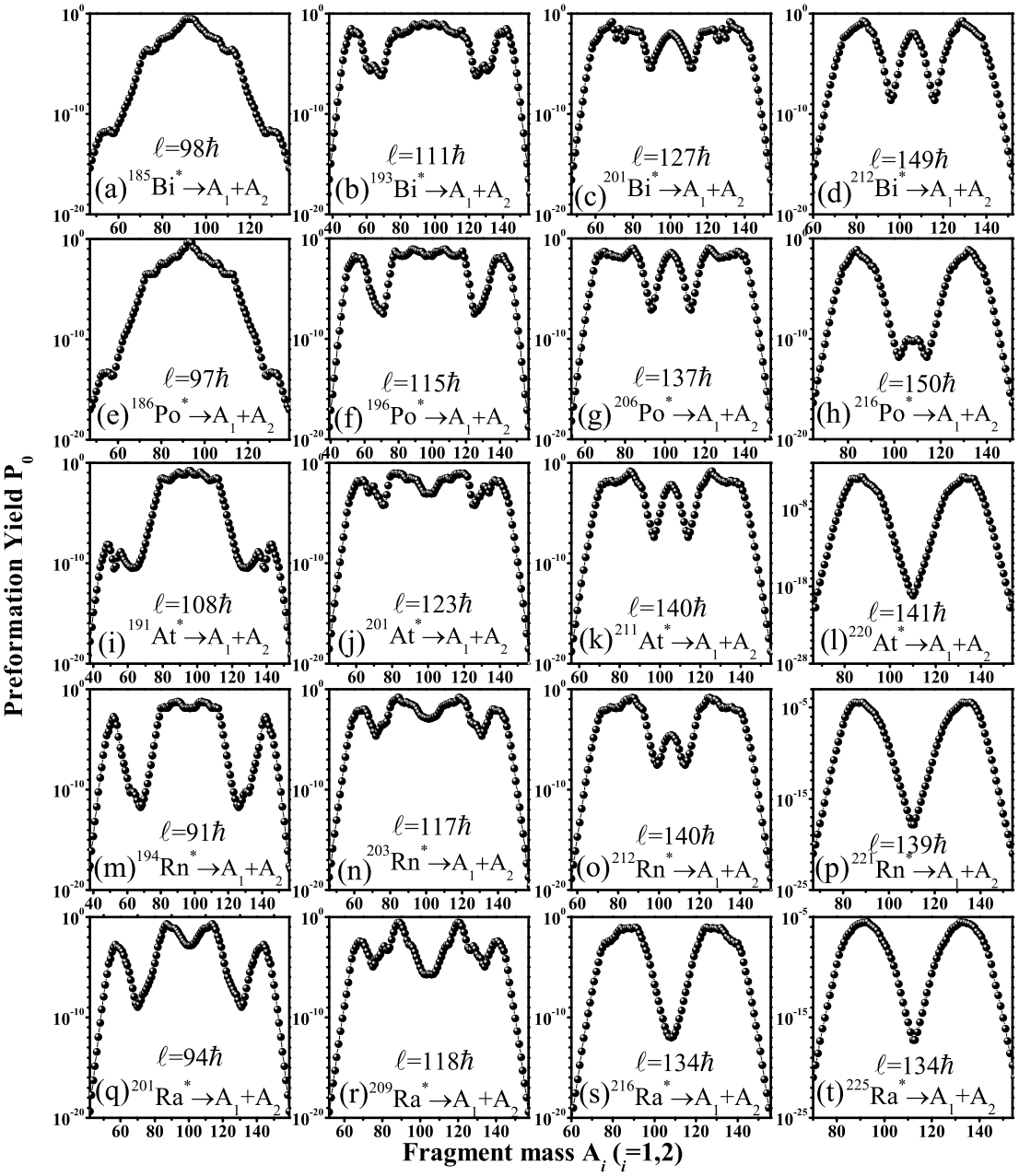

Figure 6.6: Preformation yield $P_0(\mathrm{A}_i)$ for various isotopes of Bi, Po, At, Rn and Ra pre-actinide nuclei at common $E_{c.m.}$∼80 MeV.

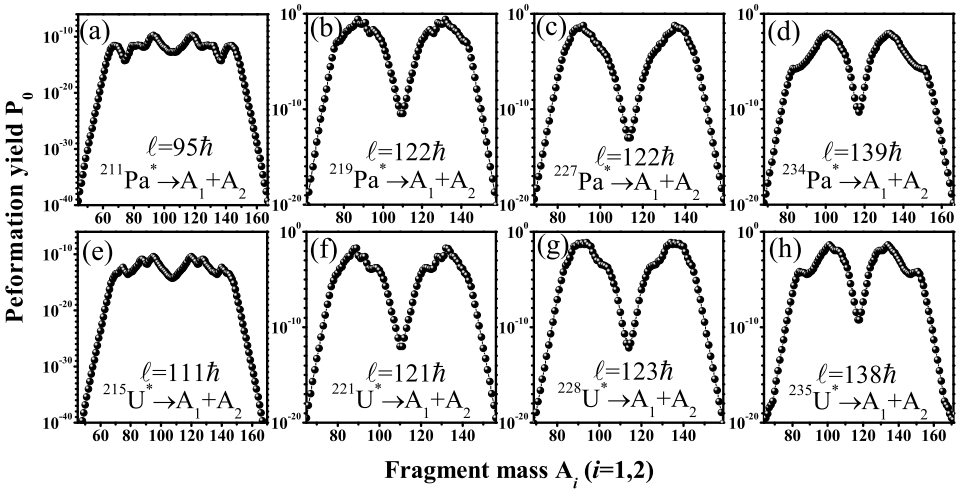

Figure 6.7: Same as figure 6.6 but for isotopes of Pa and U actinide nuclei.

fragments are discussed in Fig. 6.8 and Fig. 6.9. Note that the fragments observed at peaks of preformation profile are spherical or near spherical with very small magnitude of β_2-deformation. Whereas, the fragments present in the valleys of P_0 are highly deformed. It clearly indicates the significant role of deformations of decaying fragments in the fission dynamics as discussed earlier in Fig. 6.5.

The characteristics of fission decay are also analyzed in terms of symmetric (Sym) to asymmetric (Asym) peak ratios P_{Sym}/P_{Asym} as a function of compound nucleus mass A_{CN} as shown in Fig. 6.8. A transition from symmetric fission to asymmetric fission occurs for the pre-actinide region. Triple-humped mass distributions appear around the transitional region, demonstrating the comparable weightage for symmetric and asymmetric fission (see Fig. 6.6). This clearly signify the existence of fine structure features in the fission dynamics of pre-actinide nuclei. However, the asymmetric fission prevails in the case of heavier nuclei (i.e. Ra, Pa and U). The peak ratios are calculated for the wide mass region of pre-actinide nuclei and the results are presented in Fig. 6.8. It is observed from figure that the P_{Sym}/P_{Asym} decreases with increment in mass number of compound nucleus A_{CN}. This suggests that the fragment mass distribution exhibits a transition from symmetric to asymmetric fission with increase in compound nucleus mass. Interestingly, the N/Z ratio of A_{CN} around the transitional region is common for all studied cases, which is approximately equal to 1.4. The experimental verification of above mentioned

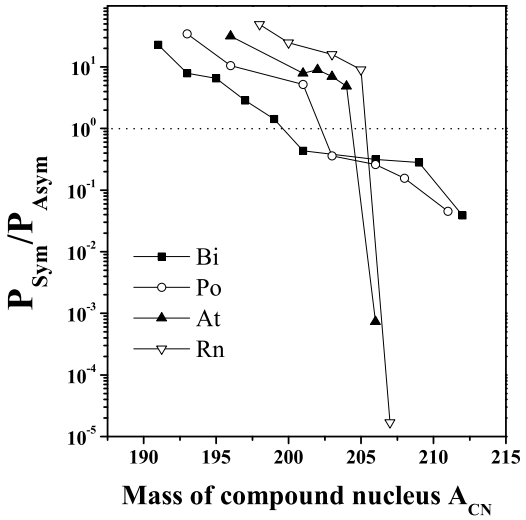

Figure 6.8: A plot of Symmetric to asymmetric fission peak ratio vs. compound nucleus mass A_{CN} for the isotopic mass region of Bi, Po, At and Rn nuclei.

results would be interesting.

The above calculated DCM results allow to identify the mass division of most energetic light (A_L) and heavy (A_H) asymmetric fission fragments for long isotopic chains. Figs. 6.9(a)-6.9(d) present the proton (Z) and neutron (N) number of most probable light and heavy fission fragments of asymmetric peaks observed in preformation profile of Figs. 6.6 and 6.7. Fig. 6.9(b) depicts that the heavy fission fragment is always observed near proton number Z=50 for pre-actinide region and Z=54 for actinide nuclei. Whereas, the N number varies over several units (increases with increase in mass number of CN). It is worth mentioning here that the observed heavy fission fragment A_H are spherical and corresponding light fission fragment are partially spherical with very small deformations. The above observations signify the relevance of deformation effects of binary decay fragments in the fission dynamics. However, it would be fascinating to explore the role of higher degree deformations in the fission dynamics of pre-actinide and actinide mass region, as a future assignment.

6.5 Summary

In this chapter, the fission fragment mass distributions are analyzed for the various pre-actinide and actinide nuclei (^{201}Bi*, ^{206}Po*, ^{211}At*, ^{212}Rn*, ^{216}Ra*, ^{227}Pa* and ^{228}U*)

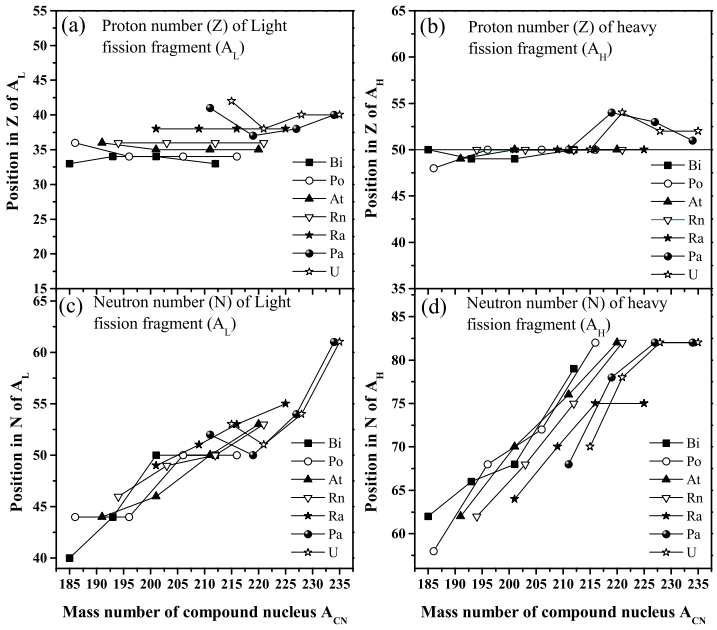

Figure 6.9: The position of most probable light (A_L) and heavy (A_H) asymmetric fission fragments in proton (Z) and neutron (N) numbers as a function of A_{CN}.

produced via heavy-ion (^{19}F) induced reactions. The fission excitation functions are calculated within collective clusterization approach, and are in accordance with the measured data except at few highest energies. The suppression of fission excitation functions indicates the presence of non-compound nucleus (nCN) processes at these energies. The competing nature of various modes of fission i.e. symmetric (Sym) and asymmetric (Asym) is analyzed in terms of fission mass distributions and related symmetric to asymmetric fission peak ratios. The asymmetric fission is dominant decay mode for the above mentioned nuclei at all considered energies. The analysis is further extended to isotopic chains of several pre-actinide and actinide nuclei, for adequate addressal of mass dependence of fragment distributions. The calculated results show a transition from symmetric to asymmetric fission when one goes from lighter to heavier isotopic mass. The transitional region for studied isotopic chains lie around N/Z≈1.4 of compound nuclei, which exhibit the triple humped mass distribution. Further, the most energetic asymmetric light (A_L) and corresponding heavy (A_H) fission fragments are identified for a long isotopic chain of pre-actinide and actinide nuclei. Interestingly, the heavy asymmetric fission fragments are observed near proton number Z=50 for pre-actinide region and Z=54 for actinide region.

It is concluded that switching from symmetric to asymmetric fission and the possibility of in between triple humped structure is primarily because of the deformation effects of nascent fragments. It is relevant to mention here that above mentioned structural features survive, even at T$\geq$1.5 MeV, where shell effects are suppose to suppressed significantly.

In chapters 3 to 6, variety of nuclear reactions are studied in order to understand the dynamical and structural features involved in fission mechanisms. The collective conclusions derived from these studies are presented in the forthcoming chapter. A brief outline for future prospects is also discussed in the end.

Bibliography

[1] T. K. Ghosh, S. Pal, K. S. Golda and P. Bhattacharya, Phys. Lett. B **627**, 26 (2005).

[2] A. Sen, T. K. Ghosh and S. Bhattacharya *et al.*, Phys. Rev. C **96**, 064609 (2017).

[3] N. Eren, N Buyukcizmeci and R Ogul, Phys. Scr. **76**, 657 (2007).

[4] A. Kaur and M. K. Sharma, Eur. Phys. J. A **55**, 89 (2019).

[5] A. Kaur and M. K. Sharma, Indian J. Pure Appl. Phys. **57**, 576 (2019)..

[6] M. K. Sharma, S. Kanwar, G. Sawhney and R. K. Gupta, Phys. Rev. C **85**, 064602 (2012).

[7] G. Sawhney, G. Kaur, M. K. Sharma and R. K. Gupta, Phys. Rev. C **88**, 034603 (2013).

[8] G. Sawhney, R. Kumar and M. K. Sharma, Phys. Rev. C **86**, 034613 (2012).

[9] M. Kaur and M. K. Sharma, Phys. Rev. C **85**, 054605 (2012).

[10] M. Kaur, M. K. Sharma and R. K. Gupta, Phys. Rev. C 86, 064610 (2012).

[11] B. B. Singh, M. K. Sharma and R. K. Gupta, Phys. Rev. C **77**, 054613 (2008).

[12] A. Kaur, G. Kaur and M. K. Sharma, Braz. J. Phys. **48**, 608 (2018).

[13] G. Kaur, K. Sandhu, A. Kaur and M. K. Sharma, Phys. Rev. C **97**, 054602 (2018).

[14] A. Kaur, K. Sandhu and M. K. Sharma, Commun. Theor. Phys. **70**, 565 (2018).

[15] T. Banerjee *et al.*, Phys. Rev. C **96**, 014618 (2017).

[16] K. E. Rehm *et al.*, Phys. Rev. Lett. **81**, 3341 (1998).

[17] A. M. Samant, S. Kailas, A. Chatterjee, A. Shrivastava, A. Navin and P. Singh, Eur. Phys. J. A **7**, 59 (2000).

[18] A. C. Berriman, D. J. Hinde, M. Dasgupta, C. R. Morton, R. D. Butt and J. O. Newton, Nature **413**, 144 (2001).

Chapter 7

Summary and outlook

The experimental evolution of the 'accelerators and detectors' led the incredible progress in the nuclear fission research field. Theoretical interpretation of experimental outcomes is very challenging and important task, because it manifests the interesting dynamical aspects of the nuclear fission process. In this work, the dynamical cluster-decay model (DCM) is employed to examine the different compound nucleus (CN) and non-compound nucleus (nCN) fission mechanisms observed in the light particle, heavy ion and loosely bound projectile induced reactions. The possibility of light particle emission (or equivalently evaporation residue) is also examined for studied nuclei. Besides this, an effort is made to investigate the spontaneous fission (SF) of superheavy nuclei (SHN) occurring as an end product in the α-decay chains. The nuclear systems studied in this thesis vary from the light mass to superheavy region. The fission analysis is legitimate, only if it is studied at several energies across the barrier. At such higher energies, the incorporation of temperature (T), angular momentum (ℓ), deformation and orientation effects become important, which are duly included in this study. Further, the detailed analysis of fine structure effects among the fission fragments is accomplished in reference to variation in mass number and incident energies. A comprehensive information of fission mechanism form experiment and theoretical point of view, and its relevance on various entrance channel factors is discussed in the **chapter 1**. The objectives of this thesis work are achieved by employing the dynamical theory of DCM approach. This methodology describes the fragmentation potential energy in terms of collective coordinates, which is further used to obtain the formation probability of nascent fragments. The penetration probability of these nascent fragments is estimated by utilizing the WKB approximation. **Chapter 2** contains the relevant description of the methodology used.

First, the application of DCM approach is utilized for the non-rotating spontaneous fissioning nuclei (i.e. ℓ=0 case). The spontaneous fission (SF) process have decisive impact in the stability/existence of superheavy nuclei (SHN). Therefore, the dynamics involved in SF decay of various isotopes of Z=103-112 superheavy nuclei is analyzed in **chapter 3**. Interestingly, these nuclei are obtained as the end products in α-decay chains of ^{282}113, ^{287}114, ^{287}115, ^{288}115, ^{291}116, ^{293}117, ^{294}117 and ^{294}118 nuclei. The temperature effects are incorporated in terms of recoil energy (E_R) of residual SHN, left after neutron evaporation from the CN. The competition between α-decay and SF of SHN is examined, and it is observed that SF is the prominent decay mode for all studied SHN. Using the characteristics of preformation probability P_0, the energetically favoured nascent fragments are identified for aforementioned SHN, lying in the vicinity of magic numbers of Z=50 and N=82. The mass distributions of the studied SHN are clearly symmetric, which in turn provide information related to nuclear structure effects. The experimental confirmation of such predictions would be interesting. Further, the SF half-lives are calculated for these identified most probable fission fragments, which show nice agreement with the experimental observations. The relative study of 'hot compact' and 'cold elongated' configurations of decaying fragments suggests that 'hot compact' configurations are more favourable for the SF decay of SHN. Apart from this, it is emphasised that the 'shell correction' term in the collective fragmentation potential plays a key role to study the fragment mass distributions.

The fission decay analysis is further extended in **chapter 4**, for the case of light particle and heavy ion induced reactions. First, a wide range of incident neutron energies (i.e. E_n=32.8-59.9 MeV) is explored to study n+^{232}Th$\rightarrow$ ^{233}Th* and n+^{238}U$\rightarrow$^{239}U* reactions. A relative analysis of spherical and β_2-deformed fragmentation demonstrates that the impact of deformations is not crucial for the contributing fission region of n-induced reaction at studied energies. The mass distribution of fission fragments suggests the asymmetric fission is dominant decay mode for both actinide nuclei. However, a small hump around the symmetric fragments is observed for ^{233}Th* nucleus, which is not seen in the mass distribution of ^{239}U* nucleus. Interestingly, this outcome is in accordance with

the experimental observation. Also, the DCM-estimated fission excitation functions show good agreement with the measured data. Further, a relative fission decay analysis of four actinide nuclei i.e. ^{233}Th*, ^{233}Pa*, ^{239}U* and ^{239}Np* is carried out, which are formed under the same reaction conditions. In addition to this, an effort is made to study the influence of sticking and non-sticking moment of inertia on fission decay of ^{233}Th* nucleus. It is observed that sticking limit is favourable for the estimation of fission excitation functions. Finally, the role of projectile is examined by studying reactions involving charged particle (p) beam as projectile in addition to the neutral neutron (n) beams at common incident energy E∼27 MeV. Interestingly, the mass distributions show same behavior for both type of projectile.

This chapter is extended further to the investigation of heavy ion induced reaction. For this purpose, ^{32}S+^{184}W→^{216}Th* reaction is studied at energies around the Coulomb barrier for the choice of β_2-static deformed choice of fragmentation using optimum orientations. The fission fragment anisotropies (A) are estimated using the standard saddle-point statistical model (SSPSM) using DCM parameters. The comparison of calculated-anisotropies with the measured one show some difference at above barrier energies, which indicates the presence of nCN content in the decay of ^{216}Th* nucleus. Further, the capture cross-sections are obtained within DCM by adding the contributions of various CN and nCN decay processes such as evaporation residue (ER), fusion-fission (ff), quasi fission (QF) and fast fission (FF). Here, the predicted ER contributions are negligibly small in accordance with experimental findings. The mass distributions of ^{216}Th*, are asymmetric in nature independent of the incident energy, as observed for the case of light particle induced fission of actinide systems. Beside this, the quasi fission barrier is calculated as a function of angular momentum (ℓ), which show decrement as ℓ-values rises. Whereas, the fast fission process contributes at higher ℓ-values where fission barrier disappears. This implies that the probability of formation of compound nucleus also reduces at higher angular momentum values in addition to higher energies. Finally, the role of β_2-dynamic deformations on CN and nCN decay of ^{216}Th* nucleus is explored at highest energy, where nCN fission competes with CN fission. With the inclusion of dynamic deformations, symmetric fission channel start contributing the total fission excitation functions along with the asymmetric fission decay mode. Apart from this, the barrier characteristics are differ-

ent for the choices of static and dynamic deformations, thereby affecting the contribution of various decay mechanisms.

The study of fission mechanism is extended further in **chapter 5** by studying the impact of tightly bound and loosely bound projectile on same target within the framework of DCM. In the first case, the possibility of evaporation residue and fission decay of smaller compound nuclei i.e. ^{68,70}Ge* formed in ^{4,6}He+^{64}Zn reactions, is examined. It is observed that this compound nucleus mainly decays via ER channel, and the contribution of fission cross-sections is negligibly small. Hence, the fusion cross-sections are estimated by adding the contributions of ER channels. For the case of ^{68}Ge* nucleus, the calculated excitation functions of ER channels such as p- and n-emissions, show nice agreement with measured ER data. On the other side, there is a possibility that the ER channels of ^{70}Ge* nucleus formed in loosely bound projectile induced reaction, show some deviation from experimental measurements due to the possible presence of breakup+transfer processes. To investigate this, the individual ER cross-sections of ^{70}Ge* nucleus are calculated [e.g. $(2n)^{68}$Ge, $(np)^{68}$Ga, $(2np)^{67}$Ga and $(n\alpha)^{65}$Zn]. It is observed that the σ_{ER} for $(n\alpha)^{65}$Zn and $(2np)^{67}$Ga channels deviate from the experimental data, which advocates the presence of breakup+transfer processes. By applying relevant energy corrections, the breakup+transfer excitation functions are estimated, and the total sum of fusion and breakup+transfer contributions show good agreement with the experimentally measured fusion data. The comparison of complete fusion excitation functions of tightly bound '^{4}He' and loosely bound '^{6}He' projectile induced reactions indicates the sub-barrier enhancement and above-barrier suppression in the fusion excitation functions of ^{6}He+^{64}Zn reaction. These results can be explained on the basis of structure properties of loosely bound projectile. The larger radius of the loosely bound projectile reduces the Coulomb barrier, as a result one can expect the fusion enhancement. Besides this, the low binding energy of '^{6}He' nucleus implies large contribution of breakup+transfer channels which results in the suppression of fusion cross-sections at above barrier energies.

After analyzing that ER is main decay mode of lighter nuclei formed in tightly and loosely bound He-induced reactions, it will of further interest to analyze the fission decay of heavier nuclei formed in such kind of reactions. Therefore, the fission decay analysis is

carried out for various At* isotopes with mass A_{CN}=212-217 formed in tightly (^{3,4}He) and loosely (^{6,8}He) bound projectile induced reactions on same target (^{209}Bi). First, the neck-length parameter 'ΔR' is optimized in order to address the experimental fission excitation functions available at above barrier energy region for the case of ^{212,213,215}At* isotopes. The neck-length parameter ΔR increases linearly with compound nucleus energy E^*_{CN}, which in turn provide an opportunity to predict the below barrier fission contributions for these isotopes. By employing the systematics of ^{212,213,215}At* isotopes, the fission contributions are predicted for another loosely bound and neutron-rich projectile induced reaction i.e. ^{8}He+^{209}Bi$\rightarrow^{217}$At* at E^*_{CN} across the barrier. Further, the N/Z dependence of various DCM observables in reference to the fission mechanism is estimated, where N and Z are the neutron and atomic number of compound nucleus. The fission excitation functions show increment as a function of E^*_{CN} as well as N/Z ratio. Using the characteristics of fragmentation potential and preformation probability, the fission fragment mass distributions are analyzed. Also, the most probable nascent fragments are identified, which lie in the region of magic shell closures with Z or N=50 and N=82. Besides this, the observed mass distributions are asymmetric in nature for all isotopes, although a small hump with very small preformation factor appears around symmetric fragments for lighter mass isotopes.

In **chapter 6**, the DCM approach is further applied to investigate the fine structure effects in the fission fragment mass distributions of various pre-actinide (^{201}Bi*, ^{206}Po*, ^{211}At* ^{212}Rn*, ^{216}Ra*) and actinide nuclei (^{227}Pa* and ^{228}U*) produced via ^{19}F-induced reactions. This study is highly desirable, because it may provide possibility of new nuclei far from stability line. Initially, the energy dependence of fine structure effects in terms of fragmentation potential and preformation probability is analyzed, at near and above barrier energies. The calculated results suggest that the asymmetric fission is main decay channel for above mentioned nuclear systems. Whereas, the contribution of symmetric component is relatively more at below barrier region for lighter nuclei such as ^{201}Bi*, ^{206}Po* and ^{211}At*. These observations are further confirmed by the estimated symmetric to asymmetric fission peak ratios (P_{Sym}/P_{Asym}) varying with $E_{c.m.}$. In this chapter, the calculations are performed at sufficiently higher temperature (T$\geq$1.5 MeV), where

the shell correction term plays limited role. This in turn suggests that the fission path may be influenced via deformation effects of decaying fragments. The fission excitation functions are calculated for aforementioned nuclei, which match with the experimental data except at few highest energies. This deviation indicates the presence of nCN content at these energies, which is in agreement with the chapter 4 observations. The analysis is extended further by exploring the mass dependence of fine structure effects for a series of proton-rich to neutron-rich nuclei at common $E_{c.m.}$≈80 MeV near the Coulomb barrier. It is observed that lighter mass isotopes show symmetric mass distribution. However, with the increase in mass, a three peaked structure appears which indicates the co-existence of symmetric and asymmetric fission channels. The heavier isotopes mainly decay via asymmetric fission. The transitional region for studied isotopic chains lie around N/Z≈1.4 of compound nuclei, which exhibit the triple humped mass distribution. Finally, the most probable fission decay fragments are identified for these isotopic chains, which lie around the proton number Z=50 for pre-actinide nuclei and Z=54 for actinide nuclei.

The above mentioned work is related to the CN and nCN decay mechanisms of fissioning nuclei formed via variety of nuclear reactions. This work is confined to the quadrupole (β_2) deformations and coplanar (ϕ=0) orientations only. It will be of further interest to extend above mentioned studies to the higher multipole deformations and non-coplanar orientation of nuclei. It is well known that the the identification of CN and nCN fission is complex process, but these mechanisms are highly dependent on the entrance channel factors. On the basis of these properties, the study of nCN fission can be explored for multiple reactions with different entrance channels but having same composite system. It is observed in present study that deformations play significant role in the evolution of fine structure effects. Therefore, the analysis of higher order deformations on fission mass distributions of pre-actinide and actinide nuclei will be of future interest.